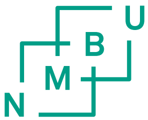

Norwegian University of Life Sciences
Faculty of Science and Technology

Philosophiae Doctor (PhD)
Thesis 2018:59

Hyperspectral Photoluminescence Imaging of Silicon Wafers and Solar Cells

Hyperspektral avbildning av fotoluminescens fra silisiumbaserte skiver og solceller

Torbjørn Mehl

Hyperspectral Photoluminescence Imaging of Silicon Wafers and Solar Cells

Hyperspektral avbildning av fotoluminescens
fra silisiumbaserte skiver og solceller

Philosophiae Doctor (PhD) Thesis

Torbjørn Mehl

Norwegian University of Life Sciences
Faculty of Science and Technology

Ås (2018)

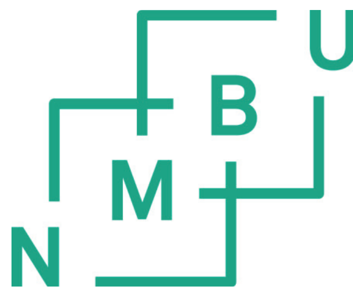

Thesis number 2018:59
ISSN 1894-6402
ISBN 978-82-575-1528-7

This research has been a part of the FME - SuSolTech center for renewable energy technology sponsored by the Norwegian Research Council together with Norwegian industrial partners.

Supervisory team

Prof. Espen Olsen, (main supervisor)
Faculty of Science and Technology
Norwegian University of Life Sciences

Dr. Ingunn Burud, Associate Professor (co-supervisor)
Faculty of Science and Technology
Norwegian University of Life Sciences

Dr. Andreas Svarstad Flø, Senior Engineer (co-supervisor)
Faculty of Science and Technology
Norwegian University of Life Sciences

Evaluation committee

Dr. Christian Rogaß, PostDoc Remote Sensing (first opponent)
Helmholtz Centre Potsdam
GFZ German Research Centre for Geosciences, Potsdam, Germany

Dr. Gaute Stokkan, Senior Research Scientist (second opponent)
Sustainable Energy Technology
SINTEF Industry

Prof. Knut Kvaal, (committee coordinator)
Faculty of Science and Technology
Norwegian University of Life Sciences

Summary

Hyperspectral photoluminescence imaging is a non-destructive characterization method used to study radiative defects in crystalline silicon wafers and solar cells. It provides both spatial distribution and spectral response of these crystal imperfections and impurities. The goal of this research has been to establish hyperspectral photoluminescence imaging as a characterization method. The objectives of this research have been three-fold; to optimize, verify and apply the method.

In the optimizing process, an oscillation in the background noise was identified. An enhanced noise removal algorithm was developed, drastically increasing the camera's sensitivity, allowing even weakly emitting defects to be detected. By application of a macro-lens, the spatial resolution has been improved from 200 to 27 μm.

Verification of the method was done by comparing results with several complementary characterization techniques and on various materials. In addition to multicrystalline silicon wafers and solar cells, samples of mono and mono-like crystalline silicon have been characterized with success. The results show that hyperspectral photoluminescence imaging correlates well and in some instances, compared with electroluminescence, yields richer data output.

The third objective of this research was to show that the method might be applied as a characterization method in line with other existing methods. This objective has been achieved in two studies. One of these studies has led to a patent application.

The conclusion is that Hyperspectral photoluminescence imaging is a method that may be used on par with other characterization methods.

Sammendrag

Hyperspektral avbildning av fotoluminescens er en ikke-destruktiv karakteriseringsmetode av radiative defekter i krystallinske silisiumbaserte skiver og solceller. Metoden gir både romlig fordeling og spektral respons av disse krystallfeilene og urenhetene. Målet med denne forskningen har vært å etablere hyperspektral avbildning av fotoluminescens som en karakteriseringsmetode. Formålet med denne forskningen har vært tredelt; optimalisere, verifisere og anvende metoden.

Underveis i optimaliseringsprosessen ble svingninger i bakgrunnsstøyen identifisert. Det ble utviklet en forbedret algoritme for fjerning av bakgrunnsstøy, noe som gjorde at kameraets sensitivitet økte drastisk og førte til at selv defekter som avga signaler med svak intensitet kunne oppdages. Ved å benytte en makrolinse er den romlige oppløsningen blitt forbedret fra 200 til 27µm.

Verifisering av metoden ble gjort ved å sammenligne resultatene med flere komplementære karakteriseringsteknikker og ulike materialer. I tillegg til multikrystallinske silisiumskiver og solceller, har prøver av mono- og mono-lignende krystallinsk silisium blitt karakterisert med suksess. Resultatene viser at hyperspektral billedtaking av fotoluminescens samsvarer godt med andre metoder og at den i noen tilfeller, sammenlignet med elektroluminescens, gir mer rikholdig data.

Det tredje formålet med denne forskningen har vært å vise at metoden han benyttes som en karakteriseringsmetode på lik linje med andre eksisterende metoder. Dette er vist i to studier hvorav en av disse har resultert i en patentsøknad.

Konklusjonen er at hyperspektral avbildning av fotoluminescens er en metode som kan brukes på lik linje med andre karakteriseringsmetoder.

Acknowledgments

My PhD journey started with *Varig Videreutdanning* in Physics at NMBU. This was an offer of competence building for high school teachers lacking sufficient university credits to teach physics. Throughout this education, Associate Professor Arne Auen Grimenes ignited the spark of interest resulting in me embarking on a PhD. I want to thank Arne Auen Grimenes for setting me on this great path.

I want to thank my supervisor, Professor Espen Olsen and co-supervisors Dr. Ingunn Burud and Dr. Andreas Svarstad Flø. I thank you for valuable discussions and giving me the academic freedom to pursue my interests. I would like to thank the master students who have been a part of the Solar Cell Group at RealTek. A special thanks to Guro Wyller, Audun Ingebrigtsen, Simen Bergan, Lisa Kvalbein and Malin Iris Helander. I want to extend my gratitude to the Section for Learning and Teacher Education for the opportunity to teach future physics and informatics teachers, a valuable experience enhancing the content of my PhD.

I want to thank Dr. Dominik Lausch and Tabea Luka for great collaboration over the past four years. I also want to thank them for the half-year I spent at Fraunhofer CSP in Halle, Germany. This was a valuable learning experience and academic development. I also want to thank Marcus Gläser for invaluable help and introduction to the German way of life. I want to thank Dr. Otto Breitenstein at Max Planck Institute of Microstructure Physics for his warm welcome and inspiring conversations. I want to thank the team at INES, France and especially Dr. Elénore Letty and Dr. Wilfried Favre for proving samples and a generally fruitful collaboration. I want to thank Professor Marisa Di Sabatino Lundberg and her team at NTNU, Norway both for supplying samples and through analyzes.

I thank my sister Dr. Anna Mehl for invaluable help in proof reading the final versions of articles and the PhD thesis.

Since I am still married and have not been divorced in the past 4 years, I owe my wife great thanks. This PhD would not have been possible without the wonderful patience and understanding from her and our two children.

Torbjørn Mehl
Ås, August 2018

Abbreviations

ALS	**A**lternating **L**east **S**quares
BB	**B**and to **B**and
BNM	**B**ackground **N**oise **M**atrix
CCD	**C**harge-**C**oupled **D**evice
CF	**C**orrected **F**rame
Cz	**Cz**ochralski (monocrystalline)
DRL	**D**efect **R**elated **L**uminescence
DS	**D**irectional **S**olidification
EBSD	**E**lectron **B**ack**S**catter **D**iffraction
EL	**E**lectro**L**uminescence
GB	**G**rain **B**oundary
HSEL	**H**yper**S**pectral **EL**ectroluminescence
HSPL	**H**yper**S**pectral **P**hoto**L**uminescence
ICA	**I**ndependent **C**omponent **A**nalysis
LM	**L**ight **M**icroscopy
MC	**M**omentum **C**onserving
MCR	**M**ultivariate **C**urve **R**esolution
mc-Si	**m**ulti**c**rystalline **Si**licon
NIR	**N**ear-**I**nfra**R**ed
PCA	**P**rincipal **C**omponent **A**nalysis
PL	**P**hoto**L**uminescence
PLS-DA	**P**artial **L**east **S**quares **D**iscriminant **A**nalysis
PV	**P**hoto**V**oltaics
ReBEL	**Re**verse-**B**ias **E**lectro**L**uminescence
RF	**R**aw **F**ame
SEM	**S**canning **E**lectron **M**icroscopy
SRH	**S**hockley **R**ead **H**all
SWIR	**S**hort-**W**avelength **I**nfra**R**ed
TD	**T**hermal **D**onors
TEM	**T**ransmission **E**lectron **M**icroscopy
TO	**T**ransverse **O**ptical

List of papers

This thesis is based on the following seven papers, attached in the appendix, and referred to in the text by their Roman numerals.

Paper I

Mehl, Torbjørn; Wyller, Guro Marie; Burud, Ingunn; Olsen, Espen. *Increased Sensitivity In NIR Hyperspectral Imaging By Enhanced Background Noise Subtraction*. Submitted to Optics Letters

Paper II

Burud, Ingunn; **Mehl, Torbjørn**; Flø, Andreas Svarstad; Lausch, Dominik; Olsen, Espen. *Hyperspectral photoluminescence imaging of defects in solar cells*. Journal of Spectral Imaging 2016; Volume 5.

Paper III

Lausch, Dominik; **Mehl, Torbjørn**; Petter, Kai; Flø, Andreas Svarstad; Burud, Ingunn; Olsen, Espen. *Classification of crystal defects in multicrystalline silicon solar cells and wafer using spectrally and spatially resolved photoluminescence.* Journal of Applied Physics 2016; Volume 119:054501.(5)

Paper IV

Mehl, Torbjørn; Di Sabatino Lundberg, Marisa; Adamczyk, Krzysztof; Burud, Ingunn; Olsen, Espen. *Defects in multicrystalline Si wafers studied by spectral photoluminescence imaging, combined with EBSD and dislocation mapping*. Energy Procedia 2016; Volume 92. p. 130-137

Paper V

Mehl, Torbjørn; Burud, Ingunn; Letty, Elénore; Olsen, Espen. *Oxygen-related defects in n-type Czochralski silicon wafers studied by hyperspectral photoluminescence imaging*. Energy Procedia 2017; Volume 124. p. 107-112

Paper VI

Olsen, Espen; Bergan, Simen; **Mehl, Torbjørn**; Burud, Ingunn; Ekstrøm, Kai Erik; Di Sabatino Lundberg, Marisa. *Defect related radiative recombination in mono-like crystalline silicon wafers*. Physica Status Solidi (a) applications and materials science 2017; Volume 214.(8)

Paper VII

F. Frühauf, P.P. Altermatt, T. Luka, **T. Mehl**, H. Deniz, and O. Breitenstein. *Injection intensity-dependent recombination at various grain boundary types in multicrystalline silicon solar cells*. Solar Energy Materials and Solar Cells 2018; Volume 180. p. 130-137

Additional scientific work performed during the PhD program

Paper

Olsen, Espen; Kvalbein, Lisa; Helander, Malin Iris; **Mehl, Torbjørn**; Letty, Elénore; Favre, Wilfried; Veirman, Jordi; Burud, Ingunn. *Study of oxygen in Czochralski silicon by hyperspectral photoluminescence*. EU PVSEC 2017 Proceedings; p. 583-585

Oral presentations

Mehl, Torbjørn; Di Sabatino Lundberg, Marisa; Adamczyk, Krzysztof; Burud, Ingunn; Olsen, Espen. *Studies of defects in mc-Si wafers by spectral PL imaging, EBSD and dislocation mapping*. Norwegian Solar Cell Conference 2016; 2016-05-31 - 2016-06-01

Mehl, Torbjørn; Wyller, Guro Marie; Burud, Ingunn; Olsen, Espen. *Increased sensitivity in NIR hyperspectral imaging by enhanced background noise subtraction*. 18th International Conference on Near Infrared Spectroscopy; 2017-06-11 - 2017-06-15

Posters

Mehl, Torbjørn; Burud, Ingunn; Flø, Andreas Svarstad; Olsen, Espen. *Defect related photoluminescence in solar cells studied by spectral imaging*. 8th International Workshop on Crystalline Silicon for Solar Cells (CSSC-8); 2015-05-05 - 2015-05-08

Mehl, Torbjørn; Di Sabatino Lundberg, Marisa; Adamczyk, Krzysztof; Burud, Ingunn; Olsen, Espen. *Defects in multicrystalline Si wafers studied by spectral photoluminescence imaging, combined with EBSD and dislocation mapping*. SiliconPV 2016; 2016-03-07 - 2016-03-09

Bergan, Simen; **Mehl, Torbjørn**; Di Sabatino Lundberg, Marisa; Burud, Ingunn; Olsen, Espen. *Defect Related Radiative Recombination in Mono-like Crystalline Silicon Wafers*. 32 EUPVSEC; 2016-06-20 - 2016-06-24

Mehl, Torbjørn; Burud, Ingunn; Letty, Elénore; Olsen, Espen. *Oxygen-Related Defects in n-Type Czochralski Silicon Wafers Studied by Hyperspectral Photoluminescence Imaging*. SiliconPV 2017; 2017-03-03 - 2017-03-05

Mehl, Torbjørn; Burud, Ingunn; Letty, Elénore; Olsen, Espen. *Oxygen-Related Defects in n-Type Czochralski Silicon Wafers Studied by Hyperspectral Photoluminescence Imaging*. Norwegian Solar Cell Conference 2017; 2017-05-09 - 2017-05-10

Kvalbein, Lisa; Helander, Malin Iris; **Mehl, Torbjørn**; Burud, Ingunn; Letty, Elénore; Olsen, Espen. *Hyperspectral photoluminescence imaging of n-type Czochralskisilicon through an ingot*. Norwegian Solar Cell Conference 2017; 2017-05-09 - 2017-05-10

Olsen, Espen; Kvalbein, Lisa; Helander, Malin Iris; **Mehl, Torbjørn**; Letty, Elénore; Favre, Wilfried; Veirman, Jordi; Burud, Ingunn. *Study of oxygen in Czochralski silicon by hyperspectral photoluminescence*. EU PVSEC 2017; 2017-09-25 - 2017-09-29

Helander, Malin; Olsen, Espen; **Mehl, Torbjørn**; Søndanå, Rune; Burud, Ingunn. *Thermal donors in Czochralski Silicon Wafers Investigated by Spectral Imaging*. Norwegian Solar Cell Conference 2018; 2018-05-02 - 2018-05-3

Contents

Summary iii
Sammendrag v
Acknowledgments vii
Abbreviations ix
List of papers xi
Contents xv
1 Introduction and aims 1
1.1 Motivation 1
1.2 Objective of this research 1
1.3 Overview 2
2 Theoretical background 3
2.1 Crystalline silicon 3
2.1.1 Solidification techniques 3
2.1.2 Lifetime 3
2.1.3 Bandgap 4
2.1.4 p-n junction 4
2.1.5 Recombination mechanisms 5
2.2 Defects in crystalline silicon 7
2.2.1 Impurities 7
2.2.2 Dislocations 7
2.2.3 Surfaces, twins and grain boundaries 7
2.2.4 Precipitates 8
2.3 Band-to-band photoluminescence 9
2.4 Defect related luminescence 9
2.5 Temperature dependence of radiative recombination 10
2.6 Laser penetration depth in crystalline silicon 10
3 Experimental 13
3.1 Samples 13
3.1.1 Monocrystalline 13
3.1.2 Mono-like 13
3.1.3 Multicrystalline 13
3.2 Hyperspectral imaging 14
3.2.1 Hyperspectral camera 15
3.2.2 Line laser 16

3.2.3 Long pass filter 16
3.2.4 Sample holder 16
3.3 Data processing 17
3.3.1 Pre-processing 17
3.3.2 Multivariate Curve Resolution analysis 18
3.3.3 Partial Least Squares Discriminant Analysis 19
4 Results and discussion 21
4.1 Optimization of the method/equipment. 21
4.1.1 Algorithm enhancements for better signal-to-noise ratio 21
4.1.2 Macro lens for higher resolution 24
4.1.3 Enhance the analysis technique 24
4.1.4 Sample preparation 26
4.1.5 New long pass filter 27
4.2 Verification of the method 27
4.2.1 HSPL combined with electroluminescence 27
4.2.2 HSPL combined with electron backscatter diffraction and dislocation mapping 28
4.2.3 Mono crystalline and room temperature 31
4.2.4 Mono-like wafers 32
4.3 Application of the method 33
4.3.1 Further TD investigations 33
4.3.2 Study of injection intensity-dependent recombination 33
5 Conclusion 37
6 Further work 39
Bibliography 41
Appendix – Papers 45

1 Introduction and aims

1.1 Motivation

The Photovoltaics (PV) industry has a strong focus on price and quality. To reduce production cost and secure good quality it is mandatory to reduce defects in the solar cell material. Crystalline silicon, holding approximately 90 % of the market[1], can have structural imperfections and contain impurities; defects that limit the carrier lifetime and lead to efficiency reductions. Thus, it is essential to understand why they occur and how they can be avoided.

To study defects in crystalline silicon, many different characterization methods can be used. Some of these methods are destructive, others not. To get a deeper knowledge of a problem, it is often necessary to combine two or more methods. By using two or more destructive methods, it is therefore necessary to have samples that are approximately equal, such as neighboring wafers. It is therefore an advantage to have methods to choose from which are non-destructive, especially when access to neighboring wafers is absent or the variation between them is high.

Hyperspectral photoluminescence (HSPL) imaging is a non-destructive characterization method of radiative defects in crystalline silicon wafers and solar cells. It provides both spatial distribution and spectral response of these crystal imperfections and impurities.

When this PhD research started, the only known HSPL equipment was at NMBU. It was built by Flø[2] during his PhD research 2010-2014 and had only been used in a few studies[3-6].

1.2 Objective of this research

The possibilities and limitations of hyperspectral imaging, as a tool for characterization of silicon wafers and solar cells, have not been fully explored and should therefore be investigated. Furthermore, the method was at an initial stage and held great potential for improvement. Hence, the overall objective of this research has been to explore and improve the use of hyperspectral photoluminescence imaging.

The objectives of this research have been to optimize the method, to verify the method and to apply the method.

The goal of optimizing the method was to improve images by reducing noise, achieving higher resolution and sharper images, and enhance the analysis. This was done by:

- Algorithm enhancements for better signal-to-noise ratio (**Paper I**)
- Macro lens for higher resolution (**Paper II**)
- Enhance the analysis by introducing another analysis technique (**Paper II**)
- Sample preparation; sharper images of wafers after etching (**Paper IV**)

Verification of the method was done by comparing HSPL results with several complementary methods and on various materials. The aim was to discover the applicability in combination with other characterization techniques.

- HSPL combined with electroluminescence (**Paper III**)
- HSPL combined with electron backscatter diffraction & dislocation mapping (**Paper IV**)
- HSPL used on mono crystalline wafers (**Paper V**)
- HSPL used on mono-like wafers (**Paper VI**)

The third objective of this research was to show that the method might be applied as a characterization method in line with other existing characterization methods. This was done in two studies.

- A study of thermal donors
- A study of injection intensity-dependent recombination (**Paper VII**)

1.3 Overview

This thesis is organized as follows: A brief introduction with the motivation for this thesis, followed by the objective and structure of this research in the next sections. Chapter 2 presents the theoretical background. In Chapter 3, the material and methods are described. Chapter 4 contains the main discussion of my research. The main conclusions are presented in Chapter 5, followed by suggestions for further work and bibliography. The seven papers are attached in the appendix.

2 Theoretical background

2.1 Crystalline silicon

In this section there will be given a brief introduction to solar cells physics, with a special focus on recombination paths.

2.1.1 Solidification techniques

In this research, wafers and solar cells of crystalline silicon have been studied. Solidified silicon forms a giant covalent structure, as each Si atom shares all its four valence electrons with other Si atoms, where the lattice pattern is of diamond cubic crystal structure. Two solidification techniques are dominant in the solar cell industry; the Czochralski (Cz) process to produce monocrystalline material and by directional solidification (DS) to produce multicrystalline material. In the Cz process, a single seed crystal is dipped in molten silicon. While the silicon solidifies around the seed, it is slowly pulled up of the melt as it rotates and forms a long cylindrical ingot, consisting of one single crystal.

On the other hand, in the less complex and thereby cheaper DS process, the molten silicon cools and solidifies in the crucible. The melt will solidify in the bottom and form a mosaic of crystals that will grow upward while the temperature drops. The resulting ingot consists of many grains. Wafers cut from a DS ingot are called multicrystalline silicon (mc-Si) wafers. The efficiency is lower in solar cells made from mc-Si than Cz wafers because of a greater present of defects.

When studying defects, neighboring wafers are often used. Neighboring wafers have almost identical properties due to the cutting of wafers being done perpendicular to the crystal growth direction.

2.1.2 Lifetime

In the Si crystal, electrons form covalent bonds. To break a bond, an electron can absorb an incoming photon, if the photon has equal or higher energy then the binding energy. The electron will leave a positively charged hole in the lattice and move free within the lattice. Since the electron is in an excited state, the electron may recombine with a hole. The average time the electron is free, the time from photon absorption to electron-hole pair annihilation, is called the charge carrier’s lifetime.

2.1.3 Bandgap

For a single atom, there exists a finite number of discrete energy states, called energy levels, an electron can possess. In a lattice structure, due to the wave function of the valence electrons in neighboring atoms, the energy levels are closely separated, and can be treated as continuous bands of legal energy, only broken by some regions, called bandgaps, with specific energies the electron cannot possess.

In the ground state, at 0 K, all electrons will have the lowest possible energy. Because of the Pauli Exclusion Principle, saying two fermions cannot be in the same quantum state, the electrons are filling energy bands from the bottom upwards[7]. In a semiconductor, the highest band occupied by electrons is called the valence band and the band above, the lowest unoccupied, is called the conduction band. As for crystalline Si, all valence electrons are involved in bonding and the valence band is completely filled with electrons, while the conduction band is completely empty. The bandgap, E_G, is defined as the difference between the lowest energy level in the conduction band, E_C, and the highest energy level in the valence band, E_V.

For indirect bandgaps, as in crystalline Si, E_V and E_C occur at different crystal momentum, thus an emission or absorption of a phonon is required in addition to absorption of a photon, to brake the bond; to excite an electron from the valence band to the conduction band[8].

2.1.4 p-n junction

Silicon has four valence electrons. By replacing some atoms in the crystal structure with atoms with more valence electrons, from Group V or higher of the Periodic Table, the material will be n-doped (n for negative). The most common is to use phosphorus (P). The crystal structure will then have some loosely bound electrons, which are in Coulombic bonds. Very little energy is required to excite these electrons, since the energy level is slightly lower than E_C. These atoms are therefore called donors, because they donates electrons to the lattice.

If atoms from Group III or lower of the Periodic Table are used instead, the material will be p-doped (p for positive). The most common is to use Boron (B). These atoms are called acceptors, because they need a valence electron from a neighboring bond to complete its bonding. The lack of an electron leaves a vacancy in the lattice that can be seen as a positively charged particle. Very little energy is required to ionize the acceptor, since the ionized state energy is slightly higher than E_V.

With a p-doped and an n-doped layer brought together, a diffusion of majority carriers will occur across the junction. Electrons will annihilate holes, leaving behind a layer of fixed charge on either side of the junction. This will set up an electrostatic field, which leads to drift of minority carriers back across the junction. Equilibrium is established when diffusion and drift are balanced. This leaves a junction region depleted of charge carriers, referred to as a p-n junction.

Illumination, with photon energy greater or equal to the bandgap, may break covalent bonds and form electron-hole pairs. The electric field in the p-n junction separates the photo-generated free charge carriers, electrons and holes. Connecting an external circuit will allow the electrons and holes to recombine. The idea behind the solar cell is to make use of the electric current in the external circuit. The current in the external circuit depends on the lifetime. With high recombination rates (i.e. short lifetimes), electrons recombine before being collected and thus the solar cell current suffers.

2.1.5 Recombination mechanisms

Shockley and Queisser[9] showed that the lifetime, τ, has the greatest impact on the efficiency of a solar cell. From Chen[10], the open circuit voltage, V_{oc}, can be written as

$$V_{OC} = constant + \frac{k_B T}{2q} \ln \tau \tag{1}$$

where k_B is the Boltzmanns constant, q is electric charge and T is the temperature of the solar cell. Equation (1) shows that shorter lifetime gives lower voltage and thus lower efficiency.

The recombination rate depends on several different recombination mechanisms. Some mechanisms are unavoidable (intrinsic), due to physical processes in the intrinsic material, while others are avoidable (extrinsic), mainly due to imperfect material[8]. The mechanisms can occur in parallel, and the total recombination rate is the sum of the rates from the individual mechanisms. Since the lifetime is inversely proportional to the recombination rate[10], the net recombination lifetime, τ, is given by equation (2).

$$\frac{1}{\tau} = \frac{1}{\tau_1} + \frac{1}{\tau_2} + \cdots + \frac{1}{\tau_n} \tag{2}$$

There are essentially four important recombination mechanisms[7] in solar cell material; Radiative recombination, Auger recombination, Shockley-Read-Hall (SRH) recombination and Surface recombination.

Radiative recombination

Radiative recombination, also called band-to-band (BB) recombination, is an intrinsic mechanism and is the inverse process of photon absorption. The exited electron in the conduction band, relax to the valence band and recombine with a hole. When they annihilate, a photon with energy E_G is emitted. This emission is denoted BB luminescence. The radiative BB recombination mechanism is dominant in direct semiconductors, but is suppressed in indirect semiconductors, due to the two-step process involving a phonon[11], resulting in a long lifetime.

Auger recombination

Another intrinsic mechanism is the Auger recombination. Unlike radiative recombination, no photon is emitted when an electron-hole pair annihilates. The energy released is transferred to a third charge carrier instead, either in the valence band or in the conduction band. The third charge carrier will relax back to its original state and deposit the extra energy as phonons in the lattice. Due to the use of a third charge carrier, Auger recombination is the dominant recombination mechanism in pure materials with high doping concentrations.

Shockley-Read-Hall recombination

SRH recombination, recombination thought traps, is by far the most important recombination mechanism in real semiconductors[8]. Impurities and defects in the crystal structure will provide legal energy levels, charge carrier traps, within the bandgap. These traps provide an efficient two-step recombination; an electron will first relax from the conduction band to the defect level, and then relax to the valence band where it annihilates a hole. The energy released is converted into photons or phonons, or both, depending upon the nature of the trapping process[12]. By lowering the temperature, the rate of photons increases, because the phonon activity decreases. At 90 K, different SRH recombination pathways appears as separate signals[13].

Surface recombination

At the surface of a crystal, there is an incomplete structure, thus a high concentration of unsatisfied valence, often described as dangling bonds. The dangling bonds are the source of many legal energy levels within the bandgap, which can be used as traps in a two-step recombination. This leads to a high surface recombination rate. The problem is reduced or

eliminated by passivating the surface, e.g. with depositing of hydrogenated amorphous silicon on crystalline silicon[14].

2.2 Defects in crystalline silicon

A perfect Si crystal without defects does not exist in real life. During crystal growth, many imperfections are introduced. The different types of crystal defects can be classified by their dimension.

2.2.1 Impurities

0-dimensional defects are single point defects in the lattice. They can be either intrinsic or extrinsic. Intrinsic point defects occur in all crystalline solids[15], due to thermal excitation at temperatures above 0 K. A thermal excited Si atom will leave its position in the lattice, creating a point defect called vacancy, a vacant lattice site. The Si atom may diffuse in between the atoms in the lattice structure. A single Si atom, in a normally void space, is creating a self-interstitial point defect.

Single atoms of other elements than Si cause extrinsic point defects. If they are added to the material intentionally, they are called solutes, as in the case of doping where atoms are intentionally added to control the charge carriers. Non-intentionally added foreign atoms are called impurities. The impurity can be interstitial or substitutional, i.e. substitute a Si atom in a lattice site. Metastable point defects, as iron, can exist in many states. The two dominate states are, as interstitial, Fe_i, and in an ion pair, FeB. The state can be changed by temperature[16], illumination[17] or by forward-biased voltage[18].

2.2.2 Dislocations

1-dimensional defects are linear defects called dislocations. They can be categorized as either edge dislocations or screw dislocations. An edge dislocation occurs when a row of atoms ends within the lattice. A screw dislocation originates from a shift of one atom in the lattice with respect to a perfect arrangement. In real crystalline material, most dislocations are neither pure edge nor pure screw, but mixed dislocations along a curved dislocation line[15].

2.2.3 Surfaces, twins and grain boundaries

2-dimensional defects are interfacial defects and can be categorized as surfaces, twins or grain boundaries. The external surface of the crystal is often a complex structure with many

defects, although the structure is derived from the underlying parallel plane. A twin is the surface that separates two volumes of crystal, which are mirror images of each other.

A grain boundary (GB) is the interfacial structure that separates two grains, or crystals, having different crystal structure and/or crystallographic orientation[15]. GBs can by divided into three categories: low-angle grain boundaries (≤15°), random grain (or high-angle) boundaries (≥15°) and coincident site lattice boundaries.

Low-angle GB can be seen as a simple planar array of dislocations. An array of parallel edge dislocations makes a tilt boundary, while two sets of parallel screw dislocations make a twist boundary. The misorientation creates a tilt angle that can be used to describe the tilt boundary. The angle is parallel to the GB for twist boundaries.

For random GB, on the other hand, the interfacial is relatively disordered, with a high density of dangling bonds, thus providing many sites for solutes and impurities. Some high-angle GB has a degree of fit (Σ) between the structures, when a finite fraction of lattice sites coincides between the two lattices. These GBs are called coincident site lattice (CSL) boundaries, for $3 \leq \Sigma \leq 49$. CSLs boundaries are named by their fit. For a Σ9, there is one atom for each ninth that is shared between the two lattices.

2.2.4 **Precipitates**

3-dimensional defects are volume defects of aggregates of atoms or vacancies. Clusters of impurities, over a finite volume in a Si crystal, are called precipitates. Precipitates tend to be formed in the vicinity of lattice defects, thus decorating these dislocations and grain boundaries with impurities. Precipitates can also be formed in homogeneous regions of the crystals[19]. Trapped gasses or accumulation of vacancies gives voids within the lattice. A void can act as a sink for interstitials[20].

2.3 Band-to-band photoluminescence

Photoluminescence (PL) is radiative recombination (luminescence) gained by exciting electrons by use of illumination (photons). A laser, sending out photons with energy higher than the bandgap, can be used as an excitation source.

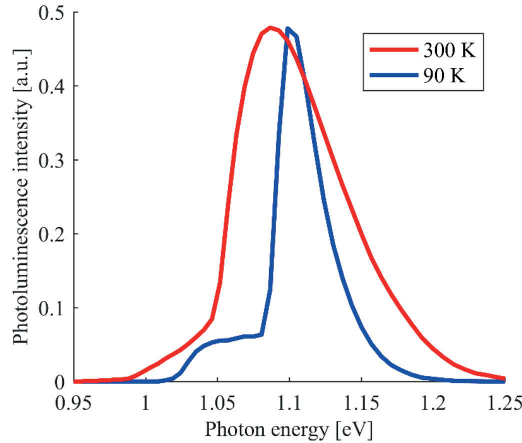

Figure 1 HSPL measurements of a mc-Si solar cell, at respectively 90 K (blue) and 300 K (red), illustrating the temperature dependent shift in energy and broadening of the peak for the band-to-band related photoluminescence. The BB PL knee at ~1.05 eV, is due to two-phonon emissions.

When referring to the band-to-band (BB) photoluminescence, it is in this thesis referred to the BB related photoluminescence peak having the highest intensity. At 90 K, the highest BB peak is at 1.10 eV. This peak is due to the BB photon emission assisted by the emission of a transverse optical (TO) phonon[21]. The TO phonon is a momentum conserving (MC) phonon. The BB luminescence knee, at ~1.05 eV in Figure 1, is due to two-phonon emissions, where TO(MC) + O^{Γ} is the most dominant. Γ is defined as the zero momentum point at the center of the Brillouin zone where the electron wave has no momentum from the perspective of the crystal lattice.

2.4 Defect related luminescence

SRH recombination originates from impurities, defects or a combination of both. Thus, photon emissions from SRH recombination are denoted defect related luminescence (DRL). Drozdov et al.[22] described in 1976 four DRL signals they related to dislocations. Thus, the findings are referred to as D-lines. The names and energy levels of the respective D-lines are, at 4.2 K: D1 0.812 eV; D2 0.875 eV; D3 0.934 eV and D4 1.000 eV. Since this first report, dislocations and their interactions with impurities have been investigated for decades by

various research groups[23]. Many theories as to what underlies each of the D-lines, have been submitted over the years[2]. Other DRL signals have also been reported, for various energy levels in the range 0.68 – 0.78 eV, and in addition D5 at 0.826 eV[24] and VID3 at 0.94 eV[5].

2.5 Temperature dependence of radiative recombination

The bandgap in crystalline Si is temperature dependent, varying from 1.17 eV at 0 K to 1.12 eV at 300 K. The decrease in the bandgap is linear at room temperature, but quadratic and decreases less for temperatures below 200 K. There are two main sources for the change in energy gap with temperature; thermal expansion and available phonons[25].

Because of thermal expansion of the lattice, there is a change in bond lengths with temperature, thus a change of the electron energies. The second contribution dominates at elevated temperatures above 100 K and is related to the electron–phonon interaction, reflecting the temperature dependence of the phonon distribution. Only a few numbers of allowed phonon energies (below a temperature dependent threshold value) are available for the electron–phonon interaction at low temperatures. In addition to the decrease in the bandgap due to rising temperature, there is a temperature dependent phonon-induced broadening of the bandgap[26]. The shift in energy and broadening of the peak, are illustrated in Figure 1 of two HSPL measurements of a mc-Si solar cell, at respectively 90 K and 300 K.

2.6 Laser penetration depth in crystalline silicon

To study SRH recombination in bulk material of a solar cell, the laser used for excitation has to penetrate into the bulk material by passing the anti-reflection coating, passivation layer, the emitter and the p-n junction. The total thickness of these layers is ~1 μm [27]. In studies of as-cut wafers, these manufactured layers are not present, but there is a sawing damage zone on the surface instead, with high recombination rate. The sawing damage runs ~10 μm into the material[28]. For wafers that have been textured, the sawing damage zone has been removed. Texturing is one of the first steps in the process of making a solar cell. It removes the sawing damage zone and at the same time create a surface structure that reduce reflection of light from the solar cell.

The penetration depth is dependent on both wavelength and temperature, and is defined as the depth where the light intensity has fallen to 1/*e* of its original value. At 300 K, phonons with a wavelength of 510 nm have a penetration depth of 1 μm in intrinsic Si, while 10 μm for

780 nm phonons[29]. By lowering the temperature, the penetration depth becomes longer. At 90 K, the penetration depth is 32 µm for 510 nm wavelength and 46 µm for 780 nm [30].

To excite electrons, the laser has to have a wavelength shorter than the band-to-band emission at 1.1 eV. This corresponds to a wavelength of 1127 nm. Since it must be possible to distinguish between band-to-band emissions and laser light, and block reflections from the laser light from entering the optics, by using a long pass filter, the laser wavelength should be shorter than ~1000 nm. The penetration depth for photons with wavelength of 1000 nm is 156 µm at 300 K. The preferred thickness of mc-Si wafers used in production lines today, is 180 µm [1]. Thus, a 1000 nm laser will go straight through the material, if the sample temperature is lowered. With a sample temperature lowered to 90 K, the laser wavelength should thus be shorter than 870 nm, which correspond to a penetration depth of 195 µm.

It can be concluded that if the same laser is going to be used at both at 300 K and 90 K, it must be in the range 780 – 870 nm. The 808 nm laser used in the HSPL setup meets this requirement. Photons with a wavelength of 808 nm have a penetration depth of 12.7 µm in intrinsic Silicon at 300 K. At 90 K, the penetration depth is 68.5 µm. The respective values were found by interpolation of data from Green[29] and Schinke et al.[30].

3 Experimental

3.1 Samples

One of the primary aims of this thesis has been to explore the use of hyperspectral photoluminescence imaging. Thus, several different types of samples have been investigated, although, to narrow the scope, only samples of crystalline silicon wafers and solar cells have been chosen. These are categorized as either mono-, mono-like- or multicrystalline. As-cut wafers and wafers gone through some treatments like polishing, etching and/or passivating have been characterized in addition to solar cells. Among these there have been both commercial and laboratory-produced (pilot scale) samples.

3.1.1 Monocrystalline

The sample characterized in **Paper V** is a wafer from an n-type, phosphorus doped, Czochralski ingot. The 156×156 mm^2 wafer is from the top part (seed-end) of an industrial ingot, solidified fraction < 5%. The wafer was chemically textured with potassium hydroxide (KOH) in order to remove the saw damaged layer.

3.1.2 Mono-like

In **Paper VI**, three 156×156 mm^2 as-cut mono-like crystalline silicon wafers were studied. The wafers were from three different heights, cut from a p-type (boron doped) mono-like silicon ingot. The ingot was produced in a pilot-scale furnace at NTNU in Trondheim. Six Cz monocrystalline seeds were used, positioned to form six inter-seed junctions with [110]/[110] boundary planes and three with [100]/[100] boundary planes. The seeds were placed in close contact except for two junctions with intentionally made gaps of 0.4 and 1.6 mm. The ingot was grown in the <110> direction. In each seed junction, there were different tilt and misorientations. See **Paper VI** and Ekstrøm et al.[31] for further details.

3.1.3 Multicrystalline

The p-type mc-Si wafer used in **Paper I** was chosen only for illustration of background noise. The 125×125 mm^2 sample was placed in the sample holder that allows samples of sizes up to 156×156 mm^2. The sample size was chosen in order to obtain a reference area throughout the recording. The sample had been solidified and processed at Fraunhofer ISE research laboratory.

Four mc-Si solar cells were used in **Paper II**. The sample referred to as Sample 1 in **Paper II** is actually two different solar cells. The electroluminescence (EL) image in Figure 2b) in **Paper II** is not of Sample 1, but from a neighboring solar cell of Sample 1. These two solar cells are also used in **Paper III**, see next paragraph for more details. Sample 2 and 3 are 156 × 156 mm^2 mc-Si solar cells commercially produced by DelSolar, Taiwan[32]. The solar cells were produced in 2013 or earlier and of p-type.

In **Paper III**, both wafers and solar cells were investigated. The 156 × 156 mm^2 mc-Si p-type solar cells were fabricated in 2009 by Q-Cell SE Germany with a standard commercial process. The as-cut wafers analyzed were neighboring wafers of the solar cells.

The samples investigated in **Paper IV** were 125×125 mm^2 mc-Si wafers made in a pilot scale furnace at NTNU in Trondheim. To fit into the electron backscatter diffraction (EBSD) apparatus, samples of 30×60 mm^2 in size were cut from the wafers. Three different types of samples were investigated in this study: sample A: p-type (boron doped); sample B: p-type (boron doped) enriched with Fe; and sample C: n-type (phosphorous doped) enriched with Fe. They were investigated by HSPL both as-cut and after having been polished and etched.

In **Paper VII**, two 156×156 mm^2 mc-Si solar cells from different producers were investigated by several different characterizations methods. HSPL measurements were performed on a passivated neighboring wafer of one of the solar cells.

3.2 Hyperspectral imaging

The camera and the laser are mounted on a rig that is attached to a motorized horizontal translation stage. The camera is mounted to point vertically downwards. A hyperspectral pushbroom camera takes pictures in one spatial dimension, a line. The second spatial

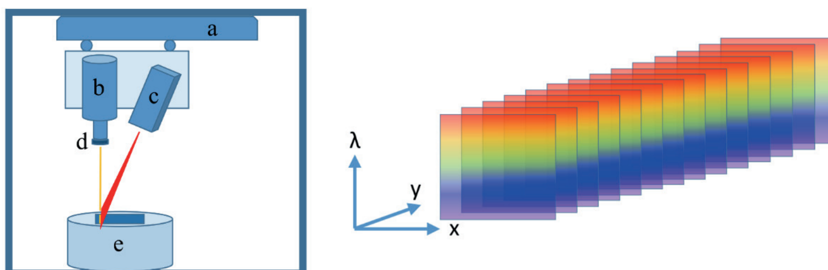

Figure 2. Hyperspectral imaging setup. a) translation stage, b) hyperspectral camera, c) line laser, d) long pass filter and e) cryogenic cooler. The camera records a 2D image with one spatial and one spectral dimension. The second spatial dimension is obtained by assembling images taken while the camera scans the sample using the translation stage.

dimension is obtained by assembling images taken while the camera is moving. The camera thus takes pictures of a horizontal line perpendicular to the direction of travel of the translation step. The line laser is mounted to the side of the camera and illuminates obliquely downwards on a slightly wider line segment than the camera can capture. The sample is placed on top of a cryogenic cooler in which the surface is parallel to the translational stage. A schematic sketch of the hyperspectral photoluminescence imaging setup is shown in Figure 2. The equipment is mounted in an enclosed cabinet made of anodized aluminum with a matte black finish. This prevents unwanted light from interfering with the recording and protects users from reflections from the laser light. The laser has an intensity of up to 20 suns, so even a fraction of the light can cause eye damage.

3.2.1 Hyperspectral camera

For image capture, a near-infrared (NIR) pushbroom hyperspectral camera (SWIR, Specim, Finland), with a mercury cadmium telluride detector (HgCdTe), has been used. The camera records a 14 bits 2D frame with one 320 pixels spatial dimension (x), and one 256 bands spectral dimension (λ). By assembling frames taken while the camera scans the sample, the second spatial dimension (y) is generated. This setup yields a three-dimensional data file (spatial x, y and spectral λ), called a hypercube. This provides a PL spectrum in each spatial pixel (x,y) of the sample.

The spectrum is divided between 256 sensors that measure the light intensity in each interval, distributed on wavelengths from 929.11 to 2530.70 nm. This corresponds to photons with energies from 1,334 eV down to 0.4899 eV. Interval widths do vary from 6.32 nm for the shortest wavelength, to 6.23 nm for the longest wavelength. The resolution of the measured value for a sensor is 14 bits, that is, values in the range of 0 to 16383 and referred to as counts. A count is proportional to the quantity of photons detected by the sensor.

Using the standard objective, S31-f/2.0, the spatial resolution can be adjusted in the range from 75 to 500 µm, by varying the distance between camera and sample holder. The macro objective, M=1 f/4.0, has a range from 25 to 30 µm. In the setup for this study, the spatial resolution have varied from 27 µm in **Paper VII**, 30 µm in **Paper II**, 100 µm in **Paper III**, 116 µm in **Paper VII**, 250 µm in **Paper IV** and 500 µm in **Paper I**, **II**, **V** and **VI**.

The scanning speed of the motorized linear translation stage depends on spatial resolution and frame rate. E.g., with a frame rate of 25 Hz and a spatial resolution of 500 µm, the scanning speed is set to 12.5 mm/s. This provides the same resolution in both spatial dimensions.

3.2.2 Line laser

As an excitation source, the hyperspectral PL setup is equipped with an 808 nm line laser. The Lasiris Magnum II (Coherent, USA) is a high power laser diode line generator with adjustable beam power up to 5600 mW and a fixed fan angle of 30 degrees. It generates a uniform, non-Gaussian, intensity distributed line. In a 500 µm resolution setup, this gives an irradiation power density of up to 2 W/cm^2.

3.2.3 Long pass filter

Since the camera detection range is from 930 to 2500 nm, the 808 nm laser light will not be detected. The camera's charged coupled device (CCD) is measuring the first order maxima of the diffraction pattern of light that has passed a dispersing element. The 808 nm laser's second order maxima is overlapping with the first order of 1616 nm wavelength light. To overcome this problem, a long pass filter is placed in front of the camera lens. A long pass filter blocks for shorter wavelengths and allows longer wavelengths to transmit (pass). In this study, both an 850 nm (Paper I – III) and a 1000 nm (Paper IV – VIII) long pass filter have been used to prevented laser beam reflections from entering the optic apparatus. Both have been high performance long pass filters from Edmund Optics with optical density ≥ 4.

In the papers, the term *low pass filter* has been used incorrectly. Instead, the term *long pass filter* should have been used. While some manufactures still use the term *low pass filter* for this kind of optical filter, the term is now mostly reserved frequency filters for acoustic and electronic applications.

3.2.4 Sample holder

For cooling the samples to 90 K, a cryogenic container filled with liquid nitrogen is used. The container was manufactured locally at NMBU. The entire outside of the container is covered with a thick layer of extruded polystyrene foam, except on the top of the container, where there is a plate of polished aluminum. The plate is adapted to wafers and solar cells up to 156 × 156 mm^2 in size, so that the entire sample comes into contact with the aluminum. Inside the tank, from the top of the container, heat sinks run down into liquid nitrogen. Small nozzles on the top of the container pour cold nitrogen vapor over the sample. Thus, the sample cools down quickly and in seconds, thermal equilibrium is achieved. The tank holds two liters and the temperature will remain constant until all the liquid nitrogen is evaporated. To control the temperature, a digital thermometer is attached to the surface of the cryogenic container.

The cryogenic container is also used as a sample holder for image capture at room temperature, but then without being filled with liquid nitrogen.

3.3 Data processing

The data from a hyperspectral recording is stored in a three dimensional matrix and all data processing and analysis have been done using MATLAB from The MathWorks, Inc., USA. MATLAB is a mathematical calculation program which is particularly suited for matrix manipulations, which is even reflected in the name, derived from MATrix LABoratory. In this study, several versions of the software have been used, from R2013a through R2016b. In addition, to do a Multivariate Curve Resolution (MCR) analysis and a Partial Least Squares Discriminant Analysis (PLS-DA), MATLAB was equipped with the MIA_Toolbox R3.0.3 and PLS_Toolbox R8.2.1 extensions from Eigenvector Research, Inc., USA.

3.3.1 Pre-processing

Before the recorded data can be analyzed, the hypercube, stored in a data file, has to be loaded into MATLAB. For this purpose it has been used an algorithm developed by Flø[2]. The algorithm load the data into MATLAB and, at the same time, subtracts the background noise. The method to remove background noise, is to subtract a dark frame, recorded with the shutter closed, from the unprocessed raw frame (*RF*), recorded with the shutter open. In our setup we keep the shutter closed the last three seconds of the recording. This results in a dark area at the end of the picture exhibiting no luminescence signal (dashed rectangle in Figure 3). The background noise level value for each pixel of the camera chip is found as the median value from several successive frames in the dark area. Flø's algorithm used the 10 last successive frames of the recording. In the x, y, λ-coordinate system, this means that the background noise for pixel (x_i, λ_k) on the two-dimensional camera chip is found by taking the median of pixel values from (x_i, y_j, λ_k) to $(x_i, y_{j+10}, \lambda_k)$ in the hypercube. The resulting matrix is in the following referred to as the background noise matrix *(BNM)*, which is our dark frame. The standard dark-frame subtraction scheme can be written as

$$\boldsymbol{CF}(\boldsymbol{y}) = \boldsymbol{RF}(\boldsymbol{y}) - \boldsymbol{BNM}, \quad (3)$$

where *CF* is the corrected frame. An example of an image before and after a standard dark-frame subtraction is shown in Figure 3.

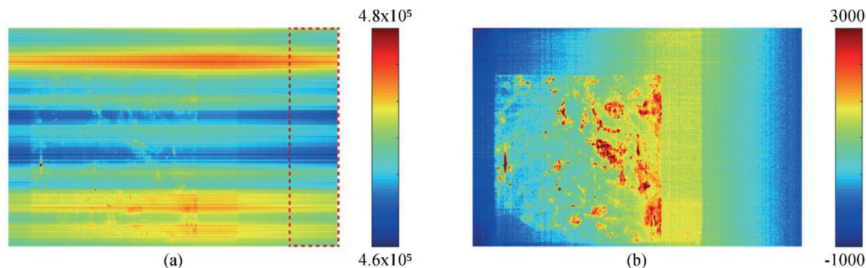

Figure 3 Image (a) is an integral over defect related PL in the range 0.73 – 0.92 eV (wavelength bands 67-124) before, whereas image (b) is after standard dark-frame background noise subtraction. The dashed rectangle in image (a) shows the "dark area" from which the background noise level for each pixel is found. After standard subtraction scheme, a gradient can be seen in the scanning direction (horizontal) of image (b).

In this study, the subtraction of background noise has been modified and an enhanced background noise subtraction scheme has been implemented (**Paper I**).

In addition, a routine to remove most of the impulse noise without compromising the data, by taking the median of corresponding values from three subsequently recorded hyperspectral images has been implemented (**Paper I**). This method was developed during my MSc degree and described in the MSc Thesis[33]. Impulse noise is mainly caused by dead pixels, analog-to-digital converter errors and bit errors in transmission, and is often a temporary disturbance. It can appear as salt-and-pepper grains in a 2D grey scale digital image. In a 3D HSPL image the impulse noise can be observed as stripes in the scanning direction, y, after the dark-frame subtraction. Impulse noise is often removed by general pixel cleaning i.e. spatial and/or spectral median based filters, but used on a HSPL image it may compromise some of the spectral and/or spatial data. Since most of the impulse noise is of temporary nature, a stripe will only appear (partly) in one of subsequent recorded images. In order to remove most of the impulse noise without compromising the data, the median of corresponding values from three subsequently recorded HSPL images is saved in a new hypercube. This new hypercube contains the data used for further analysis.

3.3.2 Multivariate Curve Resolution analysis

In order to extract all the different defect-related emission signals from the hypercube, a mathematical method for deconvolving complex, convoluted signals composed of several discrete, simultaneously occurring signals is needed. To resolve complex dataset into purecomponents where no or little prior information is available, Principal Component Analysis (PCA), Independent Component Analysis (ICA) and MCR are methods that can do this. MCR is chosen as method, because PCA and ICA impose the components profiles to follow

mathematical or statistical constrains, while MCR impose the components profiles to follow physically or chemically meaningful constraints[34]. The most popular and flexible MCR algorithm is Multivariate Curve Resolution by Alternating Least Squares[35] (MCR-ALS). The MCR-ALS algorithm included in the PLS_Toolbox is used in this study. The MCR-ALS method have been used with success to analyze data from hyperspectral imaging[36] and from hyperspectral PL imaging[5].

The mathematical representation of the MCR method can be described by Equation (4).

$$\boldsymbol{D} = \boldsymbol{C}\boldsymbol{S}^{T} + \boldsymbol{E} \tag{4}$$

The measured data, $\boldsymbol{D}$, is decomposed into a number of components, with representative scores in $\boldsymbol{S}^{T}$, and corresponding loading vectors in $\boldsymbol{C}$. The error matrix, $\boldsymbol{E}$, represents the difference between the recorded and the simulated signal. In MCR-ALS, the alternating least squares (ALS) algorithm is used to minimize $\boldsymbol{E}$. The components represent the different radiative defects, with images of the spatial distribution of each defect in $\boldsymbol{S}^{T}$ and their corresponding spectrum in $\boldsymbol{C}$.

As input, the MCR method only requires the measured data and an estimation of components in the dataset. A trial and error approach has been used, based on a qualitative guess of components. A weakness of the MCR method is that it can divide the dataset into too many or too few components. Therefore, it is necessary to check the physical interpretation of each component.

E.g., in MCR, the noise is assumed to be independent and ideally distributed[34]. If the noise has some correlation structure, MCR may give this as one of the output components. De Zan et al.[37] showed that by having a preprocessing step, where the background noise is reduced, the MCR analysis could be greatly improved.

3.3.3 Partial Least Squares Discriminant Analysis

In some cases, the goal is to identify a certain type of defect emission in samples. For this purpose, partial least squares discriminant analysis may be a good tool[38]. PLS-DA is a linear classification method, a derivative of the standard PLS regression that uses class variables instead of numeric variables. In this work, the PLS-DA algorithm in PLS Toolbox is used.

4 Results and discussion

This research has been three-fold. The goals have been to optimize the method, to verify the method and to apply the method. In this section, I will discuss the research leading to the various papers I have included in this thesis.

4.1 Optimization of the method/equipment.

As both the equipment and the method were in an initial stage when I commenced my research, they have been subject to continuous improvements. In this section, I will present the work that was done to improve HSPL.

4.1.1 Algorithm enhancements for better signal-to-noise ratio

Paper I deals with improving the method by improving the quality of the image, especially on the weaker signals. This entails a considerable improvement in image quality. The weak signals are plentiful. This enhancement also improves the possibility of using the MCR analysis.

The method used for subtraction of background noise from the hyperspectral camera, is to use median values obtained from a dark region acquired with a closed shutter during the last three seconds of the recording. Since the hypercube is an assembly of images recorded over a timespan, it shows variations in the noise level due to thermal oscillation in the camera. The standard background subtraction method does not compensate for this oscillation, see Figure 4. For most applications, this is not a problem since the signals are significantly stronger than the background noise oscillation. However, the PL signals from defects in the studied silicon wafers range from a few tens to several thousand counts. Taking into account that the amplitude of the background oscillation can attain a value of more than a hundred counts, defects with the weakest signals might not be detected. In **Paper I**, we demonstrate

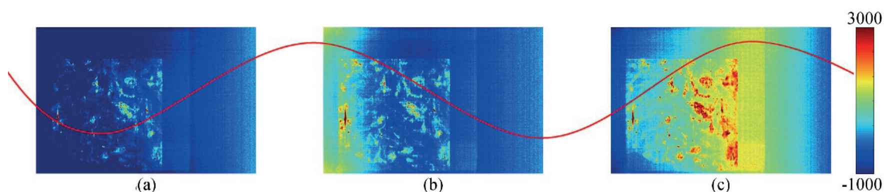

Figure 4 Defect related PL signal from three subsequent measurements; (a), (b) and (c). During measurement (a) and (c), the count rate increases, whereas it decreases during measurement (b). This feature suggests some variable to fluctuate periodically, indicated by a red line.

how it is possible to detect these weak signals by enhancing the background subtraction scheme of the camera.

We discovered that the background oscillation has a period of 45 seconds and the amplitude level varies over the chip surface. Highest amplitude was found in the corners of the chip. A matrix based on the count difference between the highest and lowest possible background noise level, for each camera pixel (x_i, λ_j), was constructed, referred to as the background amplitude correction matrix (BACM). We also identified an area on the chip, which does not record sample related signals during measurements of silicon wafers. Because the variation of counts with time in such an area only would be caused by the oscillation in the background noise level, this area could function as an amplitude reference. Based on the reference area and the BACM, an enhanced background noise subtraction scheme was developed.

For each raw frame, *RF*(*y*), the median number of counts in the reference area is calculated and stored in the raw frame reference, *RFref*(*y*). The background noise matrix reference, *BNMref*, of the measurement is found as the median number of counts in the reference area of the *BNM*. The delta thermal background, *ΔTB(y)*, is defined as the difference between a frame's background noise and the background noise matrix. *ΔTB(y)* holds the extra counts that, due to thermal oscillations, need to be subtracted from each pixel in each raw frame, in addition to the background noise matrix, *BNM*.

In the development of the new scheme we make the following two assumptions. First, we assume that the ratio of the thermal background *ΔTB* to the *BACM* (which is the maximum value of the thermal background oscillation) is equal over the entire camera chip for each frame, expressed in Equation (5).

$$\frac{\Delta TB(x_1, y_1, \lambda_1)}{BACM(x_1, \lambda_1)} = \frac{\Delta TB(x_2, y_1, \lambda_2)}{BACM(x_2, \lambda_2)} = constant \tag{5}$$

Second, we assume that this will also hold for the median values from the reference area.

$$\frac{\Delta TB(x_i, y_j, \lambda_k)}{BACM(x_i, \lambda_k)} = \frac{RFref(y_j) - BNMref}{BACMref} \tag{6}$$

This gives

$$\Delta TB(y) = \frac{RFref(y) - BNMref}{BACMref} \cdot BACM \tag{7}$$

To enhance the background correction scheme, by including subtraction of the extra counts due to thermal oscillations, Equation (3) is modified by inserting Equation (7). *CF* is thus defined as

$$\boldsymbol{CF(y) = RF(y) - BNM - \frac{RFref(y) - BNMref}{BACMref} \cdot BACM} \tag{8}$$

A visualization of the enhanced subtraction scheme is shown in Figure 5.

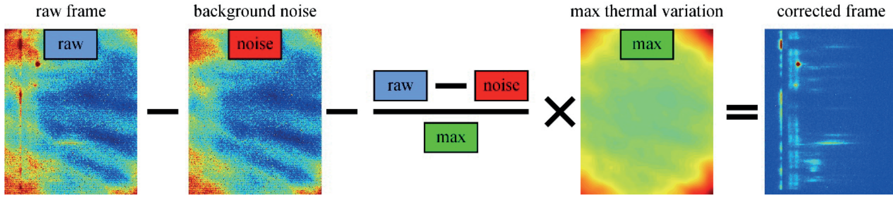

Figure 5 The enhanced subtraction regime; a visualization of Eq. (6). The background noise and the extra counts, due to thermal oscillation, are subtracted. The red, blue and green rectangles symbolize three constants, found from the median of the values from the reference area. The extra counts are calculated using the deviation in the reference area divided by maximum deviation

Images of the three measurements in Figure 4 corrected with the new regime are shown in Figure 6(a-c). With the periodic background noise removed, the possibility to remove most of the impulse noise with use of the median of corresponding values from subsequent recorded images is enhanced. An image of the median of the three recordings is shown in Figure 6(d).

With the enhanced background subtraction scheme, the camera's sensitivity is drastically increased, allowing even weakly emitting defects to be detected.

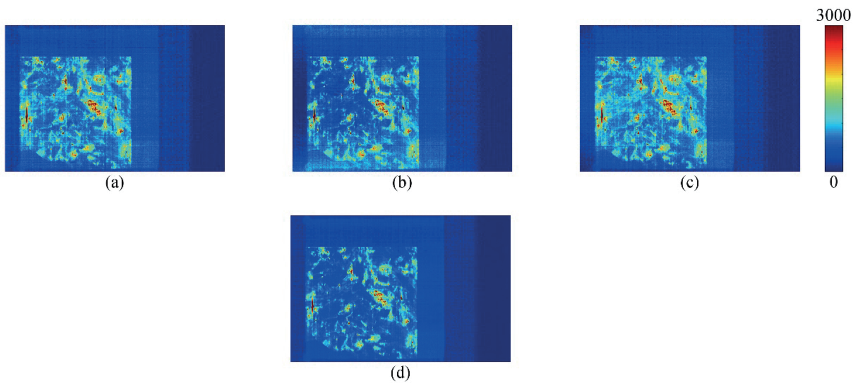

Figure 6 Defect related PL images (0.73 – 0.92 eV) from three subsequent measurements (a-c), made with use of the new background noise subtraction scheme. Image (d) is made from the median of the three measurements (a-c).

4.1.2 Macro lens for higher resolution

Before I started my work, the highest spatial resolution that had been used was 200 µm. When taking pictures of whole 6-inch wafers, the resolution is set to 500 µm. This is usually done first, to get an overview of where there may be interesting areas. Then, these areas can be examined by taking higher resolution images. With the standard lens installed, Flø[5] had previously had a resolution of 200 µm. In this study, I wanted to push the limits of the use of the lens. I first managed to achieve a resolution of 100 µm in the work presented in **Paper III** and then 75 µm in the work presented in **Paper VI**.

We wanted to see if it was possible to get even higher resolution using a macro lens. The results of this experiment are presented in **Paper II**. By using the macro lens, we reached a spatial resolution of 30 µm. It made it possible to locate and investigate single grain boundaries and the corresponding spectral response as a function of the spectral distribution. This is illustrated in Figure 7, where the 30 µm resolution images are shown next to the 500 µm ones for two spectral bands at 0.7 eV and 0.8 eV, respectively. The defect emission at 0.7 eV (left panel, Figure 7) can be seen as spots whereas at the emission at 0.8 eV appear along the grain boundaries (right panel, Figure 7). With these results, it was concluded that the macro lens could be used with HSPL. The macro lens was thus used in the research presented in **Paper VII**, here with a resolution of 27 µm.

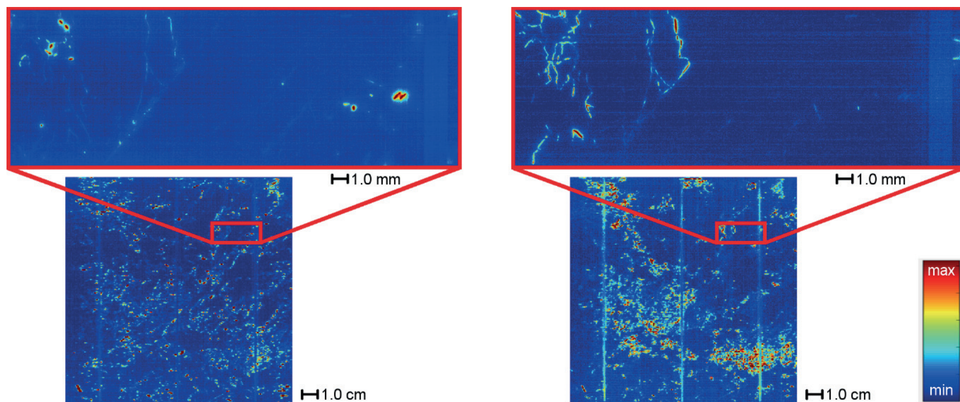

Figure 7 Photoluminescence images of a solar cell for selected emissions. A small region, indicated by a red rectangle, was imaged with a macro lens setup, yielding a spatial resolution of 30 µm. These high resolution images show that some of the defect related signals originate in grain boundaries (0.8 eV, right panel) whereas other signals show up as singular spots (0.7 eV, left panel).

4.1.3 Enhance the analysis technique

To enhance the analysis, we wanted to test if another chemometric analysis technique, PLS-DA, could be used as a tool on HSPL images, to recognize and classify "known" classes.

Flø[2] introduced the use of MCR as a technique to improve the analysis of the hyperspectral images. Score images from MCR analysis showed good agreement with the manually extracted D-band images in the studied wafers. In **Paper II**, we wanted to verify the MCR technique by comparing score images from MCR analysis of a HSPL measurement, Figure 8c), with an EL image from a neighbor sample, Figure 8b).

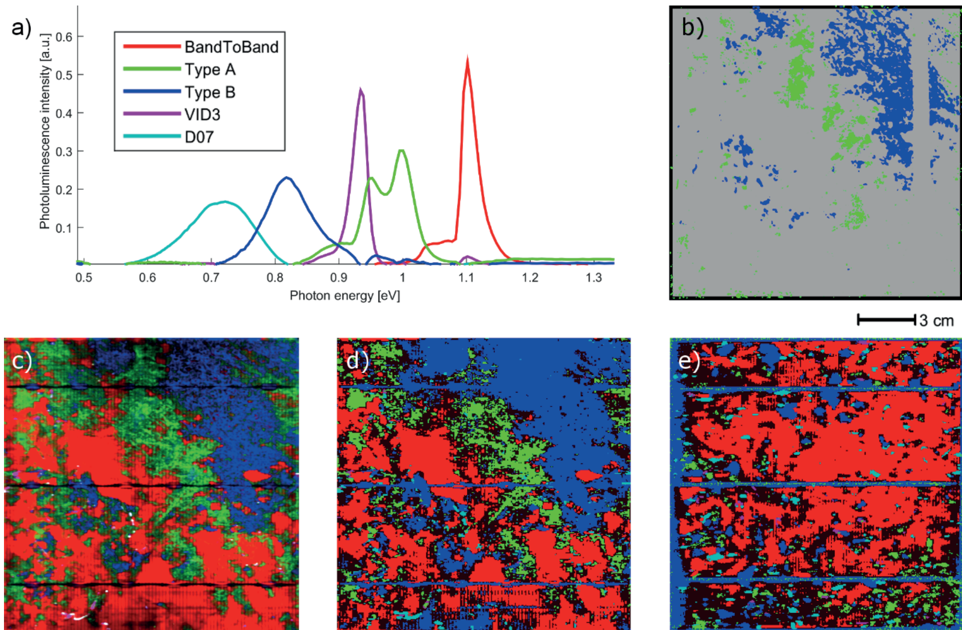

Figure 8 a) MCR loading plot of sample 1. b) Electroluminescence image of neighbor of sample 1. c) MCR score image of sample 1, d) PLS-DA classification sample 1. e) PLS-DA prediction of the different emissions on the unknown sample 2.

Two of the MCR components correspond with two types of defects, named Type A and Type B, found using the electroluminescence method. In addition, two other defects, named D07 and VID3 were clearly detected, as well as the Si band-to-band emission (BB). The spectra of the five components are shown in Figure 8a). The good agreement with the electroluminescence image in this example confirms that hyperspectral photoluminescence imaging with MCR analysis is a well-suited technique applied to silicon wafers and solar cells. A more thorough review of this result is described in Section 4.2.1.

We then introduced another chemometric analysis technique, PLS-DA, to test if the technique is possible to use on HSPL images. The same hyperspectral image was analyzed with PLS-DA where regions of the four defects (type A, B, VID3 and D07) and BB were manually selected as classes and used to construct the PLS-DA model. The resulting classification is shown in Figure 8d) and corresponds well with the results from the MCR analysis. The same

PLS-DA model was then applied to another solar cell, which had not previously been investigated by other methods; see Figure 8e). The five classes of luminescence emission could be identified also in this sample, but we have no complementary measurements for validation for this sample. The model misclassified the busbars as type B defect in both cases. This is due to the presence of second order harmonics of the laser light reflections in the busbars, at 0.77 eV, merging with the signal from type B defect. It seems that PLS-DA can be used as an analytical tool of HSPL images, but further studies are required.

4.1.4 Sample preparation

In connection with EBSD and dislocation mapping, during the research resulting in **Paper IV**, some wafers were going to be polished and etched. What effect this had with regard to HSPL was not known. It was therefore decided to do HSPL both before and after this process. In **Paper IV** it is mentioned that this was done, but the results have been omitted during the editing process, since this was not the main aim of the article. However, I find the results of interest and will therefore present it briefly here.

The samples were first polished down 1 μm before analyzed by EBSD. Then the samples were etched with Sopori etchant before the dislocation density was measured. The polishing and etching process showed a drastic improvement on the HSPL images. The blurring in the image is gone. It is now possible to see in more detail where the signals emit from. Figure 9 shows a picture of defect luminescence from a wafer before and after the polishing and etching process. Further studies need to be done, to determine if both or only one of the processes is needed to give this result.

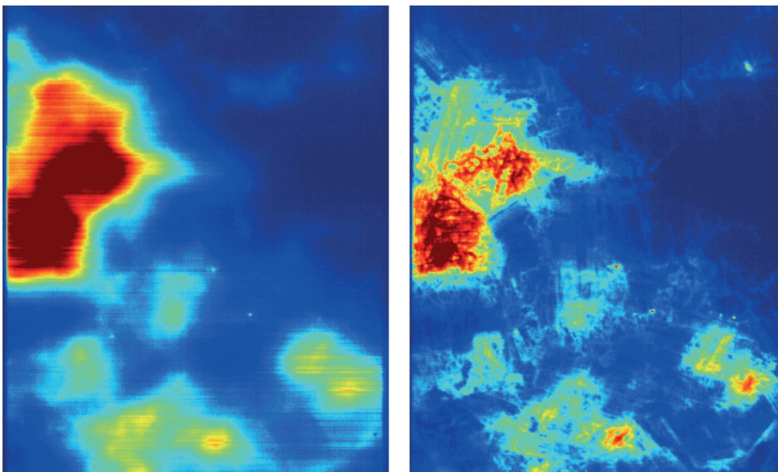

Figure 9 Defect luminescence, 0.7 eV, from a wafer before and after being polished and etched

4.1.5 New long pass filter

Initially (**Paper I – III**), the HSPL setup was equipped with an 850 nm long pass filter to prevent the 808 nm laser beam from entering the optics. Unfortunately, not enough of the laser light was blocked, as reported in the previous section. Either the blocking effect, with an optical density ≥ 4, is not enough or the transition at 850 nm is not sharp enough or too close to 808 nm. Thus, the filter was replaced with a 1000 nm long pass filter with the same optical density. This has improved the measurements; no laser light has been detected in the HSPL images after the replacement (**Paper IV – VII**).

4.2 Verification of the method

In order to verify the HSPL method, it is necessary to correlate the results from HSPL measurements with other complementary material characterization techniques.

4.2.1 HSPL combined with electroluminescence

In **Paper III** we used HSPL on 6-inch mc-Si silicon solar cells and neighboring wafers, and analyzed the images by MCR. This was correlated against results from Lausch et al.[39], who had classified Type-A and Type-B defects on a neighboring solar cell, by using forward electroluminescence and reversed biased electroluminescence (ReBEL)[40] imaging combined with imaging of sub-band defect luminescence. Some of these results were also used in **Paper II**, described in Section 4.1.3.

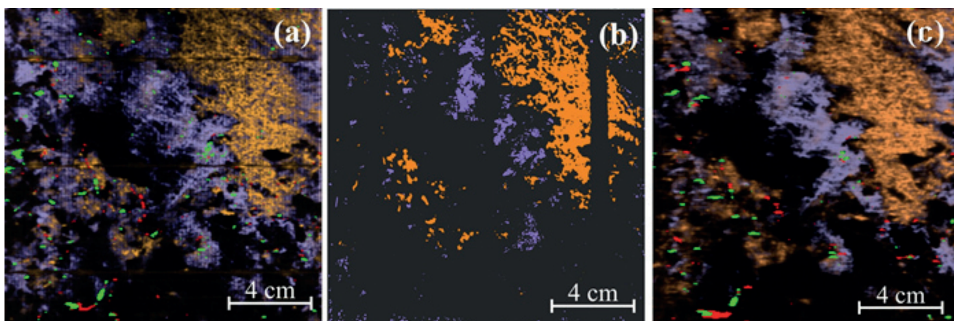

*Figure 10 Classification of defects (a) MCR results from HSPL of a mc-Si solar cell. (b) Classification by forward and reverse biased electroluminescence of a neighbouring solar cell . (c) MCR results from HSPL of a neighbouring wafer. The colours correspond to the defect Type-A – purple, Type-B – orange, Type-D07 – red, Type-VID3 – green. Reproduced from **Paper III**, with the permission of AIP Publishing.*

In Figure 10a) the result from the MCR analysis from a HSPL measurement of a solar cell is shown. Figure 10b) shows the results from defect classification by forward and reverse biased electroluminescence of a neighboring solar cell (busbars rotated 90°). To distinguish Type-A

(purple) and Type-B (orange) defects, Lausch et al.[39] combined electroluminescence results from band-to-band luminescence (> 1.1 eV), defect luminescence (0.73 – 0.85 eV) and pre-breakdown luminescence of type-2 pre-breakdown sites.

Type-A and Type-B defects were identified in both approaches. HSPL with use of MCR algorithm additionally classified D07 and VID3 defects. Type-B defects show the same lateral distribution, but the areas covered by Type-A defects seem smaller using EL methods. The reason for this is likely that the EL method is not detecting all Type-A defects, see discussion in **Paper III**. It is concluded that HSPL is the more reliable method for detection of Type-A defects.

In order to clarify if the specified defect types are already present at wafer level and how they have evolved during the solar cell process, the HSPL procedure is applied to a neighboring as-cut mc-Si wafer of the previous analyzed solar cell. Results from the MCR analysis of the wafer, shown in Figure 10c), reveal that the defects are already present in the wafer material before the solar cell processing starts. It means that Type-A, Type-B, D07 and VID3 defects are bulk material defects and not induced during solar cell processing. By comparing the spatial distribution, only Type-A defects covers slightly more areas in the solar cell compared to the wafer; especially close to the left side of the samples, which is an edge region near the crucible wall. This is due to a slight activation of more Type-A defects during the solar cell processing[41].

Beside the much higher lateral resolution of HSPL, the reproducibility and accuracy is higher due to the usage of the MCR algorithm compared to the manual classification by using electroluminescence methods. **Paper III** also showed that HSPL have an advantage over EL, since the method can be used on as-cut wafer. In addition, HSPL have provided the spectrum of each of the effects, as shown in Figure 8a). As the spectra for Type A and Type B is now known, it is possible to use these spectra for detecting the defects.

4.2.2 HSPL combined with electron backscatter diffraction and dislocation mapping

In **Paper IV**, HSPL measurements was correlated against results from electron backscatter diffraction (EBSD) measurements and dislocation mapping (PVScan by GT Solar), conducted by collaborators at NTNU in Trondheim, Norway. The main purpose of this study was to find spectral response and spatial distribution of iron in mc-Si wafers.

First, HSPL was used to compare n- and p-type samples with and without intentionally introduced Fe. It was found that the p-type wafer enriched with Fe, distinguished from the

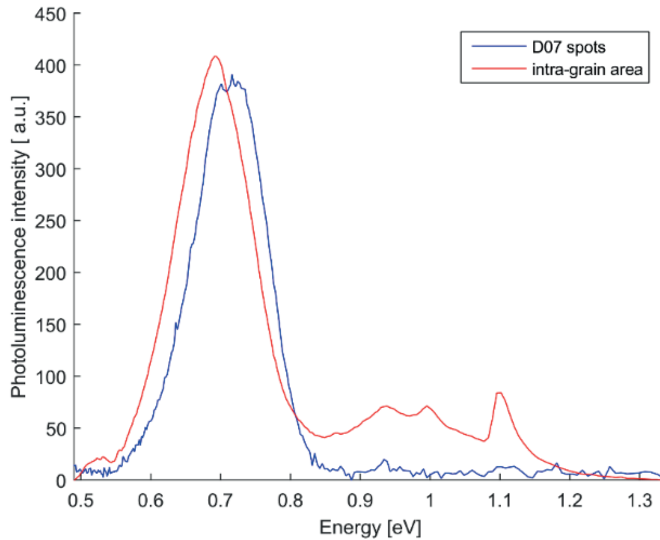

Figure 11 Spectra from intra-grain area (red) with 0.694 eV signal versus D07 spot (blue) in p-type sample with Fe added.

others with a variation, both spectral and spatial, in the PL signal around 0.7 eV. In addition to D07 spots (found in all samples), there were intra-grain areas emitting photons with slightly lower energy, 0.716 eV and 0.694 eV respectively. There are also weak D3/D4 and BB signals emitting from these intra-grain areas, see Figure 11.

The HSPL results were then visually compared with images obtained by EBSD and PVScan. EBSD for mapping of grain orientation and grain boundary types, PVScan for mapping the dislocations density. For all wafers, the D07 spots correlated with grain boundaries, especially Σ9, Σ27 and random GB. For the p-type wafer enriched with Fe, the additional emission signal at 0.694 eV seemed to be strong in regions with high dislocation density. It was concluded that there is reason to believe that a radiative recombination pathway with characteristic photons with energy 0.694 eV is present in this sample due to interstitial iron (Fe_i), while the D3/D4 emission pair is related to the FeB complex.

Since HSPL showed that other defects were present in the samples, we compared also those with the results from EBSD and PVScan, see Figure 12. A detailed description of the correlations, between the different DRL, grain boundaries, grain orientation and dislocation density, can be found in **Paper IV**.

By applying MCR analysis, two of the components were linked to Type A and Type B defects, studied in **Paper III,** and one component to Fe, see Figure 13. From the spatial distribution of Type A and Type B defects, these defects appear to emit from areas with high dislocation

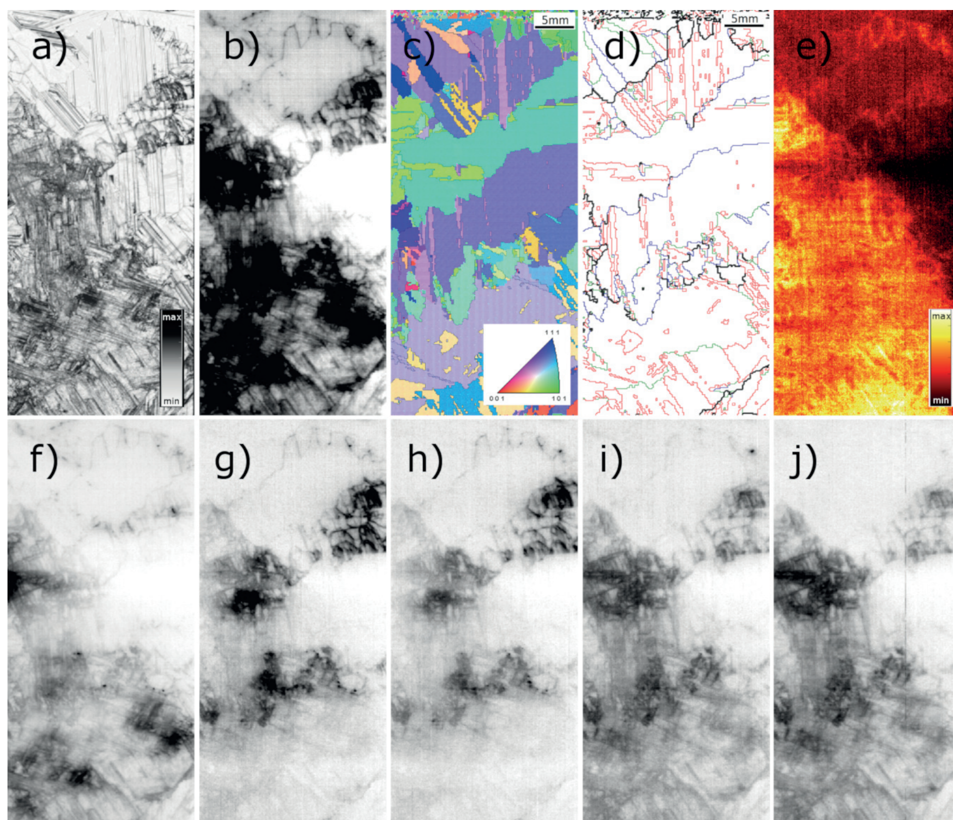

Figure 12 Spatial distribution of features in p-type boron doped mc-Si wafer enriched with Fe. (a) Dislocation mapping, (b) DRL image (integral of signal (0.5–1.0 eV), (c) grain orientation, (d) grain boundary types: Σ3 in red, Σ9 in green, Σ27 in blue and random GB in black. (e) BB PL (1.10 eV). (f) Spatial distribution of D07 (0.694 eV), (g) D1 (0.807 eV), (h) D2 (0.875 eV), (i) D3 (0.943 eV) and (j) D4 (1.00 eV).

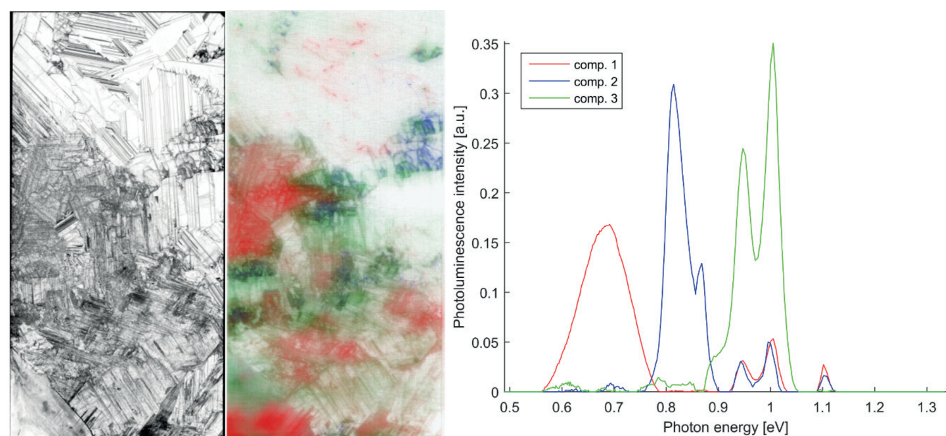

Figure 13 Dislocation density map beside image and graph of three components from an MCR analysis. Comp. 1 (red) Fe related PL. Comp. 2 (blue) Type B. Comp. 3 (green) Type A. Correlation between high dislocation density and spatial distribution of the components are found.

density. It is worth noting that the respective patterns look different. Future studies should try to distinguish between these patterns.

This study showed that comparing measurements from HSPL with EBSD and PVScan is possible and provides new insights into the origin of defects.

4.2.3 Mono crystalline and room temperature

Until this study, presented in **Paper V**, hyperspectral PL imaging had only been used to characterize multicrystalline silicon wafers and solar cells. The technique had never before been used on Cz-Si wafers. Burud et al.[4] used an almost similar setup (equipped with an InGaAs camera) on Cz-Si wafers, but did not detect any other emissions than the BB signal.

In **Paper V**, the aim was to determine the potential of hyperspectral PL imaging to detect heterogeneous distribution of defects/impurities in mono crystalline wafers. For this, oxygen-related Thermal Donors (TD) in n-type Czochralski silicon (Cz-Si) wafers were examined using HSPL at low temperature as well as at room temperature. To verify, the results from HSPL were compared with results from OxyMap measurements, conducted by collaborators at INES-Department of solar technologies at LITEN CEA in Le Bourget-du-Lac, France.

OxyMap[42] is a characterization tool that measure [O_i], [P] and as-grown [TD] across the wafers. It is based on resistivity measurements on as-cut wafers, after controlled generation of TD and after suppression of TD. The technique is destructive, thus was being used on neighbouring wafers of samples we investigated by HSPL.

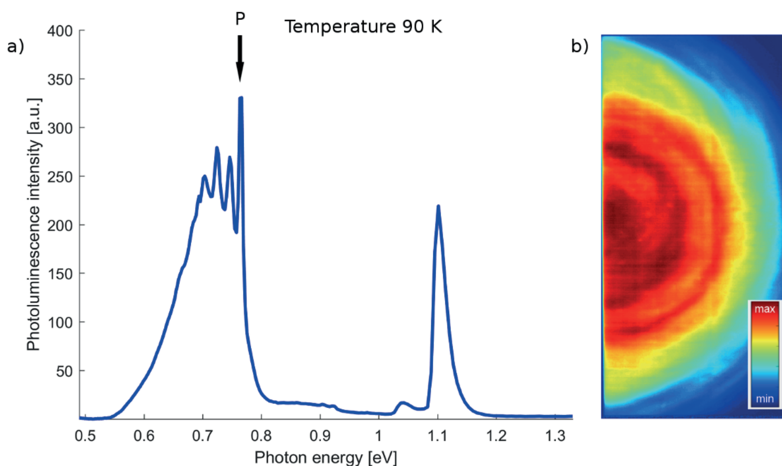

Figure 14 (a) PL spectrum from Cz-Si wafer at T = 90 K. (b) Spatial distribution of the defect related PL integrated over the range 0.66–0.77 eV. This is believed to be caused by TD.

HSPL measurement was carried out on a Cz-Si n-type wafer from the top part (seed-end) of an industrial ingot, at 90 K. This part of the ingot contains the highest [O_i] and is exposed to a rather slow cooling, thus contain TD. Figure 14 shows the PL spectrum and the spatial distribution of the defect related part. The pattern is ring-like and strongest in the centre. This correlates well with the concentration of O_i and TD, obtained by OxyMap, see **Paper V** for further details.

Since the P line, at 0.767 eV in Figure 14, is related to TD[24, 43-45], it can be assumed that the rest of the broad band with center at 0.72 eV also is related to TD[46]. The different local peaks at 90 K can be due to phonon replicas and/or TD with different oxygen–silicon complexes.

The HSPL measurement was repeated at room temperature, 300 K, and the results are shown in Figure 15. Compared with 90 K, the PL signal at 300 K is weaker and missing local peaks, but the broad peak with centre at 0.72 eV is still detected. Its spatial distribution corresponds with the measurement obtained at 90 K, and therefore has the same origin.

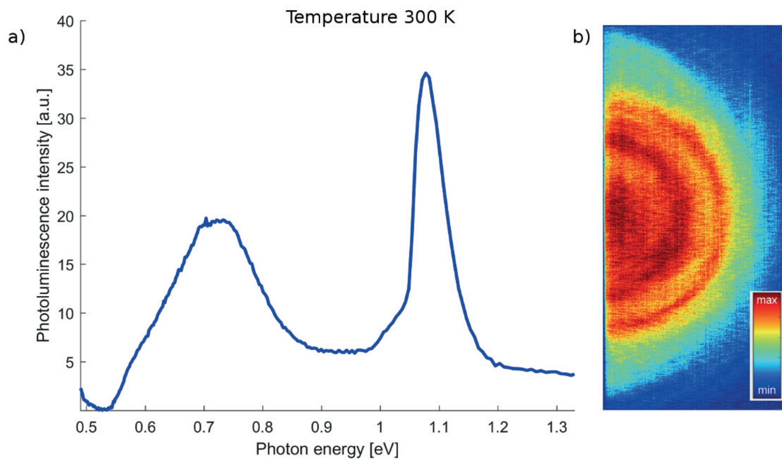

Figure 15 (a) PL spectrum from same sample as shown in Figure 14, now at T = 300 K. (b) Spatial distribution of the defect related PL integrated over the range 0.66–0.77 eV.

Hyperspectral PL imaging thus seems to be a promising tool to detect radiative defects also in Cz-Si. The possibility to detect Thermal Donors at room temperature with hyperspectral photoluminescence imaging is evidenced.

4.2.4 Mono-like wafers

Due to the success of using HSPL for characterization of mono- and multicrystalline Si, we wanted to try the method on mono-like wafers. Mono-like silicon is produced with the goal of increasing wafer efficiency at lesser cost by getting a near-monocrystal by seed-assisted

solidification in a crucible, original used for multicrystalline silicon. The aim of this study was to investigate defect related luminescence emission, especially in dislocated areas above the seed junctions.

Collaborators at NTNU provided samples, cut from various heights in a mono-like ingot. HSPL results were compared with results from their work[31], which included use of, inter alia, light microscopy (LM), scanning electron microscopy (SEM) and conventional non-spectrally resolved photoluminescence. The HSPL measurements were carried out by Simen Bergan as a part of his MSc Thesis[47], with me as a supervisor. Results from this work were published in **Paper VI**.

The study finds the DRL signal to exhibit a correlation with the number of axis with small angle misalignment in the junctions of the seeds. The D1 signal decreases with ingot height, while D2, D3 and D4 are found to increase with ingot height. It is also fund a signal at 0.90 eV above these junctions. In additional, in parasitic crystals growing into the main mono-like ingot from the crucible walls, a signal around 0.7 eV is detected. In the main, mono-like structure, no defect related luminescence was detected. For further details, see **Paper VI**.

4.3 Application of the method

After having optimized and verified the HSPL method, the next step was to use it as a full-fledged tool for characterization of crystalline silicon wafers and solar cells.

4.3.1 Further TD investigations

The findings in **Paper V** were of such interest that the experiment was repeated with new samples. The sample set also includes samples from the tail end of an ingot. The findings in **Paper V** were thus verified. The results are partly published in a conference proceedings[48]. The experiment revealed further findings that have not been published, due to an ongoing patent application with collaborators at INES, France. These findings had to be edited out of the manuscript for the conference proceedings. Unfortunately, these results cannot be presented here either, since the patent application process is not completed.

4.3.2 Study of injection intensity-dependent recombination

In **Paper VII**, which is a part of Felix Frühauf's PhD research, I contributed with HSPL measurements, in the study of some special grain boundaries (GBs). These special GBs may show up as bright lines in an image made from the ratio of two open circuit (conventional

non-spectrally resolved) photoluminescence (V_{oc}-PL) images taken at two different light intensities. This is an indication of distinct injection intensity-dependent recombination properties of these special GBs. Evaluation of V_{oc}-PL images at different illumination intensities concluded that the apparent luminescence ideality factor at the special GBs is about 0.89, whereas it is between 0.94 and 0.95 in the other regions.

To obtain more knowledge of the physical nature of the special GBs showing intensity-dependent recombination and of other GBs not showing this effect, ReBEL, SEM, transmission electron microscopy (TEM) and HSPL imaging were applied.

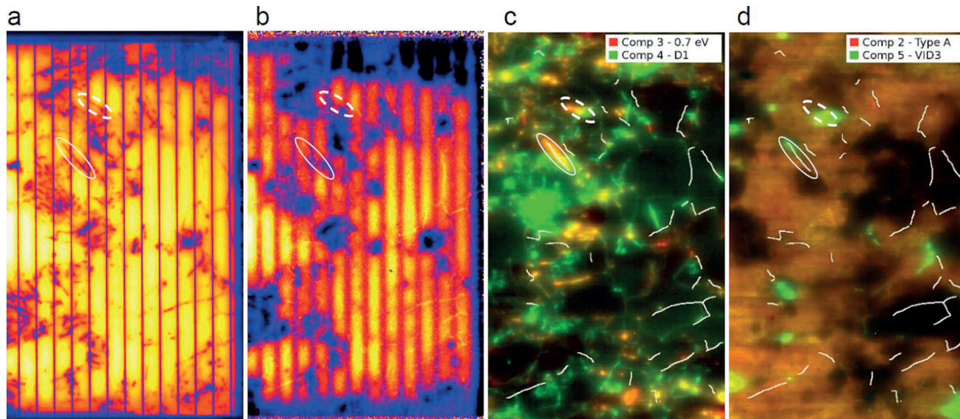

Figure 16 a) V_{oc}-PL image (1 sun) of a region in the second investigated cell. b) ratio of V_{oc}-PL images at 1 and at 0.1 suns intensity. c) HSPL MCR analysis shows in red 0.7 eV (Fe_i?) and green D1 (Type B). d) HSPL MCR analysis shows in red D3&D4 (Type A) and green VID3. In areas where two components are present, the colors blend. The positions of the special GBs showing injection-dependent recombination are marked as white lines.

ReBEL showed no pre-breakdown sites, while HSPL imaging showed only in one of the investigated GBs particular defect luminescence, see Figure 16. SEM measurement shows that a special GB is strongly attacked by the texturing etch, whereas an ordinary GB is only weakly attacked. TEM investigations revealed that the investigated special GB is a large-angle GB whereas the GB not showing this effect is a small-angle GB.

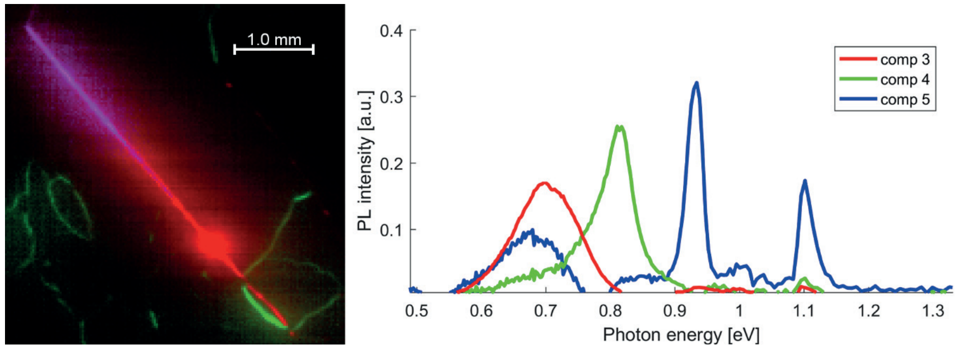

Figure 17 Spatial distribution and respective spectra of components obtained from HSPL MCR analysis of PL from the GB marked by a solid white ellipse in Figure 16. Each component has its own color, but in areas where two or more are present, the colors blend.

In the HSPL measurement, none of the special GBs, marked with white lines in Figure 16, shows any significant defect luminescence, except for the one marked with a solid white ellipse. This exception was investigated further, by applying a macro lens on the HSPL apparatus. Results from the high resolution HSPL, Figure 17, shows an inhomogeneous distribution of three different luminescence components from the GB. This leads to the conclusion that these special GBs are relatively clean ones, hence they obviously show a moderate density of deep level defects, see **Paper VII** for further details.

5 Conclusion

The goal of this research has been to establish hyperspectral photoluminescence imaging as a characterization method for studying defects in wafers and solar cells. The objectives of this research have been three-fold, to optimize the HSPL method, to verify the method and to apply the method.

The first goal was to optimize the HSPL method. Through the discussion of **Paper I**, with the enhanced background noise subtraction scheme, the camera's sensitivity is drastically increased, allowing even weakly emitting defects to be detected. **Paper II** shows how higher resolution was achieved. **Paper IV** shows that by a polishing and etching process a drastic improvement on the HSPL images may be achieved.

The second goal of verification of the method was done by comparing results with other existing methods and on various materials. In **Papers III** through **VI**, the method is verified against other characterization methods. The results show that HSPL correlates well and in some instances yields richer data output.

The third objective of this research was to show that the method might be applied as a characterization method in line with other existing methods. This objective has been achieved as shown in two studies where HSPL has been applied as a characterization method. The study of TD in Cz-Si has even led to a patent application.

This means that HSPL is applicable as a viable method for characterization of solar cell materials. HSPL is a non-destructive method and is considered a fully adequate method that may be used on par with other characterization methods.

6 Further work

Although HSPL may now be used on an equal footing with other characterization methods, there is still room for improvement.

The quality of the HSPL imaging may be improved by replacing the Specim camera with one with better image sharpness and/or lower spatial co-registration between bands. A recent publication[49], where the Specim camera was used and compared, showed that there are other cameras that might provide better results.

Polishing and etching of as-cut wafers showed a drastic improvement on the HSPL images. Thus, we can claim that polishing and etching of samples may advantageously be performed, when wafers are going to be characterized by HSPL. Further studies need to be done, to determine if both or only one of the processes is needed to give this result.

In order to recognize and classify "known" classes of radiative defects, PLS-DA seems promising as an analytical tool of HSPL images. PLS-DA did some misclassifications, thus further studies are required before it can be implemented as an analytical tool.

With minor changes in the hyperspectral setup it will be possible to include electroluminescence, resulting in an equipment that may be use for both HSPL and hyperspectral electroluminescence (HSEL) imaging. In this way one will not only have a new characterization tool for HSEL, but also be able to correlate results from HSPL and EL images with much greater accuracy than what was done in **Paper III**.

Bibliography

1. *International Technology Roadmap for Photovoltaic (ITRPV), 2017 Results*. (2018). Frankfurt: VDMA Photovoltaic Equipment.
2. Flø, A. (2014). *Hyperspectral Imaging as a Tool for Characterization of Multicrystalline Silicon Wafers*. PhD Thesis. Ås: Norwegian University of Life Sciences.
3. Olsen, E. & Flø, A. S. (2011). Spectral and spatially resolved imaging of photoluminescence in multicrystalline silicon wafers. *Applied Physics Letters*, 99 (1): 3. doi: http://dx.doi.org10.1063/1.3607307.
4. Burud, I., Flø, A. S. & Olsen, E. (2012). On the origin of inter band gap radiative emission in crystalline silicon. *AIP Advances*, 2 (4): 7. doi: http://dx.doi.org10.1063/1.4766588.
5. Flø, A., Burud, I., Kvaal, K., Søndenå, R. & Olsen, E. (2013). Distribution of radiative crystal imperfections through a silicon ingot. *AIP Advances*, 3 (11). doi: 10.1063/1.4834155.
6. Flø, A. S., Burud, I. & Olsen, E. (2014). Spatially and Spectrally Resolved Temperature Dependence of Defect Related Luminescence Using Hyperspectral Imaging. *Conference record of the Photovoltaic Specialists Conference*: 1888-1892. doi: http://dx.doi.org10.1109/PVSC.2014.6925293.
7. Green, M. (1982). *Solar cells: operating principles, technology, and system applications*. Kensington, Australia: The University of New South Wales.
8. Nelson, J. (2003). *The physics of solar cells*: World Scientific Publishing Company.
9. Shockley, W. & Queisser, H. J. (1961). Detailed Balance Limit of Efficiency of p-n Junction Solar Cells. *Journal of Applied Physics*, 32 (3): 510-519. doi: 10.1063/1.1736034.
10. Chen, C. J. (2011). *Physics of solar energy*. Hoboken, New Jersey: John Wiley & Sons.
11. Goetzberger, A., Knobloch, J. & Voß, B. (1998). *Crystalline Silicon Solar Cells*. Chichester, England: John Wiley & Sons, Ltd.
12. Shockley, W. & Read Jr, W. (1952). Statistics of the recombinations of holes and electrons. *Physical review*, 87 (5): 835.
13. Tajima, M., Iwata, Y., Okayama, F., Toyota, H., Onodera, H. & Sekiguchi, T. (2012). Deep-level photoluminescence due to dislocations and oxygen precipitates in multicrystalline Si. *Journal of Applied Physics*, 111 (11): 6. doi: 10.1063/1.4728194.
14. Pankove, J. & Tarng, M. (1979). Amorphous silicon as a passivant for crystalline silicon. *Applied Physics Letters*, 34 (2): 156-157.
15. Callister, W. D. & Rethwisch, D. G. (2011). *Materials science and engineering*. 9th ed. ed. New York: Wiley.
16. Zoth, G. & Bergholz, W. (1990). A fast, preparation-free method to detect iron in silicon. *Journal of Applied Physics*, 67 (11): 6764-6771.
17. Graff, K. & Pieper, H. (1981). The properties of iron in silicon. *Journal of the Electrochemical Society*, 128 (3): 669-674.
18. Kimerling, L. C. & Benton, J. L. (1983). Electronically controlled reactions of interstitial iron in silicon. *Physica B+C*, 116 (1): 297-300. doi: https://doi.org/10.1016/0378-4363(83)90263-2.
19. Périchaud, I. (2002). Gettering of impurities in solar silicon. *Solar Energy Materials and Solar Cells*, 72 (1): 315-326. doi: https://doi.org/10.1016/S0927-0248(01)00179-9.

20. Raineri, V. & Campisano, S. (1996). Voids in silicon as sink for interstitials. *Nuclear Instruments and Methods in Physics Research Section B: Beam Interactions with Materials and Atoms*, 120 (1-4): 56-59.
21. Dean, P. J., Haynes, J. R. & Flood, W. F. (1967). New Radiative Recombination Processes Involving Neutral Donors and Acceptors in Silicon and Germanium. *Physical Review*, 161 (3): 711-729. doi: 10.1103/PhysRev.161.711.
22. Drozdov, N., Patrin, A. & Tkachev, V. (1976). Recombination radiation on dislocations in silicon. *Jetp Lett*, 23 (11): 597-599.
23. Binetti, S., Le Donne, A. & Sassella, A. (2014). Photoluminescence and infrared spectroscopy for the study of defects in silicon for photovoltaic applications. *Solar Energy Materials and Solar Cells*, 130: 696-703. doi: 10.1016/j.solmat.2014.02.004.
24. Pizzini, S., Guzzi, M., Grilli, E. & Borionetti, G. (2000). The photoluminescence emission in the 0.7-0.9 eV range from oxygen precipitates, thermal donors and dislocations in silicon. *Journal of Physics-Condensed Matter*, 12 (49): 10131-10143. doi: 10.1088/0953-8984/12/49/312.
25. Ashcroft, N. W. & Mermin, N. D. (1976). *Solid state physics*. New York: Holt, Rinehart and Winston.
26. Viña, L., Logothetidis, S. & Cardona, M. (1984). Temperature dependence of the dielectric function of germanium. *Physical Review B*, 30 (4): 1979-1991. doi: 10.1103/PhysRevB.30.1979.
27. Glunz, S. W., Preu, R. & Biro, D. (2012). 1.16 - Crystalline Silicon Solar Cells: State-of-the-Art and Future Developments. In Sayigh, A. (ed.) *Comprehensive Renewable Energy*, pp. 353-387. Oxford: Elsevier.
28. Sopori, B., Devayajanam, S. & Basnyat, P. (2016). Surface characteristics and damage distributions of diamond wire sawn wafers for silicon solar cells. *AIMS Materials Science*, 3 (2): 669-685. doi: 10.3934/matersci.2016.2.669.
29. Green, M. A. (2008). Self-consistent optical parameters of intrinsic silicon at 300K including temperature coefficients. *Solar Energy Materials and Solar Cells*, 92 (11): 1305-1310. doi: https://doi.org/10.1016/j.solmat.2008.06.009.
30. Schinke, C., Peest, P. C., Schmidt, J., Brendel, R., Bothe, K., Vogt, M. R., Kroger, I., Winter, S., Schirmacher, A., Lim, S., et al. (2015). Uncertainty analysis for the coefficient of band-to-band absorption of crystalline silicon. *Aip Advances*, 5 (6). doi: 10.1063/1.4923379.
31. Ekstrøm, K. E., Stokkan, G., Søndenå, R., Dalaker, H., Lehmann, T., Arnberg, L. & Di Sabatino, M. (2015). Structure and dislocation development in mono-like silicon. *physica status solidi (a)*, 212 (10): 2278-2288. doi: 10.1002/pssa.201532105.
32. DelSolar. (2013). *D6R Multi-crystalline Photovoltaic Cell*. QWMD-03-03-03 Ver. 1.3: DelSolar Co. Ltd.
33. Mehl, T. (2014). *Characterization of Multicrystalline Solar Cells Using Hyperspectral Imaging*. M.Sc. Thesis. Ås: Norwegian University of Life Sciences.
34. Ruckebusch, C. & Blanchet, L. (2013). Multivariate curve resolution: A review of advanced and tailored applications and challenges. *Analytica Chimica Acta*, 765: 28-36. doi: https://doi.org/10.1016/j.aca.2012.12.028.
35. Tauler, R. (1995). Multivariate curve resolution applied to second order data. *Chemometrics and Intelligent Laboratory Systems*, 30 (1): 133-146. doi: https://doi.org/10.1016/0169-7439(95)00047-X.
36. Piqueras, S., Duponchel, L., Tauler, R. & de Juan, A. (2011). Resolution and segmentation of hyperspectral biomedical images by Multivariate Curve Resolution-Alternating Least Squares. *Analytica Chimica Acta*, 705 (1): 182-192. doi: https://doi.org/10.1016/j.aca.2011.05.020.

37. De Zan, M. M., Gil Garcia, M. D., Culzoni, M. J., Siano, R. G., Goicoechea, H. C. & Martinez Galera, M. (2008). Solving matrix-effects exploiting the second order advantage in the resolution and determination of eight tetracycline antibiotics in effluent wastewater by modelling liquid chromatography data with multivariate curve resolution-alternating least squares and unfolded-partial least squares followed by residual bilinearization algorithms I. Effect of signal pre-treatment. *J Chromatogr A*, 1179 (2): 106-14. doi: 10.1016/j.chroma.2007.11.091.
38. Chevallier, S., Bertrand, D., Kohler, A. & Courcoux, P. (2006). Application of PLS-DA in multivariate image analysis. *Journal of Chemometrics: A Journal of the Chemometrics Society*, 20 (5): 221-229.
39. Lausch, D., Petter, K., Henke, B., Bakowskie, R., Schweizer, S. & Hagendorf, C. (2011). Classification of recombination active defect structures in multicrystalline silicon solar cells. *Energy Procedia*, 8: 28-34. doi: 10.1016/j.egypro.2011.06.097.
40. Lausch, D., Petter, K., Wenckstern, H. v. & Grundmann, M. (2009). Correlation of pre-breakdown sites and bulk defects in multicrystalline silicon solar cells. *physica status solidi (RRL) - Rapid Research Letters*, 3 (2-3): 70-72. doi: 10.1002/pssr.200802264.
41. Bakowskie, R., Lantzsch, R., Kaden, T., Eller Karl, G., Lausch, D., Ludwig, Y. & Petter, K. (26th European Photovoltaic Solar Energy Conference and Exhibition, 2010). *Comparison of recombination active defects in multicrystalline silicon by means of photoluminescence imaging and reverse biased electroluminescence*.
42. Veirman, J., Martel, B., Enjalbert, N. & Dubois, S. (2016). Oxygen-defect characterization for improving R&D relevance and Cz-Si solar cell efficiency. *Photovoltaics International*, 33.
43. Minaev, N. S. & Mudryi, A. V. (1981). Thermally-induced defects in silicon containing oxygen and carbon. *Physica Status Solidi a-Applied Research*, 68 (2): 561-566. doi: 10.1002/pssa.2210680227.
44. Uozumi, Y. & Katoda, T. (1997). Effects of stress on generation of P-line defects near insulator-silicon interface. *Applied Surface Science*, 117: 624-628. doi: 10.1016/s0169-4332(97)80154-7.
45. Tajima, M., Stallhofer, P. & Huber, D. (1983). Deep level luminescence ralated to thermal donors in silicon. *Japanese Journal of Applied Physics Part 2-Letters*, 22 (9): L586-L588. doi: 10.1143/jjap.22.L586.
46. Tajima, M. (1990). Characterization of semiconductors by photoluminescence mapping at room temperature. *Journal of Crystal Growth*, 103 (1-4): 1-7. doi: 10.1016/0022-0248(90)90162-e.
47. Bergan, S. (2016). *Defect related radiative recombination in mono-like crystalline silicon wafers*. M.Sc. Thesis. Ås: Norwegian University of Life Sciences.
48. Olsen, E., Kvalbein, L., Helander, M., Mehl, T., Letty, E., Favre, W., Veirman, J. & Burud, I. (2017). *Study of Oxygen in Czochralski Silicon by Hyperspectral Photoluminescence*. 33rd European Photovoltaic Solar Energy Conference and Exhibition, Amsterdam: WIP, München, Germany.
49. Torkildsen, H. E. & Skauli, T. (2018). Full characterization of spatial coregistration errors and spatial resolution in spectral imagers. *Optics Letters*, 43 (16): 3814-3817. doi: 10.1364/OL.43.003814.

Appendix – Papers

Paper I

Mehl, Torbjørn; Wyller, Guro Marie; Burud, Ingunn; Olsen, Espen. *Increased Sensitivity In NIR Hyperspectral Imaging By Enhanced Background Noise Subtraction*. Submitted to Optics Letters

Paper II

Burud, Ingunn; **Mehl, Torbjørn**; Flø, Andreas Svarstad; Lausch, Dominik; Olsen, Espen. *Hyperspectral photoluminescence imaging of defects in solar cells*. Journal of Spectral Imaging 2016; Volume 5.

Paper III

Lausch, Dominik; **Mehl, Torbjørn**; Petter, Kai; Flø, Andreas Svarstad; Burud, Ingunn; Olsen, Espen. *Classification of crystal defects in multicrystalline silicon solar cells and wafer using spectrally and spatially resolved photoluminescence.* Journal of Applied Physics 2016; Volume 119:054501.(5)

Paper IV

Mehl, Torbjørn; Di Sabatino Lundberg, Marisa; Adamczyk, Krzysztof; Burud, Ingunn; Olsen, Espen. *Defects in multicrystalline Si wafers studied by spectral photoluminescence imaging, combined with EBSD and dislocation mapping*. Energy Procedia 2016; Volume 92. p. 130-137

Paper V

Mehl, Torbjørn; Burud, Ingunn; Letty, Elénore; Olsen, Espen. *Oxygen-related defects in n-type Czochralski silicon wafers studied by hyperspectral photoluminescence imaging*. Energy Procedia 2017; Volume 124. p. 107-112

Paper VI

Olsen, Espen; Bergan, Simen; **Mehl, Torbjørn**; Burud, Ingunn; Ekstrøm, Kai Erik; Di Sabatino Lundberg, Marisa. *Defect related radiative recombination in mono-like crystalline silicon wafers*. Physica Status Solidi (a) applications and materials science 2017; Volume 214.(8)

Paper VII

F. Frühauf, P.P. Altermatt, T. Luka, **T. Mehl**, H. Deniz, and O. Breitenstein. *Injection intensity-dependent recombination at various grain boundary types in multicrystalline silicon solar cells*. Solar Energy Materials and Solar Cells 2018; Volume 180. p. 130-137

Paper I

Increased sensitivity in NIR hyperspectral imaging by enhanced background noise subtraction

Torbjørn Mehl[1], Guro Marie Wyller[1,2,3], Ingunn Burud[1], Espen Olsen[1*]

[1]*Department of Mathematical Sciences and Technology, Norwegian University of Life Sciences, Universitetstunet 3, 1433 Ås, Norway*
[2]*Fraunhofer Institute for Solar Energy Systems ISE, Heidenhofstr. 2, 79110 Freiburg, Germany*
[3]*Institute for Energy Technology IFE, Instituttveien 18, 2007 Kjeller, Norway*
**Corresponding author: espen.olsen@nmbu.no*

Received XX Month XXXX; revised XX Month, XXXX; accepted XX Month XXXX; posted XX Month XXXX (Doc. ID XXXXX); published XX Month XXXX

Near-infrared hyperspectral photoluminescence imaging of crystalline silicon wafers can reveal new knowledge on the spatial distribution and the spectral response of radiative recombination active defects in the material. The hyperspectral camera applied for this imaging technique is subject to background shot noise as well as to oscillating background noise caused by temperature fluctuations in the camera chip. Standard background noise subtraction methods does not compensate for this oscillation. Many of the defects in silicon wafers lead to photoluminescence emissions with intensities that are one order of magnitude lower than the oscillation in the background noise level. These weak signals are therefore not detected. In this work, we demonstrate an enhanced background noise subtraction scheme that accounts for temporal oscillations as well as spatial differences in the background noise. The enhanced scheme drastically increases the sensitivity of the camera and hence allows for detection of weaker signals.

OCIS codes: *(110.4234) Multispectral and hyperspectral imaging; (110.4280) Noise in imaging systems; (040.1490) Cameras; (040.6070) Solid state detectors; (120.6810) Thermal effects.*

http://dx.doi.org/10.1364/OL.99.099999

The presence of defects and impurities in silicon wafers for PV applications lead to a significant reduction of the efficiency of the final solar cells. Near-infrared (NIR) hyperspectral imaging of photoluminescence (PL) from radiative recombination active defects is a method that can reveal new knowledge on the spatial distribution and spectral response of these crystal imperfections. In the present work, a NIR hyperspectral pushbroom camera is applied to study radiative defects in wafers and solar cells.

The hyperspectral image (HI) is an assembly of frames recorded over a timespan. Careful temperature control of the detector CCD is needed in order to maintain a steady level of thermal noise. Variation in detector temperature may cause fluctuations in the noise level of the camera. The standard background noise subtraction method does not compensate for this. Normally this is not a problem since the signals are significantly stronger than the background noise variation.

Many of the defects in silicon wafers lead – upon proper excitation – to PL emissions with intensities more than one order of magnitude smaller than the variation in the camera's background noise level. In this work, we demonstrate how it is possible to detect these weak signals by enhancing the background noise subtraction scheme of the camera.

There are three primary sources of noise in a charge-coupled device (CCD) image sensor [1]; shot noise, read noise and dark noise. Shot noise (also called photon noise) is due to the inherent statistical variation in the arrival rate of photons incident on the CCD. The particle nature of light gives the incoming photons a Poisson distribution and the shot noise is thereby the square root of the signal. Read noise is from the digitalization process, where the on-chip preamplifier contributes most. Read noise is added uniformly to every pixel. In the CCD, at temperatures above 0 K, charge carriers will be excited thermally resulting in a thermally dependent current causing a noise signal. The statistical variation of this electron generation is called dark noise, has a Poisson distribution, and is the square root of electrons generated during exposure time.

In addition there can be a background photon flux incident on the CCD due to scattered light from the surroundings. Even with the shutter closed, black body radiation from inside the camera, e.g. the shutter itself, may be recorded due to temperatures above 0 K in the apparatus.

The signal-to-noise ratio (SNR) can then be described by Eq. (1).

$$SNR = \frac{PQ_e t}{\sqrt{(P+B)Q_e t + Dt + N_r^2}} \qquad (1)$$

P is the photon flux from sample, Q_e is the quantum efficiency of the CCD, t is the exposure time, B is the background photon flux, D is the dark current and N_r is the read noise. The sum of these noises is what is referred to as the background noise in this study.

The standard technique for removal of most of the background noise in HIs is to use dark-frame subtraction. The method use median values obtained from a dark region acquired with a closed shutter during recording, and subtract these on all frames.

Impulse noise is mainly caused by dead pixels, analog-to-digital converter errors and bit errors in transmission, and is often a temporary disturbance. It can appear as salt-and-pepper grains in a 2-D grey scale digital image and is often removed by general pixel cleaning i.e. spatial and/or spectral median based filters [2]. Used on a 3-D HI it may compromise some of the spectral and/or spatial data. In a HI the impulse noise can be observed as stripes in the scanning direction, y, after the dark-frame subtraction. Since most of the impulse noise is of temporary nature, a stripe will only appear (partly) in one of subsequent recorded images.

To remove most of the impulse noise without compromising the data, the median of corresponding values from three subsequently recorded HIs is used. In this process, a time dependent additive dark level was detected in the frames. This additive signal has a sinusoidal time variation with a period of approximately 45 s. The present work demonstrates how these variations can be corrected.

PL imaging is a standard technique used for solar cell materials where photoexcitated charge carriers emit photons when they relax to the valence band. As excitation source, the hyperspectral PL setup uses an 808 nm line laser with an irradiated power density of 2 W/cm^2 (Lasiris Magnum II). An 850 nm long-pass filter prevents laser beam reflections from entering the optics.

A NIR hyperspectral camera (SWIR, Specim, Finland), with a HgCdTe detector with a spectral resolution of 6 nm in the range 929–2531 nm (1.33–0.49 eV) is used. The camera records a 14 bits 2-D frame with one 320 pixels spatial dimension (x), and one 256 bands spectral dimension (λ). By assembling frames taken while the camera scans the sample, the second spatial dimension (y) is generated. This setup yields a three-dimensional data file (spatial x, y and spectral λ), called a hypercube. This provides a PL spectrum in each spatial pixel (x,y) of the sample. Images are taken of samples cooled with liquid nitrogen to 90 K. A similar setup has been used in previous studies [3-5]. The scanning speed for PL mapping was approximately 13 mm·s^{-1}.

The sample holder used allows for sample sizes up to (156 mm)^2. The sample used in this study is a (125 mm)^2 multicrystalline silicon wafer. There is thus a 60 pixels wide area outside the edges of the sample where the sample holder's surface is exposed, as seen in e.g. Fig. 1(b). The small sample size was chosen for a better illustration of the background noise.

Since PL from defects in wafers and solar cells are weak signals, images recorded are performed with a shutter time of 20 ms. This leads to a relatively high background noise level. The background noise level is around 9000 counts, while the PL signal is from a few tens to several thousand counts. As shown in Fig. 1, the background noise level is more than one order of magnitude larger than the defect related PL signal. Moreover, the background noise level varies from pixel to pixel.

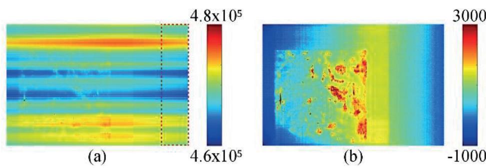

Fig. 1. Image (a) is an integral over defect related PL in the range 0.73 – 0.92 eV (wavelength bands 67-124) before, whereas image (b) is after standard dark-frame background noise subtraction. The dashed rectangle in image (a) shows the "dark area" from which the background noise level for each pixel is found. After standard subtraction scheme, a gradient can be seen in the scanning direction (horizontal) of image (b).

The standard method to remove background noise, is to subtract a *dark frame*, recorded with the shutter closed, from the unprocessed *raw frame*, recorded with shutter open. The dark frame is recorded by keeping the shutter closed during the last part. In our setup we keep the shutter closed the last three seconds. This results in a *dark area* at the end of the picture exhibiting no luminescence signal (dashed rectangle in Fig. 1(a)). The background noise level value for each pixel of the camera chip is found as the median value from several successive frames in the dark area. Here we have used 50 successive frames. In the x, y, λ-coordinate system, this means that the background noise for pixel (x_i, λ_k) on the two-dimensional camera chip is found by taking the median of pixel values from (x_i, y_j, λ_k) to $(x_i, y_{j+50}, \lambda_k)$ in the hypercube. The resulting matrix is in the following referred to as the *background noise matrix (BNM)*, which is our *dark frame*. An example of an image before and after a standard dark-frame subtraction is shown in Fig. 1.

Fig. 1(b) shows a gradient in the image after the standard background noise subtraction (scanning from left to right in horizontal direction). A comparison of three subsequent measurements of the same wafer with equal measurement parameters, is shown in Fig. 2. The count rate seems to increase from left to right during the measurements (a) and (c), whereas it decreases from left to right during measurement (b). This feature suggests that the background noise level fluctuates periodically and regardless of recording start time.

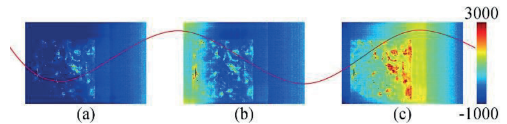

Fig. 2. Defect related PL signal from three subsequent measurements; (a), (b) and (c). During measurement (a) and (c), the count rate increases, whereas it decreases during measurement (b). This feature suggests some variable to fluctuate periodically, indicated by a red line.

Based on Fig. 2, it was suspected that the difference in count rate was caused by fluctuations in the background noise level of the camera detector during the measurements. In order to investigate this, measurements were conducted over a long time interval (200 seconds) with a closed shutter, thus allowing only the background noise level to be recorded. A plot of the count rate for each pixel (x_1, λ_i) for one spatial value, x_1, along the central part of the camera chip as a function of time (Fig. 3), confirmed our suspicion of a periodically oscillating behavior of the background noise. Fig. 3 illustrates both the difference in background noise level from pixel to pixel, and the oscillation of the background noise level for all pixels as a function of time. The oscillation is believed to be caused by the CCD chip temperature control algorithm. The oscillation fits an on/off cooling regime with period, *$T \approx 45$ s*.

With cooling turned off, the temperature will rise, causing the dark noise to increase. When the temperature reaches a certain level, the cooling is activated, causing the temperature, and thus the dark noise level, to decrease. After reaching a certain minimum temperature, the cooling system would again be deactivated.

A hyperspectral PL image with spatial resolution of 500 µm will take approximately 18 seconds to record, when scanning a full size (156 mm)^2 wafer/solar cell. For higher resolution, the recording time increases, e.g. with a resolution of 27 µm, a recording takes more than four minutes. This means that the oscillation will have an impact on the results, especially when the signal intensities are in the same order of magnitude, or lower, than the amplitude of the oscillation.

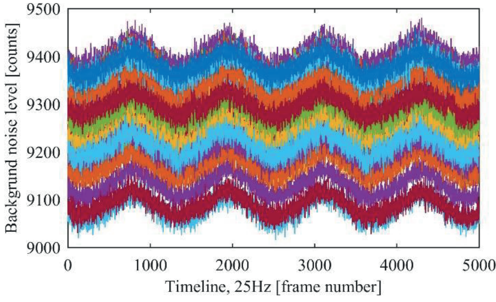

Fig. 3. Oscillations in background noise level. All sensors oscillates with the same period, $T \approx 45\,s$, and are in phase.

The next step was to investigate whether the oscillation in background noise level have the same amplitude for every location on the camera chip. To investigate the pixelwise maximum and minimum of the oscillation, a recording with the shutter closed for more than one period was taken. Based on the difference between the minimum and the maximum value, a matrix with the same dimensions as the camera chip was constructed. For each camera pixel (x_i, λ_j), the corresponding pixel in the matrix (i, j) gives the count difference between the highest and lowest possible background noise level. In the following, this matrix is referred to as the *background amplitude correction matrix* (BACM).

We discovered that the background oscillation amplitude varies over the chip surface. Highest amplitude was found in the corners of the chip (120 counts). In the central area, however, 60 counts were recorded. A visualization of the BACM is seen in Fig. 4.

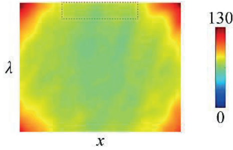

Fig. 4. Visualization of the background amplitude correction matrix (BACM). Each pixel gives the difference between the highest and the lowest background noise level for the corresponding point on the camera chip. The dashed rectangle indicates the reference area of the matrix (see text). The median value for this area is referred to as the background amplitude correction matrix reference (BACMref).

Given that the oscillation in the background noise level has a period of 45 seconds and the hyperspectral PL recording time often is as short as 18 seconds, it is not possible to determine where in the period the recording takes place. It was therefore decided to use another property of the oscillation. Since the amplitude of the oscillations is known and stored in the BACM, it is possible to determine the fraction of the amplitude between two frames in the recording, e.g. between the first and last (the dark) frame. This fraction can be used to compensate for the oscillation.

For this purpose, it is desirable to find an area on the chip which does not record sample related signals during the entire measurement. Because the variation of counts with time in such an area only would be caused by the oscillation in the background noise level, this area could function as an amplitude reference. The dashed rectangle in Fig. 4 indicates such a reference area of the matrix. The median of the values in this area is referred to as the *background amplitude correction matrix reference (BACMref)*. Note that both the matrix BACM and the number BACMref are assumed to be constant; they depend neither on the frame number nor on the sample to be studied. It is to be noted that BACM depends on exposure time, cf. Eq. (1).

Based on the reference area and the BACM, an enhanced background noise subtraction scheme is developed. For each *raw frame*, *RF*(y), the median number of counts in the reference area is calculated and stored in the *raw frame reference*, *RFref*(y). The *background noise matrix reference, BNMref*, of the measurement is found as the median number of counts in the reference area of the *BNM*. The *delta thermal background, ΔTB(y)*, is defined as the difference between a frame's background noise and the background noise matrix. *ΔTB(y)* holds the extra counts that, due to thermal oscillations, need to be subtracted from each pixel in each raw frame, in addition to the *BNM*.

In the development of the new scheme we make the following two assumptions. First we assume that the ratio of the thermal background *ΔTB* to the *BACM* (which is the maximum value of the thermal background oscillation) is equal over the entire camera chip for each frame, expressed in Eq. (2).

$$\frac{\Delta TB(x_1,y_1,\lambda_1)}{BACM(x_1,\lambda_1)} = \frac{\Delta TB(x_2,y_1,\lambda_2)}{BACM(x_2,\lambda_2)} = constant \qquad (2)$$

Then we assume that it will also hold for the median values from the reference area.

$$\frac{\Delta TB(x_i,y_j,\lambda_k)}{BACM(x_i,\lambda_k)} = \frac{RFref(y_j)-BNMref}{BACMref} \qquad (3)$$

This gives

$$\Delta TB(y) = \frac{RFref(y)-BNMref}{BACMref} \cdot BACM \qquad (4)$$

The standard dark-frame subtraction scheme can be written as

$$CF(y) = RF(y) - BNM, \qquad (5)$$

where *CF* is the *corrected frame*. To enhance the background correction scheme, by including subtraction of the extra counts due to thermal oscillations, *ΔTB(y)*, Eq. (5) is modified by inserting Eq. (4). *CF* is then defined as

$$CF(y) = RF(y) - BNM - \frac{RFref(y)-BNMref}{BACMref} \cdot BACM \qquad (6)$$

Eq. (6) holds the enhanced scheme and is shown in Fig (5).

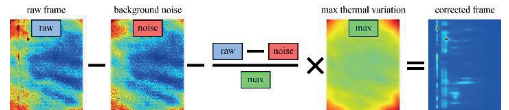

Fig. 5. The enhanced subtraction regime; a visualization of Eq. (6). The background noise and the extra counts, due to thermal oscillation, are subtracted. The red, blue and green rectangles symbolize three constants, found from the median of the values from the reference area. The extra counts are calculated using the deviation in the reference area divided by maximum deviation.

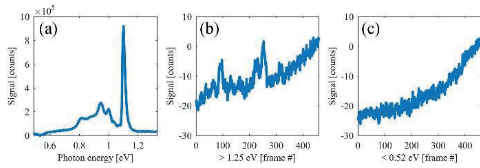

Fig. 6. (a) Total spectrum from a hyperspectral PL measurement of a mc-Si wafer. (b) Mean number of counts for wavelength bands 1-10, photon energies >1.25 eV, and (c) for bands 237-256, photon energies <0.52 eV, as function of frame number. Note that the frame numbers can be seen as a time dimension. Bands 237-256 receive no signal, only thermal oscillation. Thus, this is used as reference area.

When measuring silicon wafers, the reference area can either be taken from the part of the chip which detects light with energy higher than the bandgap of silicon (1.1 eV), or from the part detecting light with energy lower than the defect signals. Further investigation of photon energies > 1.25, eV, band 1-10, as function of frame number, shows that there are some weak signals, see Fig. 6(b). Thus, these bands cannot be used as reference area. For bands 237-256, corresponding to photon energies < 0.52 eV, we conclude that there is no signal from the sample, see Fig. 6(c). These bands can thus be used as a reference area. The shutter is closing at frame 390 and a small increase in counts is observed. This is presumably black body radiation from the shutter itself.

Since the values in the corners of BACM differs from the middle part of the matrix, only x-values from 70 to 250 were used as reference area, as seen in Fig. 4.

To evaluate the new subtraction scheme, we made a comparison with the old, using the three subsequent measurements shown in Fig. 2. By looking at weak 0.70 eV PL-signals from defects detected by band 136, the mean number of counts for all x-values as a function of frame number is calculated from both the standard and the new subtraction regime of three measurements, see Fig. 7.

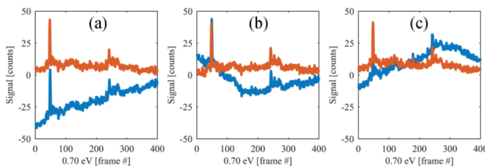

Fig. 7. Weak PL-signals from defects detected by band 136 (0.70 eV). Mean number of counts for all x-values as a function of frame number, shown with both standard (blue) and new (red) subtraction regime of three subsequent measurements; (a), (b) and (c).

The possibility to detect and study weak signals in the measurements has increased drastically. The periodic oscillation is removed and the signal from the sample is more reproducible (Fig. 7). This indicates that the assumption made in the description of the background correction procedure above, seems to hold true.

Images of the three measurements (Fig. 2) corrected with the new regime are shown in Fig. 8(a-c). Before the correction, the periodic oscillation with an amplitude of 60-120 counts gave the limitations of detection. With the new regime, the periodic signal is removed and the detection limit is set by only the standard deviation of the shot noise, which in the demonstrated case is 14 counts.

With the periodic background noise removed, the possibility to remove most of the impulse noise with use of the median of corresponding values from subsequent recorded images is enhanced. An image of the median of the three recordings is shown in Fig. 8(d). Also the detection limit is enhanced. The standard deviation in the background noise is reduced to 6 counts in the median image.

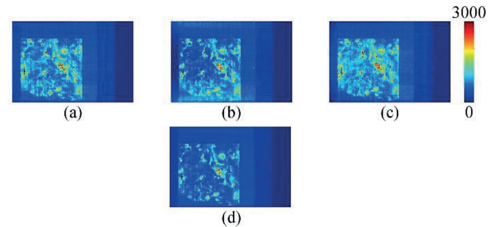

Fig. 8. Defect related PL images (0.73 – 0.92 eV) from three subsequent measurements (a-c), made with use of the new background noise subtraction scheme. Image (d) is made from the median of the three measurements (a-c).

In summary, a thermal oscillation causing a temporal variation in the background noise level of the hyperspectral camera is identified. An enhanced background noise subtraction scheme to correct for this has been developed. The PL signals from defects in the studied silicon wafers range from a few tens to several thousand counts. Taking into account that the amplitude of the background oscillation can attain a value of more than a hundred counts, defects with the weakest signals might not be detected. With the enhanced background subtraction scheme, the camera's sensitivity is drastically increased, allowing even these weakly emitting defects to be detected.

Acknowledgment. This study has been a part of the FME - SuSolTech center for renewable energy technology sponsored by the Norwegian Research Council together with Norwegian industrial partners.

REFERENCES

1. T.J. Fellers, M.W. Davidson, CCD Noise Sources and Signal-To-Noise Ratio (2015) https://micro.magnet.fsu.edu/primer/digitalimaging/concepts/ccdsnr.html
2. S. H. Teoh and H. Ibrahim, IJFCC, **1**, 4, (2012), p. 323
3. E. Olsen and A.S Flø, Appl. Phys. Lett. **99,** (2011), 011903
4. D. Lausch, et al., J. Appl. Phys. **119** (2016) 054501
5. I. Burud, et al., J. Spectral Imaging, **5** (2016), a8

FULL REFERENCES

[1] T.J. Fellers, M.W. Davidson, *CCD Noise Sources and Signal-To-Noise Ratio*, Olympus America, Inc. and The Florida State University (13 Nov. 2015) Retrieved from URL https://micro.magnet.fsu.edu/primer/digitalimaging/concepts/ccdsnr.html (accessed 14.04.18).

[2] S. H. Teoh and H. Ibrahim, *Median filtering frameworks for reducing impulse noise from grayscale digital images: A literature review,* International Journal of Future Computer and Communication, **1**, 4, (2012), pp. 323-326.

[3] E. Olsen* and A.S. Flø, *Spectral and spatially resolved imaging of photoluminescence in multicrystalline silicon wafers*, Applied Physics Letters, **99**, 1, (2011), 011903.

[4] D. Lausch, T. Mehl, K. Petter, A.S. Flø, I. Burud, E. Olsen, *Classification of crystal defects in multicrystalline silicon solar cells and wafer using spectrally and spatially resolved photoluminescence*, Journal of Applied Physics **119,** (2016), 054501.

[5] I. Burud, Mehl, T., Flø, A.S, Lausch, D., Olsen, E., *Hyperspectral photoluminescence imaging of defects in solar cells*. Journal of Spectral Imaging, **5**, (2016) a8.

Paper II

Received: 1 August 2016 ■ *Accepted: 25 November 2016* ■ *Publication: 3 December 2016*

Paper Presented at IASIM 2016, July 2016, Chamonix, France

openaccess

Hyperspectral photoluminescence imaging of defects in solar cells

Ingunn Burud,[a,*] Torbjørn Mehl,[a] Andreas Flo,[a] Dominik Lausch[b] and Espen Olsen[a]

[a]Norwegian University of Life Sciences, Department of Mathematical Sciences and Technology, Campus Ås, Pb 5003, 1433 Ås, Norway. E-mail: ingunn.burud@nmbu.no

[b]Fraunhofer-Center für Silizium Photovoltaik CSP Otto-Eißfeldt-Straße 12, 06120 Halle (Saale), Germany

The present work is a demonstration of how near infrared (NIR) hyperspectral photoluminescence imaging can be used to detect defects in silicon wafers and solar cells. Chemometric analysis techniques such as multivariate curve resolution (MCR) and partial least squares discriminant analysis (PLS-DA) allow various types of defects to be classified and cascades of radiative defects in the samples to be extracted. It is also demonstrated how utilising a macro lens yields a spatial resolution of 30 µm on selected regions of the samples, revealing that some types of defect signals originate in grain boundaries of the silicon crystal, whereas other signals show up as singular spots. Combined with independent investigation techniques, hyperspectral imaging is a promising tool for determining origins of defects in silicon samples for photovoltaic applications.

Keywords: near infrared, photovoltaic, multicrystalline silicon, MCR, PLS-DA

Introduction

Material defects in silicon wafers for photovoltaic (PV) applications can lead to significant reduction in the efficiency of the final solar cells due to a decrease in charge carrier lifetime. Uncovering these defects and the physical mechanisms behind them have high priority internationally in order to increase conversion efficiency. In-depth knowledge of material defects would allow crystallisation processes to be optimised and new methods to be developed to upgrade low quality wafers to yield solar cells with higher overall efficiencies.

Photoluminescence (PL) imaging without spectral resolution is a well-established, non-destructive technique for characterising multicrystalline silicon wafers and solar cells.[1,2] A traditional PL image will display good areas with high lifetime of charge carriers with high photoluminescence intensity, and low lifetime (bad areas) with low intensity. The high intensity photoluminescence is a result of recombination between the valence band and conduction energy band for silicon, also called the band-to-band (BB) recombination. Spectral information has traditionally been obtained only from selected points on the wafer through near infrared (NIR) photoluminescence spectroscopy. Characteristic emission signals in these spectra are supposedly related to dislocations and are named D-lines.[3] With hyperspectral photoluminescence imaging, both spatial and spectral distribution of the crystal imperfections across the whole wafer can be studied, as shown by Olsen & Flo[4] and Burud *et al.*[5]

In this work, we demonstrate how NIR hyperspectral photoluminescence imaging of silicon wafers and solar cells combined with multivariate image analysis techniques, such as multivariate curve resolution (MCR) and partial least squares discriminant analysis (PLS-DA), can be used to extract and to map a cascade of radiative defects in multicrystalline silicon samples. Moreover, we show how utilising a macro lens yields a spatial resolution of 30 µm on selected regions of the samples, revealing detailed information on the defects.

ISSN: 2040-4565
doi: 10.1255/jsi.2016.a8
© 2016 The Authors
This licence permits you to use, share, copy and redistribute the paper in any medium or any format provided that a full citation to the original paper in this journal is given, the use is not for commercial purposes and the paper is not changed in any way.

Materials and method

Samples

The samples named 1, 2 and 3 in this article are multicrystalline Si solar cells, fabricated with a standard commercial process based on boron-doped $156 \times 156\,mm^2$ wafers made from standard electronic grade silicon with comparable high purity.

Hyperspectral photoluminescence imaging

Photoluminescence imaging is based on the characteristic of a material, typically a semiconductor, that enables it to emit light in response to a light source with energy high enough to excite electrons from the valence band to the conduction band. Hyperspectral photoluminescence imaging of samples 1, 2 and 3 were obtained using a NIR hyperspectral pushbroom camera (SWIR, Specim, Finland) with a HgCdTe detector with spectral sensitivity in the 929–2531 nm (0.49–1.33 eV) range and a resolution of 6 nm (256 bands). As excitation source, an 808 nm line laser was used with an irradiated power density of $2\,W\,cm^{-2}$ (Lasiris Magnum II). The laser has enough energy to excite the electrons from the valence band to the conduction band and the photoluminescence light that we measure results from all radiative recombinations of electrons to the valence band with energy larger than 0.49 eV. A 850 nm low-pass filter prevented laser beam reflections from entering the optic apparatus. The samples were cooled to 90 K on a polished aluminium surface on top of a cryogenic cooler filled with liquid nitrogen. The cooling quenches some of the non-radiative emissions and hence enhances the luminescent active imperfections. For most applications, the spatial resolution is around 500 µm. A macro lens was also used which yields an increased resolution to 30 µm. The hyperspectral imaging setup is shown schematically in Figure 1. This setup yields a three-dimensional data file (spatial x, y and spectral λ), called a hypercube.

Electroluminescence imaging

Electroluminescence imaging is similar to photoluminescence imaging except that the excitation source is an electrical current. Spectrally integrated electroluminescence images were acquired of sample 1. The images were obtained at room temperature using a camera with a charge coupled device (CCD) camera in order to detect band-to-band (with a Si detector) and sub-band defect luminescence (using an InGaAs detector).

Image analysis

In order to extract all the different defect related emission signals from the hypercube, MCR[6] was used. MCR is a mathematical method for deconvolving complex, convoluted signals composed of several discrete, simultaneously occurring signals. An iterative process optimises the best fit by an alternating least squares (ALS) algorithm. For each of the samples studied, an MCR analysis was carried out on the hypercube of 256 photoluminescence images. In some cases, the goal is to identify a certain type of defect emission in samples. For this purpose, PLS-DA could also be applied. PLS-DA is a linear classification method, a derivative of the standard PLS regression that uses class variables instead of numeric variables. In this work, the PLS-DA algorithm in PLS Toolbox (eigenvector.com) under the MATLAB environment was used. On the hypercube of sample 1, regions of Type A, Type B and BB signal [108 spaxels (pixel spectra)] and small spots of VID3 and D07 (9 spaxels) were manually selected, and the PLS-DA model was applied to all the other spaxels in the hypercube. The same PLS-DA model was then applied to an unknown solar cell, named sample 2. Unfortunately, we have no complementary measurements for validation of this sample.

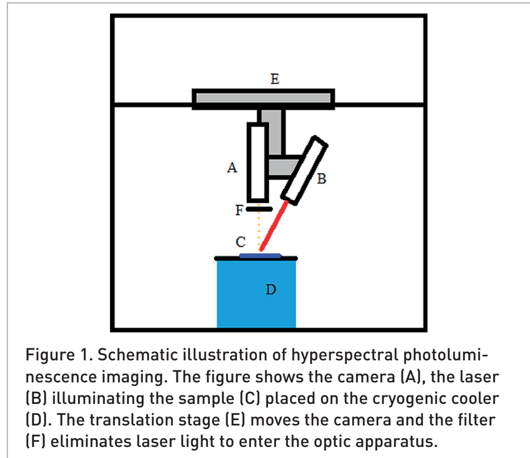

Figure 1. Schematic illustration of hyperspectral photoluminescence imaging. The figure shows the camera (A), the laser (B) illuminating the sample (C) placed on the cryogenic cooler (D). The translation stage (E) moves the camera and the filter (F) eliminates laser light to enter the optic apparatus.

Results and discussion

Classification of defects

The results from the MCR analysis of a solar cell (sample 1) are shown in Figure 2 together with an electroluminescence image of a neighbouring sample[7,8] (coming from the same location in the silicon block from which they were cut). The loading plot in units of energy volts is shown in Figure 2a). The electroluminescence image (Figure 2b) can be compared with the score images for five components laid on top of each other, each with its own colour (Figure 2c). Two of the MCR components correspond to the two types of defects, named Type A and Type B that were found with the electroluminescence method. In addition, two other defects previously found in other samples and named D07 and VID3 were clearly detected, as well as the Si BB emission. In some pixels, there are slight overlaps between defect-related emission, and the most dominant is seen in the image in the figure. However, the defects classified as Type A and Type B are very distinct in their location, and hardly any overlap of these emission signals are found.

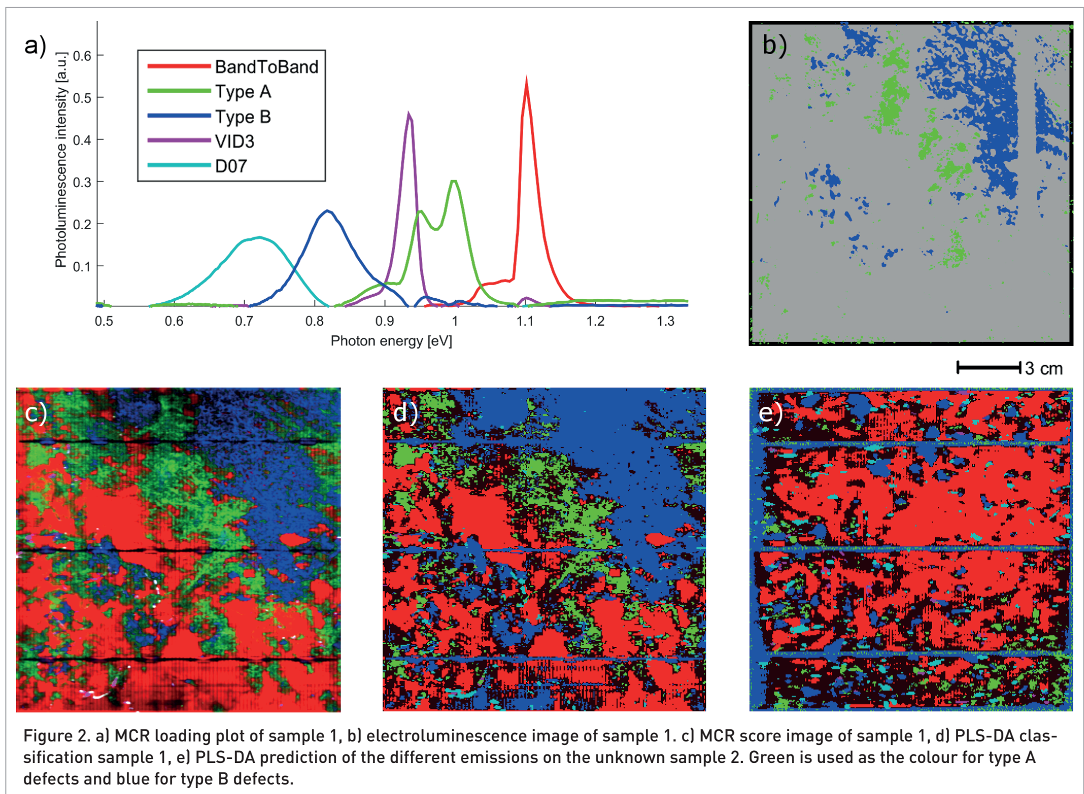

Figure 2. a) MCR loading plot of sample 1, b) electroluminescence image of sample 1. c) MCR score image of sample 1, d) PLS-DA classification sample 1, e) PLS-DA prediction of the different emissions on the unknown sample 2. Green is used as the colour for type A defects and blue for type B defects.

The same hyperspectral image was analysed with PLS-DA where regions of the four defects (type A, B, VID3 and D07) and BB were manually selected as classes. These selected regions were used to construct the PLS-DA model. The resulting classification is shown in Figure 2c and corresponds well with the results from the MCR analysis. The good agreement with the electroluminescence image in this example confirms that hyperspectral NIR photoluminescence imaging with MCR analysis is well-suited for application to silicon wafers and solar cells. Moreover, electroluminescence uses current to excite electrons and can only be carried out on finished solar cells with busbars mounted to conduct the electricity. Busbars are thin strips of silver that are screen printed onto the cells to collect and conduct the current generated by the solar cell. They can be seen as horizontal lines in Figure 2. Hyperspectral imaging, however, is not dependent on current since it uses the laser light to excite the electrons.

The PLS-DA model described above was also applied to another cell (sample 2) that has not previously been investigated by other methods. The five classes of luminescence emission could be identified also in sample 2. It can be seen that the busbars and the edges of the sample are misclassified as type B defect. This is due to the presence of second order harmonics of the laser light reflections in the busbars, at 0.77 eV, merging with the signal from type B defects. This indicates that the low-pass filter is not preventing all laser light entering the camera lens. Laser light (808 nm) will not be detected by the camera (929–2531 nm), but second order harmonics (1616 nm / 0.77 eV), generated in the optics, will. A new low-pass filter at 1000 nm has now improved this for future measurements.

Cascade of energy levels

According to the physics of recombination mechanism, one would expect defect-related emissions with many similar but slightly different energy levels, almost as a cascade of energy levels. It is therefore interesting that if one applies an MCR analysis with many components, a distribution of such energy levels is found, as shown in Figure 3 where the MCR loading plot and the score images for 11 components are shown for sample 3. When looking at the score images, one sees that all the defect emission signals have different spatial distributions. These results indicate that the classification of defects such as type A, B and D-band lines are only on a macroscopic level. Investigations using independent techniques have to be carried out in order to reveal the possible different origins of these signals.

Figure 3. MCR loadings and score images with 11 components of sample 3. Each component has its own colour, but in areas where two or more are present, the colours blend. a) loading plot, b) score images of components identified as BB luminescence, D4 and D1, c) score images with signals at 0.70 eV and 0.75 eV, d) score images of 0.80 eV, 0.84 eV and 0.88 eV, e) three of the peaks centred around 0.94 eV, often called *Very Intense D3* (VID3).

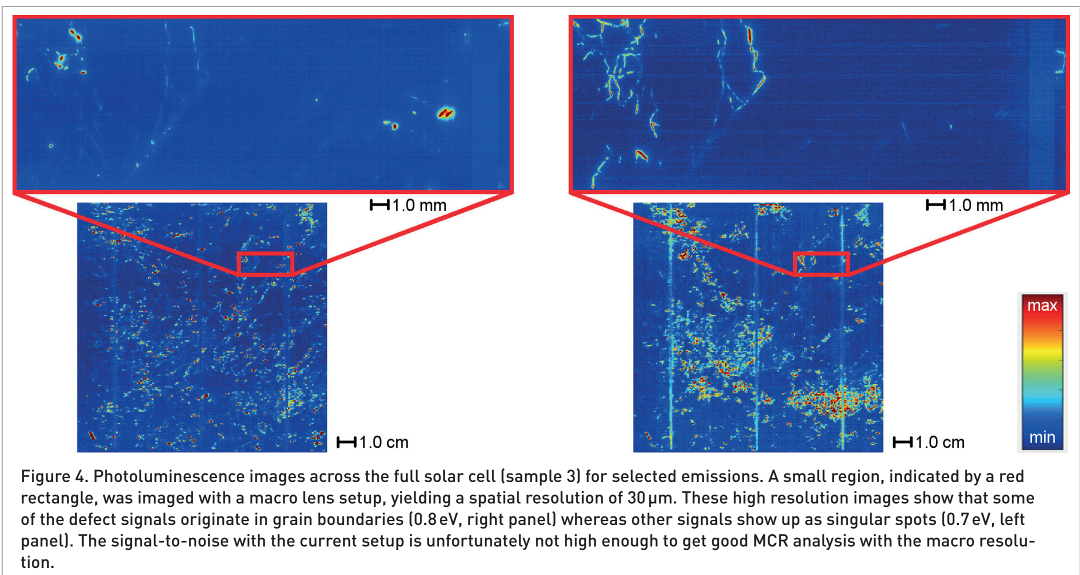

Figure 4. Photoluminescence images across the full solar cell (sample 3) for selected emissions. A small region, indicated by a red rectangle, was imaged with a macro lens setup, yielding a spatial resolution of 30 μm. These high resolution images show that some of the defect signals originate in grain boundaries (0.8 eV, right panel) whereas other signals show up as singular spots (0.7 eV, left panel). The signal-to-noise with the current setup is unfortunately not high enough to get good MCR analysis with the macro resolution.

Macro resolution

Using the macro-lens on the camera and reaching a spatial resolution of 30 μm makes it possible to locate and investigate single grain boundaries and the corresponding spectral response as a function of the spectral distribution. This is illustrated in Figure 4 where the 30 μm resolution images are shown next to the 500 μm ones for two spectral bands at 0.7 eV and 0.8 eV, respectively. The defect emission at 0.7 eV can be seen as spots, whereas the emission at 0.8 eV appears along the grain boundaries.

Conclusion

This work shows that NIR hyperspectral photoluminescence imaging can be used for characterisation of silicon solar cells. Whereas as more traditional methods of characterisation are often long and destructive, hyperspectral imaging allows one to identify and classify defects across the whole sample in a fast and non-destructive way. Moreover, MCR analysis can be used to detect new defect emission lines. Finally, it has been demonstrated how hyperspectral imaging with macro resolution (30 μm) reveals information on certain defects. Additional measurements with independent techniques, such as micro-XRF and dislocation mapping will be carried out extensively to determine the origins of the defects.

References

1. T. Trupke, R.A. Bardos, M.C. Schubert and W. Warta, "Photoluminescence imaging of silicon wafers", *Appl. Phys. Lett.* **89,** 044107 (2006). doi: https://doi.org/10.1063/1.2234747
2. T. Trupke, E. Pink, R.A. Bardos and M.D. Abbot, "Spatially resolved series resistance of silicon solar cells obtained from luminescence imaging", *Appl. Phys. Lett.* **90,** 093506 (2007). doi: https://doi.org/10.1063/1.2709630
3. N.A. Drozdov, A.A. Patrin and V.D. Tkachev, "Recombination radiation on dislocations in silicon," *JETP Lett.* **23(11),** 597 (1976). http://jetpletters.ac.ru/ps/1806/article_27602.pdf
4. E. Olsen and A.S. Flø, "Spectrally and spatially resolved imaging of photoluminescence in multicrystalline silicon wafers", *Appl. Phys. Lett.* **99,** 011903 (2011). doi: https://doi.org/10.1063/1.3607307
5. I. Burud, A.S. Flø and E. Olsen, "On the origin of inter band gap radiative emission in crystalline silicon", *AIP Advances* **2,** 042135 (2012). doi: https://doi.org/10.1063/1.4766588
6. R. Tauler, "Multivariate curve resolution applied to second order data", *Chemometr. Intell. Lab. Syst.* **30,** 133–146 (1995). doi: https://doi.org/10.1016/0169-7439(95)00047-X
7. D. Lausch, K. Petter, B. Henke, R. Bakowskie, S. Schwizer and C. Hagendorf, "Classification of recombination active defect structures in multicrystalline silicon solar cells", *Energy Procedia* **8,** S. 28–34 (2011). doi: https://doi.org/10.1016/j.egypro.2011.06.097
8. D. Lausch, T. Mehl, K. Petter, A. Flø, I. Burud and E. Olsen, "Classification of crystal defects in multicrystalline silicon solar cells and wafer using spectrally and spatially resolved photoluminescence", *J. Appl. Phys.* **119,** 054501 (2016). doi: https://doi.org/10.1063/1.4940711

Paper III

Classification of crystal defects in multicrystalline silicon solar cells and wafer using spectrally and spatially resolved photoluminescence

D. Lausch, T. Mehl, K. Petter, A. Svarstad Flø, I. Burud, and E. Olsen

Citation: Journal of Applied Physics **119**, 054501 (2016); doi: 10.1063/1.4940711
View online: http://dx.doi.org/10.1063/1.4940711
View Table of Contents: http://scitation.aip.org/content/aip/journal/jap/119/5?ver=pdfcov
Published by the AIP Publishing

Articles you may be interested in

Spatially resolved electrical parameters of silicon wafers and solar cells by contactless photoluminescence imaging
Appl. Phys. Lett. **102**, 073502 (2013); 10.1063/1.4792348

Spectral and spatially resolved imaging of photoluminescence in multicrystalline silicon wafers
Appl. Phys. Lett. **99**, 011903 (2011); 10.1063/1.3607307

Experimental setup for camera-based measurements of electrically and optically stimulated luminescence of silicon solar cells and wafers
Rev. Sci. Instrum. **82**, 033706 (2011); 10.1063/1.3541766

Photoluminescence analysis of intragrain defects in multicrystalline silicon wafers for solar cells
J. Appl. Phys. **102**, 054506 (2007); 10.1063/1.2776003

Electronic states of intrinsic layers in n-i-p solar cells near amorphous to microcrystalline silicon transition studied by photoluminescence spectroscopy
Appl. Phys. Lett. **77**, 3185 (2000); 10.1063/1.1325391

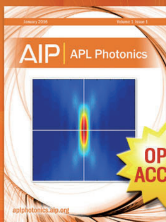

OPEN ACCESS
Launching in 2016!
The future of applied photonics research is here
AIP APL Photonics

Reuse of AIP Publishing content is subject to the terms at: https://publishing.aip.org/authors/rights-and-permissions. IP: 128.39.138.245 On: Fri, 05 Feb 2016 15:37:03

Classification of crystal defects in multicrystalline silicon solar cells and wafer using spectrally and spatially resolved photoluminescence

D. Lausch,[1,a)] T. Mehl,[2] K. Petter,[3] A. Svarstad Flø,[2] I. Burud,[2] and E. Olsen[2]
[1]Fraunhofer-Center für Silizium Photovoltaik CSP, Otto-Eißfeldt-Straße 12, 06120 Halle (Saale), Germany
[2]Norwegian University of Life Sciences NMBU, Universitetstunet 3, 1430 Ås, Norway
[3]Hanwha Q CELLS GmbH, OT Thalheim, Sonnenallee 17–21, 06766 Bitterfeld-Wolfen, Germany

(Received 30 October 2015; accepted 12 January 2016; published online 3 February 2016)

In this contribution, spectral photoluminescence (SPL) imaging detecting both the spectral distribution and the lateral position is applied on recombination active defects in multicrystalline silicon solar cells and wafers. The result is analysed by a Multivariate Curve Resolution (MCR) algorithm using the spectral photoluminescence response and their positions. (i) Without any pre-assumptions made, the algorithm distinguishes four different recombination active defect types. Looking at the spatial distribution, it is shown that two of these defect types coincide with two defect types that have been distinguished on solar cell level using an analysis of forward and reverse biased electroluminescence (denoted as Type-A and -B) previously. (ii) Using SPL, all previously classified defects can also be distinguished at the wafer level. Therefore, the defects limiting the solar cell efficiency are already present in the wafer material and not introduced by the solar cell process. This is of particular interest for the question of how to predict the solar cell efficiency based on the PL measurements at the wafer level. The SPL is able to distinguish between the recombination activity of the dominant Type-A and -B defects that cannot be distinguished by classical PL measurements of the band-to-band recombination at the wafer level. The technique also highlights the changes in recombination activity of the given defects throughout the fabrication process. (iii) Additionally, it is shown that the spectral peak positions of Type-A defects coincide with the known D3 and D4 lines and of Type-B defects with the D1 line on both solar cell and wafer level. Two further defects are captured by the MCR algorithm denoted as Type-VID3 and Type-D07 defects occurring as spot-like defects in isolated positions. Their spectral PL response is analysed as well. *© 2016 AIP Publishing LLC*. [http://dx.doi.org/10.1063/1.4940711]

I. INTRODUCTION

Currently, more than 60% of all solar modules are made from wafer-based multicrystalline silicon (mc-Si) solar cells. However, the efficiency of mc-Si solar cells is ∼10%–15% lower compared to that of the monocrystalline Si solar cells. A major reason for this is the presence of different recombination-active crystal defects in mc-Si materials. These defects have a negative influence on the efficiency[1–3] and electrical breakdown behavior of the cells.[4–6] To overcome these disadvantages, the physical mechanisms taking place at these defect sites must be understood systematically. Single defects in silicon solar cells have been investigated for several years.[7–12] Recently, a systematic investigation for different types of efficiency limiting crystal defects from 6″ solar cells down to the atomic level has been performed based on a classification scheme related to electroluminescence and pre-breakdown behaviour of crystal defects.[13] The recombination active defects were locally distinguished into Type-A and Type-B defects. Type-A defects were correlated to metal (iron) impurities activated by temperature treatment[14] with high impact on the solar cell efficiency.[15] On the contrary, Type-B defects show only a low influence on the efficiency. The root cause of Type-B defects is still unclear. Recombination models for both defect types were proposed.

Photoluminescence (PL) imaging is an established method for characterization of mc-Si wafers by locating recombination active defects at the solar cell[16] and wafer level.[17] Typically, it is performed by integrating all photon energies higher than the smallest energy (longest wavelength) detectable by the camera used. Defected regions are characterized by different luminescence intensities. However, to understand the physical mechanisms occurring at the localized defects the spectral luminescence distributions are needed. For this, a spectral PL imaging technology (SPL) has been developed where both the spectral distribution and lateral information are recorded in a so-called hyperspectral cube containing an image of the sample at each resolved wavelength.[18] In order to analyse the spatial and spectral data, Multivariate Curve Resolution (MCR) was applied in order to extract all the emission signals simultaneously across the wafer, as demonstrated in Ref. 19.

In this work, we apply the spectral imaging method to 6″ mc-Si silicon solar cells and neighbouring wafers. The result is analysed by the MCR method. In Section III A, it is shown that the recombination active defects of the solar cells are distinguished by the MCR algorithm into four different defect types. Two of the types were found to be present at the same positions like type A and B defects as introduced in

[a)]Author to whom correspondence should be addressed. Electronic mail: dominik.lausch@csp.fraunhofer.de

 © 2016 AIP Publishing LLC

Reuse of AIP Publishing content is subject to the terms at: https://publishing.aip.org/authors/rights-and-permissions. IP: 128.39.138.245 On: Fri, 05 Feb 2016 15:37:03

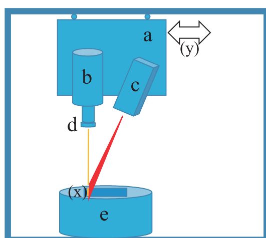

FIG. 1. Schematic illustration of the SPL method. A computer controlled translational stage (a) is used to move the hyperspectral camera (b) relative to the sample (y-direction). The sample is located on an aluminium surface on top of a cryogenic cooler (e). A line laser (c) excite electrons on the line (x-direction) sensed by the camera. A long pass filter (d) is used to stop the exciting signal to enter the camera.

Ref. 13 by forward and reverse biased electroluminescence. The SPL procedure is then applied to a neighbouring as-cut mc-Si wafer in Sec. III B. It is known that the same classified defects are already present in the wafer material, so that type A and B defect regions can already be distinguished on the wafer level. Therefore, the root cause of these defects is the Si bulk material rather than the solar cell process. In Section III C, the spectral response of each defect type is shown. The paper is concluded by a discussion in Section IV. All investigations were performed on standard 6″ solar cell or wafer size. Investigations with high lateral magnification will be focused on an upcoming publication.

II. EXPERIMENTAL DETAILS

Samples: The mc-Si solar cells were fabricated in 2009 with a standard commercial process at the company Q-Cells SE based on Boron-doped (acceptor concentration $N_A \sim 10^{16}\,\mathrm{cm}^{-3}$) 156 mm × 156 mm mc-Si wafers made from standard electronic grade silicon with comparable high purity. The wafers analysed were neighbouring unprocessed wafers of the same type hence exactly out of the same crystal region of the ingot.

Spectral imaging (SPL): SPL images of the samples were obtained using a near-infrared (NIR) hyperspectral camera (SWIR, Specim, Finland). The setup is depicted in Figure 1. A mercury cadmium telluride detector is used with spectral sensitivity in the 929–2531 nm (0.49–1.33 eV) range with a resolution of 6 nm (256 bands). A line image is recorded (320 pixels) giving a spatial resolution of 0.5 mm in both the x and y directions in the setup for this study. 3D images with one spectral and two spatial dimensions were obtained by scanning the imaged line across the samples. As an excitation source, an 808 nm line laser was used with an irradiated power density of $2\,\mathrm{W/cm^2}$ (Lasiris Magnum II). An 850 nm low-pass filter prevented laser beam reflections from entering the optic apparatus. The samples were cooled to 90 K on a polished aluminium surface on top of a cryogenic cooler filled with liquid nitrogen in order to be able to separate single defect lines with high energetic resolution. With increasing temperature, the spectral response of a defect level is energetically broadened resulting in a strong overlap of the different spectral responses. At room temperature, only a broad defect luminescence within the band gap can be detected. Similar setups have been used in previous studies.[19–22]

Data processing: MCR is a mathematical method for deconvolving complex, convoluted signals being composed of several discrete, simultaneously occurring signals. The method involves decomposing the recorded data (signal) matrix D into a matrix containing all the individual signals S^T and a weight matrix C where each signal from S^T is weighted to form the recorded signal in D. Residuals are contained in a separate matrix E. The mathematical representation of the method can be described by the following equation:

$$D = CS^T + E.$$

Initially, the number of components in C and S^T is estimated and put into the model. An iterative process then optimizes the matrixes to best fit D while minimizing the content in E by an Alternating Least Squares (ALS) algorithm.[23]

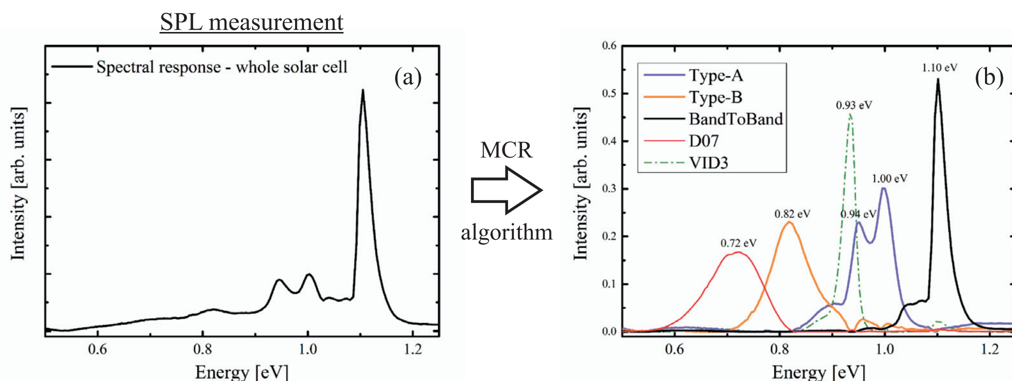

FIG. 2. (a) Spectral response of a solar cell integrated over the whole area measured at 90 K (b) Loading plots from the result of an MCR algorithm applied in the SPL measurement of a mc-Si solar cell.

Reuse of AIP Publishing content is subject to the terms at: https://publishing.aip.org/authors/rights-and-permissions. IP: 128.39.138.245 On: Fri, 05 Feb 2016 15:37:03

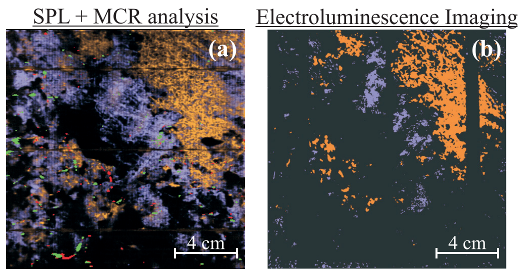

FIG. 3. (a) Lateral distribution of different defect types resolved by MCR algorithm of an SPL measurement (SPL + MCR) on a solar cell. The colours correspond to the defect types distinguished in Fig. 2(b) (Type-A—purple, Type-B—orange, Type-D07—red, Type-VID3—green) (b) Classification by forward and reverse biased electroluminescence introduced in Ref. 13 for comparison on a neighbouring solar cell. Only Type-A and -B defects were distinguished.

III. RESULTS

A. Classification of recombination active defects by MCR analyses of mc-Si solar cells

In Figure 2(a), the spectral response of an mc-Si solar cell integrated over the whole area measured at 90 K by SPL is shown. Below, the indirect band-to-band transition at ∼1.1 eV various defect lines can be detected between 0.55 eV and 1 eV. On the SPL measurement (spectral response connected with the positions), an MCR analysis was applied. An MCR analysis resolves mixtures of different signals by determining the number of constituents, their response profiles, and their estimated concentrations without prior information about their nature and composition automatically. The MCR algorithm results in a separation of five different types shown in Fig. 2(b), which are located at different areas with a different spectral response. These loading plots represent the intensity of each signal in the specific area where it is present. Hence, signals only present in some small spots will make little impact on the whole spectrum in Fig. 2(a), since the graph is an integral of all signals from the sample. The algorithm distinguishes: (i) Regions with a strong band-to-band signal at 1.1 eV (band-to-band—black); (ii) regions with two distinct peaks at 0.94 eV and 1.00 eV (Type-A—purple); (iii) regions with a distinct peak at 0.82 eV (and very weak peaks at 0.94 eV and 1.00 eV—Type-B—orange); (iv) few small spots with 0.72 eV peak (Type-D07—red); and (v) small regions showing very intense spectral response at 0.93 eV (Type-VID3—green) with luminescence intensities almost as strong as from areas with band-to-band luminescence.

In Figure 3(a), the lateral distribution of band-to-band (BB, black), Type-A (purple), Type-B (orange), Type-D07 (red), and Type-VID3 (green) is shown. D07 and VID3 defects are detected at defined, localized positions only. The separated regions (signals BB, A, and B) have a small spatial overlap, hence the different types are located at spatially different areas. Figure 3(b) shows the defect classification introduced in Ref. 14 of a neighbouring solar cell (screen printing was rotated by 90°) in order to compare the defect classification with the SPL + MCR analysis. In Ref. 14, the band-to-band luminescence (>1.1 eV), the defect luminescence (0.73–0.85 eV),[24] and the pre-breakdown luminescence of type-2 pre-breakdown sites[4,6] were used to distinguished Type-A (purple) and Type-B (orange) defects. Although the MCR analysis is automatic and based on mathematical algorithms, the classification performed in Ref. 14 and the MCR analysis are nearly identical. Type-A and Type-B defects were identified as the major defect types in both approaches and at very similar wafer positions. In addition to the much higher lateral resolution of SPL, the reproducibility and accuracy are higher due to the usage of the mathematical

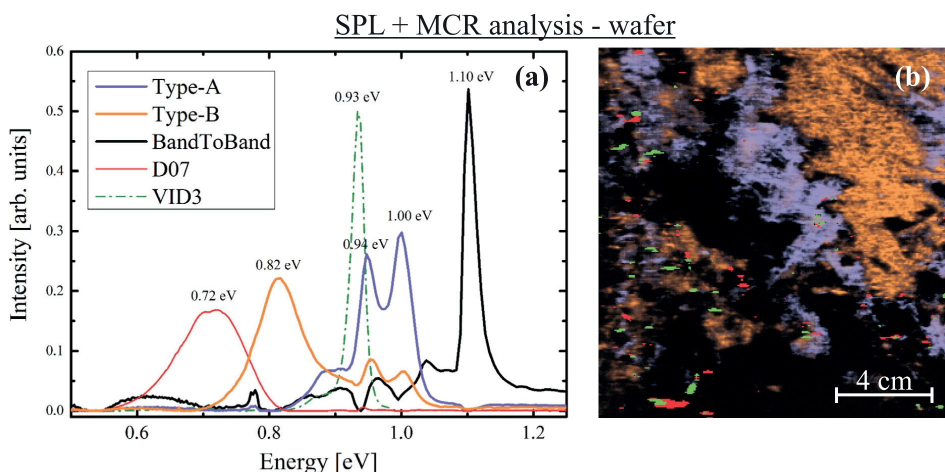

FIG. 4. MCR Analysis of a mc-Si wafer. (a) Spectral response of the defect classes. (b) Lateral position of these defect classes. The same defects were classified on solar cell (Fig. 2) and wafer level. Wafers and solar cells are neighbours.

Reuse of AIP Publishing content is subject to the terms at: https://publishing.aip.org/authors/rights-and-permissions. IP: 128.39.138.245 On: Fri, 05 Feb 2016 15:37:03

procedure compared to the manual classification by using electroluminescence methods. Further, it is obvious that using SPL and MCR analyses more Type-A defects are localized. The reason for this will be discussed later.

B. Different defect types on mc-Si wafer level

The same procedure applied in Sec. III A on solar cell level was applied at the wafer level within this section (SPL + MCR) in order to clarify if the specified defect types are already present at wafer level and how they have evolved during the solar cell process. The MCR analysis classifies the same defect types with equal spectral responses as in the case for solar cells as can be seen in Fig. 4.

By comparing the lateral distribution of Type-A and Type-B defects at the wafer (Fig. 4(b)) and the solar cell level (Fig. 3(a)), it can be stated that both defect types are present within equal regions before and after solar cell processing. A closer look reveals that Type-B defects show the same lateral distribution. In contrast, the area covered by Type-A defects are slightly lower compared to the finished solar cell especially close to the left wafer side, which is an edge region near the crucible wall. Note that the lateral distribution of the Type-A and Type-B defects at the wafer level using SPL (Fig. 4(b)) and on solar cell level using luminescence methods (Fig. 3(b)) is rather similar.

C. Spectral response of different types of recombination active defects

The spectral response of the different defect types can be traced back to well-known D-lines. Regions having a low defect density are characterized by a high intensity of the indirect band-to-band luminescence at 1.1 eV with a shoulder below 1.1 eV and missing defect luminescence (cf. Figs. 3(b) and 4(a)). Type-A defects show strong photoluminescence intensities at 0.94 eV and 1.00 eV. These are usually known as D3 and D4 luminescence peaks, respectively.[25] It is often suggested that the D3 line is most probably a phonon-assisted replica of D4.[26] The fact that the MCR algorithm also treats them as one feature (because their spatial distribution is almost identical) can be considered as another hint that both peaks stem from the same defect. Remarkable is a shoulder contributing to Type-A luminescence with low intensity and a peak at around 0.9 eV sometimes observed in microcrystalline thin-film Si layers and attributed to Si-H bonds.[27] This shoulder is responsible for the low defect luminescence intensity (observed by not spectrally resolved PL in the range of 0.73–0.85 eV) at Type-A defects reported in Ref. 14. Type-B defects are characterized by an intense peak at 0.82 eV often denoted as D1 luminescence and not present in regions with type-A defects. Also, here a shoulder can be seen, around 0.88 eV. This might be D2, often mentioned connected to D1.[28,29] Further, additional defect types having defect luminescence at 0.7 eV (Type-D07) and 0.93 eV (Type-VID3) were observed, but these will be discussed in an upcoming publication.

IV. DISCUSSION

A. Lateral distribution of different defect types on solar cell and wafer level

In Section III A it was shown that SPL combined with an MCR algorithm and the defect classification used in Ref. 13 (band-to-band and sub-band EL combined with reverse breakdown behaviour measured by ReBEL) results in the same defect classification of the major defects Type-A and -B. However, Type-D07 and Type-VID3 are additionally classified by the MCR algorithm and were not detected before. The classification is presented using one prominent example, but was proven with different Si materials having different quality. By comparing the EL and SPL classification, it is obvious that the area covered by Type-A defects seems lower using EL methods (cf. Figs. 4(a) and 4(b)). This is likely caused by the methods used. Using EL methods for classification only the pre-breakdown behaviour of type-2[30] under reverse bias (-11 V) is used to locate Type-A defects on solar cell level. At these positions, metal precipitates are present.[31] Under high magnification, these positions are called Type-A_P defects (which corresponds exactly to the positions where metal precipitates is located) in Ref. 14. Type-A_G defects which are the defects in regions close to Type-A_P defects are likely contaminated by atomic impurities since they become activate after a high temperature treatment. Using now the spectral fingerprint of Type-A defects, SPL is the more reliable method for correct localization. Type-B defects show rather the same lateral distribution using SPL or EL methods.

The analysis of the neighbouring wafer in Section III B reveals that all defect types are already present in the wafer material before solar cell processing. Hence, Type-A, Type-B, Type-D07, and Type-VID3 defects are bulk material defects and not induced during solar cell processing. Hence, the root cause for these defects is found in the Si bulk material. Using SPL, the defects can be distinguished already at wafer level. By comparing the SPL measurement before and after the solar cell process a slight activation of Type-A defects can be seen as reported by Bakowskie *et al.*[32] This observation was already discussed in Ref. 14. Likely, metal precipitates are dissolved during the solar cell process from the metal precipitates present in Type-A regions and segregate to grain boundaries during cool down after the p-n junction formation at 850 °C leading to increased recombination activity. All classified defects are found in regions having a high density of crystal defects. In Ref. 14, it is shown that Type-A and Type-B defects can be traced back to grain boundaries or line shaped dislocations. In a future work, this will be investigated by SPL as well.

B. Recombination processes at different defect types

Type-A defects are characterized by D4 (1.00 eV) defect luminescence with the phonon replica D3 (0.94 eV). Beside various discussions about the root cause, D3 and D4 lines are often attributed to stress induced intra-band defect levels energetic very close to the valence and conduction band.[26] However, the energetic position of these defect levels does

Reuse of AIP Publishing content is subject to the terms at: https://publishing.aip.org/authors/rights-and-permissions. IP: 128.39.138.245 On: Fri, 05 Feb 2016 15:37:03

not explain the strong recombination activity of Type-A defects reported in Ref. 15 but can explain the luminescence at these defects. In Ref. 14, root cause analyses and the recombination strength as a function of the temperature was investigated. These experimental observations are in good agreement with modelling results of Kveder *et al.*[9] explaining the recombination via a large number of deep defect levels. We assume that at Type-A defects, non-radiative recombination is dominant due to metal impurities. Only a small number of the induced charge carriers recombine via band near defects causing the observed luminescence. The grain boundary character of Type-A defects vary from random angle to even small angle grain boundaries.[33] A possible explanation for the high recombination activity at small angle grain boundaries was given recently by Bauer *et al.*[34,35] who have shown that the increased recombination can be traced back to Lomer dislocation likely contaminated with metals.

Type-B defects are characterized by an intense peak at 0.82 eV denoted as the D1 line. Often D1 is attributed to oxygen impurities.[36,37] However, no direct proof has been found so far. The energetic position of the defect level is in agreement to our previous observations explaining the recombination process via a band near defect level causing defect luminescence and the low influence on the solar cell efficiency. Type-B defects are often traced back to small angle grain boundaries.[33] Therefore, at Type-B defects radiative recombination is dominant rather than non-radiative recombination.

Type-D07 and Type-VID3 will be in focus in an upcoming publication. Krause *et al.*[38] assume that the very intense and local Type-VID3 (near the D3 line) is caused by a specific dislocation network formed at slightly misoriented local Σ3 grain boundary parts.

V. SUMMARY

By applying SPL combined with an MCR algorithm on the spectral photoluminescence response of mc-Si solar cells, the recombination active defects are distinguished without any pre-assumptions made into different defect types: (i) Type-A, (ii) Type-B, (iii) Type-VID3, and (iv) Type-D07. Using SPL, these defects can also be distinguished at the wafer level. Hence, it is concluded that the defects are not introduced by the solar cell process and are already present within the Si bulk material. However, the recombination strength can be changed during solar cell processing. Further, typical spectral responses of the distinguished defects are shown. Type-A defects are characterized by D4 (1.00 eV) defect luminescence with the phonon replica D3 (0.94 eV), Type-B by an intense peak at 0.82 eV denoted as the D1 line, Type-D07 by a peak at about 0.7 eV and Type-VID3 by a very intense peak at 0.93 eV. It is concluded that (i) non-radiative recombination are dominant at Type-A defects and (ii) radiative recombination are dominant at Type-B defects.

[1] J. David Zook, "Effects of grain boundaries in polycrystalline solar cells," Appl. Phys. Lett. **37**(2), 223 (1980).
[2] A. A. Istratov and E. R. Weber, "Electrical properties and recombination activity of copper, nickel and cobalt in silicon," Appl. Phys. A: Mater. Sci. Process. **66**(2), 123–136 (1998).
[3] M. Kittler, W. Seifert, and O. Krüger, "Electrical behaviour of crystal defects in silicon solar cells," Solid State Phenom. **78–79**, 39–48 (2001).
[4] W. Kwapil, P. Gundel, M. C. Schubert, F. D. Heinz, W. Warta, E. R. Weber, A. Goetzberger, and G. Martinez-Criado, "Observation of metal precipitates at prebreakdown sites in multicrystalline silicon solar cells," Appl. Phys. Lett. **95**(23), 232113 (2009).
[5] O. Breitenstein, J. Bauer, K. Bothe, W. Kwapil, D. Lausch, U. Rau, J. Schmidt, M. Schneemann, M. C. Schubert, J.-M. Wagner, and W. Warta, "Understanding junction breakdown in multicrystalline solar cells," J. Appl. Phys. **109**(7), 71101 (2011).
[6] D. Lausch, K. Petter, H. Von Wenckstern, and M. Grundmann, "Correlation of pre-breakdown sites and bulk defects in multicrystalline silicon solar cells," Physica Status Solidi RRL **3**(2–3), 70–72 (2009).
[7] S. Steingrube, O. Breitenstein, K. Ramspeck, S. Glunz, A. Schenk, and P. P. Altermatt, "Explanation of commonly observed shunt currents in c-Si solar cells by means of recombination statistics beyond the Shockley-Read-Hall approximation," J. Appl. Phys. **110**(1), 14515 (2011).
[8] H. C. Card and E. S. Yang, "Electronic processes at grain boundaries in polycrystalline semiconductors under optical illumination," IEEE Trans. Electron Devices **24**(4), 397–402 (1977).
[9] V. Kveder, M. Kittler, and W. Schröter, "Recombination activity of contaminated dislocations in silicon: A model describing electron-beam-induced current contrast behavior," Phys. Rev. B **63**, 115208 (2001).
[10] J. P. Hirth, "The influence of grain boundaries on mechanical properties," Metall. Trans. **3**(12), 3047–3067 (1972).
[11] C. H. Seager, "Grain boundary recombination: Theory and experiment in silicon," J. Appl. Phys. **52**(6), 3960 (1981).
[12] R. Bakowskie, G. Kesser, R. Richter, D. Lausch, A. Eidner, P. Clemens, and K. Petter, "Fast method to determine the structural defect density of 156 × 156 mm^2 Mc-Si wafers," Energy Proc. **27**, 179–184 (2012).
[13] D. Lausch, K. Petter, B. Henke, R. Bakowskie, S. Schweizer, and C. Hagendorf, "Classification of recombination active defect structures in multicrystalline silicon solar cells," Energy Proc. **8**, 28–34 (2011).
[14] D. Lausch, K. Petter, R. Bakowskie, J. Bauer, O. Breitenstein, and C. Hagendorf, "Classification and investigation of recombination-active defect structures in multicrystalline silicon solar cells—recombination models," in *Proceedings of the 27th EUPVSEC*, Frankfurt (Main), Germany (2012), pp. 723–728, see URL https://www.eupvsec-proceedings.com/proceedings/checkout.html?paper=17019.
[15] D. Lausch and C. Hagendorf, "Influence of different types of recombination active defects on the integral electrical properties of multicrystalline silicon solar cells," J. Solar Energy **2015**(4), 1–9.
[16] T. Fuyuki, H. Kondo, T. Yamazaki, Y. Takahashi, and Y. Uraoka, "Photographic surveying of minority carrier diffusion length in polycrystalline silicon solar cells by electroluminescence," Appl. Phys. Lett. **86**(26), 262108 (2005).
[17] T. Trupke, R. A. Bardos, M. C. Schubert, and W. Warta, "Photoluminescence imaging of silicon wafers," Appl. Phys. Lett. **89**(4), 44107 (2006).
[18] E. Olsen and A. S. Flø, "Spectral and spatially resolved imaging of photoluminescence in multicrystalline silicon wafers," Appl. Phys. Lett. **99**(1), 11903 (2011).
[19] A. Flø, I. Burud, K. Kvaal, R. Søndenå, and E. Olsen, "Distribution of radiative crystal imperfections through a silicon ingot," AIP Adv. **3**(11), 112120 (2013).
[20] I. Burud, A. S. Flø, and E. Olsen, "On the origin of inter band gap radiative emission in crystalline silicon," AIP Adv. **2**(4), 42135 (2012).
[21] A. Flø, I. Burud, and E. Olsen, "Spatially and spectrally resolved temperature dependence of defect related luminescence using hyperspectral imaging," in *Proceedings of the Photovoltaic Specialist Conference (PVSC)* (2014), pp. 1888–1892.
[22] J. Bauer, D. Lausch, H. Blumtritt, N. Zakharov, and O. Breitenstein, "Avalanche breakdown in multicrystalline solar cells due to preferred phosphorous diffusion at extended defects," Prog. Photovoltaics Res. Appl. **21**(7), 1444–1453 (2013).
[23] S. Piqueras, L. Duponchel, R. Tauler, and A. de Juan, "Resolution and segmentation of hyperspectral biomedical images by multivariate curve resolution-alternating least squares," Anal. Chim. Acta **705**(1–2), 182–192 (2011).

Reuse of AIP Publishing content is subject to the terms at: https://publishing.aip.org/authors/rights-and-permissions. IP: 128.39.138.245 On: Fri, 05 Feb 2016 15:37:03

[24]F. Lausch and C. Hagendorf, "Microscopic Study of Defect Luminescence between 0.72–0.85 eV by optical microscopy," Microsc. Res. **02**(01), 9–12 (2014).
[25]N. A. Drozdov, A. A. Patrin, and V. D. Tkachev, "Recombination radiation on dislocations in silicon," JETP Lett. **23**(11), 597 (1976).
[26]V. V. Kveder, E. A. Steinman, S. A. Shevchenko, and H. G. Grimmeiss, "Dislocation-related electroluminescence at room temperature in plastically deformed silicon," Phys. Rev. B **51**(16), 10520–10526 (1995).
[27]A. U. Savchouk, S. Ostapenko, G. Nowak, J. Lagowski, and L. Jastrzebski, "Band-tail photoluminescence in polycrystalline silicon thin films," Appl. Phys. Lett. **67**(1), 82 (1995).
[28]R. Sauer, J. Weber, J. Stolz, E. R. Weber, K.-H. Küsters, and H. Alexander, "Dislocation-related photoluminescence in silicon," Appl. Phys. A **36**(1), 1–13 (1985).
[29]E. C. Lightowlers and V. Higgs, "Luminescence associated with the presence of dislocations in silicon," Phys. Status Solidi A **138**(2), 665–672 (1993).
[30]J.-M. Wagner, J. Bauer, and O. Breitenstein, "Classification of pre-breakdown phenomena in multicrystalline silicon solar cells, Bd. 24," in *Proceedings of the 24th EU-PVSEC*, Munich, Germany (2009), pp. 925–929.
[31]A. Hähnel, J. Bauer, H. Blumtritt, O. Breitenstein, D. Lausch, and W. Kwapil, "Electron microscope verification of prebreakdown-inducing α-FeSi2 needles in multicrystalline silicon solar cells," J. Appl. Phys. **113**(4), 44505 (2013).
[32]R. Bakowskie, R. Lantzsch, T. Kaden, K. Eller, D. Lausch, Y. Ludwig, and K. Petter, "Comparison of recombination active defects in multicrystalline silicon by means of photoluminescence imaging and reverse biased electroluminescence," in *Proceedings of the 26th European Photovoltaic Solar Energy Conference and Exhibition* (2010), pp. 1839–1842.
[33]D. Lausch, M. Gläser, and C. Hagendorf, "Determination of crystal grain orientations by optical microscopy at textured surfaces," J. Appl. Phys. **114**(19), 194509 (2013).
[34]J. Bauer, A. Hähnel, H. Blumtritt, H. Deniz, A. Zuschlag, and O. Breitenstein, "Do Lomer dislocations spoil high performance of mc-Si solar cells?," Energy Proc. **77**, 565–571 (2015).
[35]J. Bauer, A. Hahnel, P. Werner, N. Zakharov, H. Blumtritt, A. Zuschlag, and O. Breitenstein, "Recombination at Lomer dislocations in multicrystalline silicon for solar cells," IEEE J. Photovoltaics **6**(1), 100–110 (2016).
[36]S. Pizzini, M. Acciarri, E. Leoni, and A. Le Donne, "About the D1 and D2 dislocation luminescence and its correlation with oxygen segregation," Phys. Status Solidi B **222**(11), 141–150 (2000).
[37]K. Bothe, R. J. Falster, and J. D. Murphy, "Room temperature subbandgap photoluminescence from silicon containing oxide precipitates," Appl. Phys. Lett. **101**(3), 32107 (2012).
[38]C. Krause, D. Mankovics, H.-M. Krause, T. Arguirov, and M. Kittler, "On the origin of intense luminescence at 0.93 eV from multi-crystalline silicon," J. Appl. Phys. **114**(3), 34902 (2013).

Reuse of AIP Publishing content is subject to the terms at: https://publishing.aip.org/authors/rights-and-permissions. IP: 128.39.138.245 On: Fri, 05 Feb 2016 15:37:03

Paper IV

Available online at www.sciencedirect.com

ScienceDirect

Energy Procedia 92 (2016) 130 – 137

Energy Procedia

6th International Conference on Silicon Photovoltaics, SiliconPV 2016

Defects in multicrystalline Si wafers studied by spectral photoluminescence imaging, combined with EBSD and dislocation mapping

Torbjørn Mehl[a,]*, Marisa Di Sabatino[b], Krzysztof Adamczyk[b], Ingunn Burud[a] and Espen Olsen[a]

[a]Norwegian University of Life Sciences, NMBU, Universitetstunet 3, 1430 Ås, Norway
[b]Norwegian University of Science and Technology, NTNU, Alfred Getz vei 2B, 7491 Trondheim, Norway

Abstract

Defect related sub-band gap luminescence emissions due to Shockley-Read-Hall recombination in mc-Si wafers have been investigated with spectral photoluminescence imaging, combined with electron backscatter diffraction and dislocation mapping, for p- and n-type wafers, with and without intentionally introduced Fe. The well-known emission with energy 0.807 eV (D1) is found to be correlated with heavily dislocated areas of the wafers with emissions emanating from the immediate vicinity of the defects. A less studied emission with energy centered around 0.7 eV (D07) may be the product of two emissions and is found to exhibit very different characteristics in a boron-doped wafer intentionally contaminated with Fe than in the other samples. There is reason to believe that a radiative recombination pathway with characteristic photons with energy 0.694 eV is present in this sample due to interstitial iron, Fe_i, while the D3/D4 (0.938 eV/1.00 eV) emission pair is related to the FeB complex.

© 2016 The Authors. Published by Elsevier Ltd. This is an open access article under the CC BY-NC-ND license (http://creativecommons.org/licenses/by-nc-nd/4.0/).
Peer review by the scientific conference committee of SiliconPV 2016 under responsibility of PSE AG.

Keywords: Silicon; Defects; Solar cells; Photoluminescence; Iron.

* Corresponding author. Tel.: +47-67231645.
E-mail address: torbjorn.mehl@nmbu.no

1876-6102 © 2016 The Authors. Published by Elsevier Ltd. This is an open access article under the CC BY-NC-ND license (http://creativecommons.org/licenses/by-nc-nd/4.0/).
Peer review by the scientific conference committee of SiliconPV 2016 under responsibility of PSE AG.
doi:10.1016/j.egypro.2016.07.043

1. Introduction

Material defects in silicon wafers for PV applications lead to a significant reduction of the efficiency of the final solar cells due to a decrease of the carrier lifetime. Spectral photoluminescence imaging (SPL) is a technology that can reveal new knowledge on the shape and structure of radiative recombination active centers originating from crystal imperfections in the silicon wafers [1]. It is a non-destructive and non-contact method used on full size wafers and solar cells.

The SPL method combines two established methods for recording photoluminescence (PL) from silicon wafers and solar cells, PL imaging [2] and PL spectroscopy [3]. PL imaging gives the spatial distribution of defect related luminescence (DRL) integrated over the spectral range, and selected spectral regions can be obtained by mounting different filters prior to the recording. PL spectroscopy, on the other hand, gives the whole DRL spectrum, but has no spatial resolution. Therefore, selection of location is essential and required prior to scan. SPL overcomes these limits and extracts the advantages of both methods. For each spatial pixel in the image, the full PL spectrum is stored. From the stored image, it is possible to select a variety of energy levels or specific regions for more detailed studies.

In order to obtain information on origin and nature of the selected regions from the spectral imaging measurements, it is necessary to correlate the images with other complementary material characterization techniques. In this work, spectral imaging has been combined with electron backscatter diffraction (EBSD) and dislocation mapping to study correlations between radiative recombination active centers, dislocation density and crystal orientation.

Multivariate curve resolution (MCR) has been utilized in this study. It is a method in multivariate statistics that decomposes the measured data matrix D into a number of representative score matrices S^T (images in our case) with corresponding loading vectors C that represent the weight of each variable (energy) used to obtain the score image. In the present application, the loading vector can be looked upon as a deconvolution of the numerous complex signals in the data set. The score images yield the spatial distribution of each of the emissions seen in the loadings. An error matrix E represents the difference between the recorded and the simulated signal, and is minimized using an alternating least squares (ALS) algorithm [4]. MCR can be represented mathematically by Eq. (1)

$$D = CS^T + E \tag{1}$$

2. Material and method

The samples investigated were multicrystalline silicon wafers made in a pilot scale, cylindrical furnace (12 kg charge). The dimensions were originally 125x125 mm^2 with thickness of approximately 200 µm. Three samples were investigated in this study: sample A: p-type, boron-doped; sample B: p-type boron-doped with Fe added to the charge; and sample C: n-type phosphorous doped with Fe added.

First, the samples were analyzed using spectral photoluminescence. The SPL setup comprised a hyperspectral camera (sensitivity range 900 - 2500 nm), an excitation source (808 nm, $2W/cm^2$ laser) and a liquid N_2-based cryogenic sample holder (77K - RT). In this study, the spatial resolution was 100 µm and the temperature set to 90K.

The samples were then polished down to 1 µm and analyzed by JEOL JSM 840 SEM equipped with NORDIF EBSD detector for mapping of grain orientation and grain boundary types. The samples were etched with Sopori etchant and the dislocation density measured by an automated dislocation scanning system (PVScan by GT Solar).

To study the impact of etching on the PL properties, SPL scans were again performed. The spectra were processed by MCR using the software package MatLab equipped with the MIA_Toolbox and PLS_Toolbox extension.

3. Results and discussion

The total PL spectrum from sample A, p-type wafer, is shown in Figure 1. The peaks on the graph correspond with the defect luminescence bands D1 – D4 [5], D07 [6] and band-to-band recombination PL signal (BB-PL). An image of the integral of all DRL signals in the interval 0.5 – 1.0 eV, equal to what one would get from established PL imaging, is shown in Figure 1 top right. From such an image, it is almost impossible to distinguish between different types of defects. To illustrate the possibilities of the SPL method, images of the defect related emissions D07 (0.694 eV), D1 (0.807 eV) and D4 (1.00 eV) are shown in Figure 1 bottom right, respectively. Their spatial distribution is clearly not correlated.

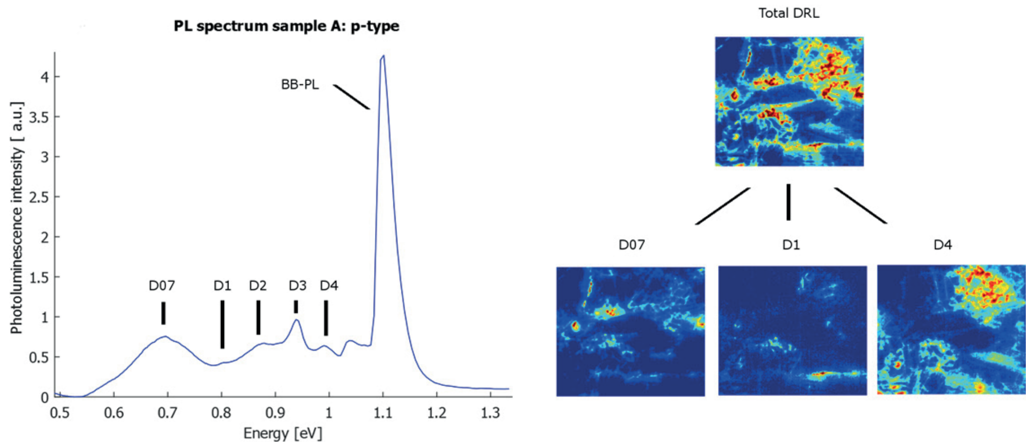

Fig. 1. Left: Accumulated luminescence emission spectrum from p-type boron-doped mc-Si wafer. Top right: PL image of all defect related luminescence in the interval 0.5 eV to 1.0 eV. Bottom: PL images of some selected defect signals; D07 (0.694 eV, left), D1 (0.807 eV, middle) and D4 (1.00 eV, right).

3.1. Spectral and spatial distribution of D07 signal

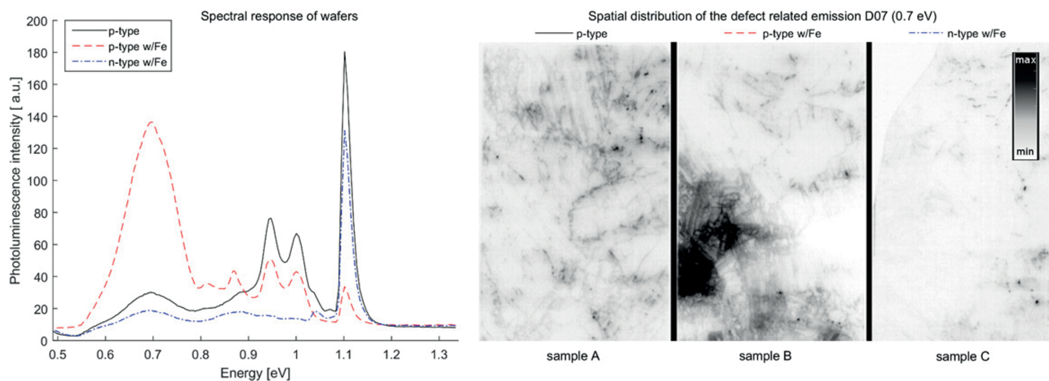

Fig. 2. Left panel: Accumulated luminescence emission spectrum from the three types of wafers, measured at 90K. Right panel: Spatial distribution of the defect related emission D07 (0.7 eV) in the three different wafers. Left image: Sample A, p-type with no added Fe; Middle image: Sample B, p-type with added Fe; Right image: Sample C, n-type with added Fe. The images are inverted in order to better visualise the emission signals (shown in black).

The total spectra from all the samples investigated and the distribution of the D07 signal are shown in Figure 2. All spatial distribution images are an integral over the interval from the spectral response center peak ± 0.05 eV. It is evident from Figure 2 that the D07 signal is found in all the samples. The n-type sample shows a notable lower signal strength, though. The boron-doped sample with Fe intentionally added exhibits significantly higher signal. This may indicate that the D07 emission is associated with Fe. The D07 signal is notably different in the two p-type samples. In sample A and C, the signal occurs as spot-like features or, seemingly, along grain boundaries. In sample B, however, the signal appears as distributed within the grains as well as along the boundaries and in spots.

In Figure 3, a spectrum from a bright, distributed D07 intra-grain area in sample B is compared with a spectrum from a bright spot. The two D07 signals have both different spatial distribution and also slightly different spectral behaviors, indicating that the two signals have different origins. In the extended areas, the center peak energy is at 0.694 eV with a marked peak energy. This signal with distributed occurrence appears strong in the intra-grain areas of the p-type wafer intentionally contaminated with Fe. In other areas, it is weak or not present. The signal emanating from the spots has a slightly higher center energy of 0.716 eV, found in all samples. This signal appears blunt on top.

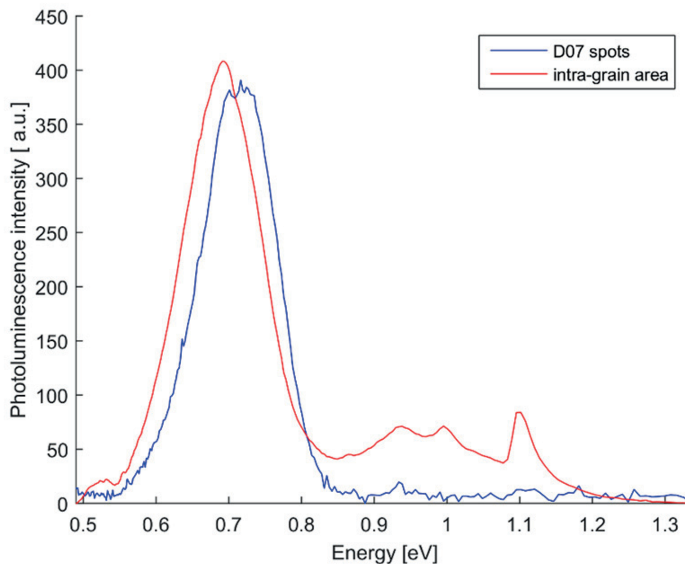

Fig. 3. Spectra from distributed D07 intra-grain area (red) signal versus D07 spot (blue) in sample B, p-type with Fe added. The intra-grain signal shows correlation with the D3/D4 and BB-PL signals while this is absent in the spot-like emission.

3.2. Dislocations

In order to find correlations between different DRL signals, crystal structure and dislocations, the PL images were visually compared with EBSD and PVScan, respectively, see Figure 4. The distribution of the emission signal D07 (0.694 eV) was compared for the three samples. For all three wafers (only sample B shown here), D07 correlate with grain boundaries, especially Σ9, Σ27 and random GB.

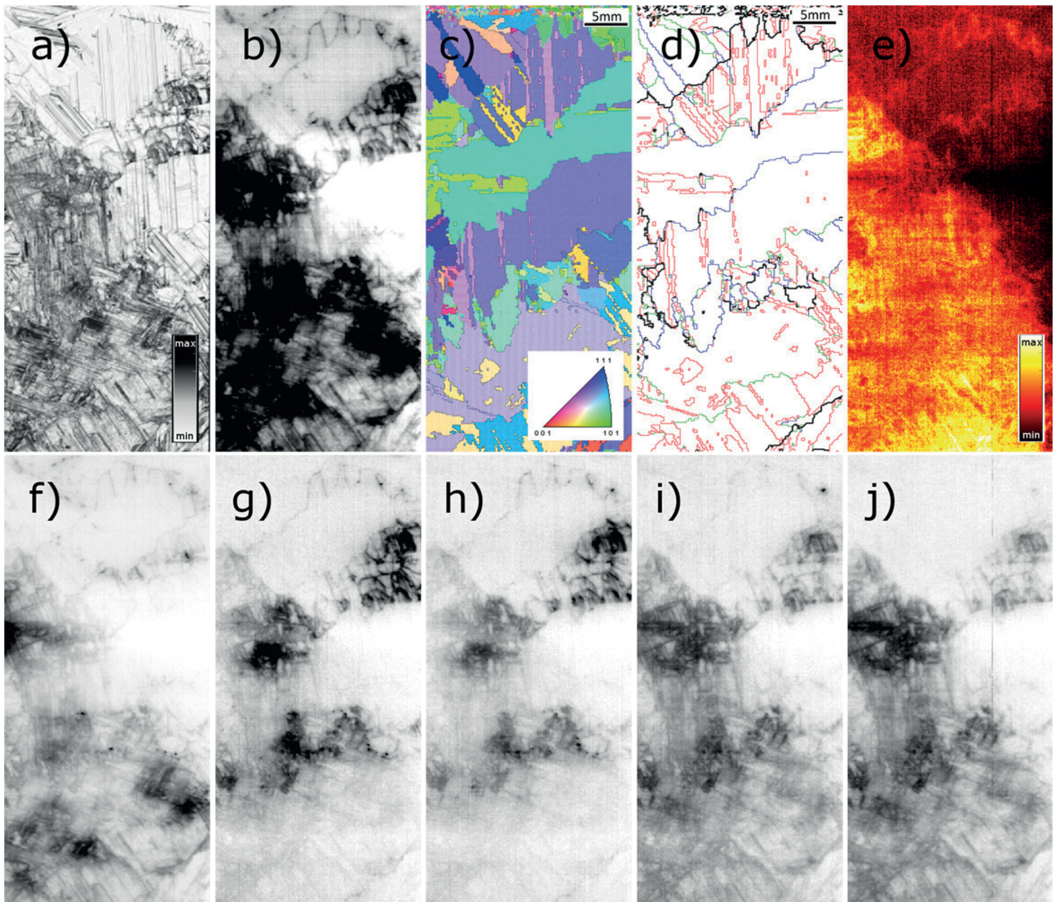

Fig. 4. Spatial distribution of features in sample B; p-type boron-doped mc-Si wafer with addition of Fe. (a) Dislocation mapping, (b) DRL image (integral of signal (0.5 – 1.0 eV), (c) grain orientation, (d) grain boundary types. Coincident site lattice (CSL) grain boundary type Σ3 in red, Σ9 in green, Σ27 in blue and random GB in black. (e) BB PL (1.10 eV). (f) Spatial distribution of D07 (0.694 eV), (g) D1 (0.807 eV), (h) D2 (0.875 eV), (i) D3 (0.938 eV) and (j) D4 (1.00 eV).

For the p-type wafer enriched with Fe there is an additional signature of the spatial distribution of the emission signal. There seems to be a strong D07 emission in regions with high dislocation density for this sample (Figure 4 (f) vs (a)). Since the wafer is enriched with Fe, this could possibly be due to Fe-B pairs or interstitial iron (Fe_i).

When comparing images of the radiative photoluminescence signals D1 (0.807 eV) and D2 (0.875 eV) with dislocation maps, the spatial distribution of D1 and D2 correlates and the regions with D1 and D2 emissions have high dislocation density, as shown for a selected part of the p-type wafer enriched with Fe. The D1 and D2 signals also seem to be correlated with the crystal directions. Grain boundaries show no correlation with D1 and D2. In Figure 4, it seems to be a correlation with random GB, but the signal have slightly different energy, see section 3.3 below.

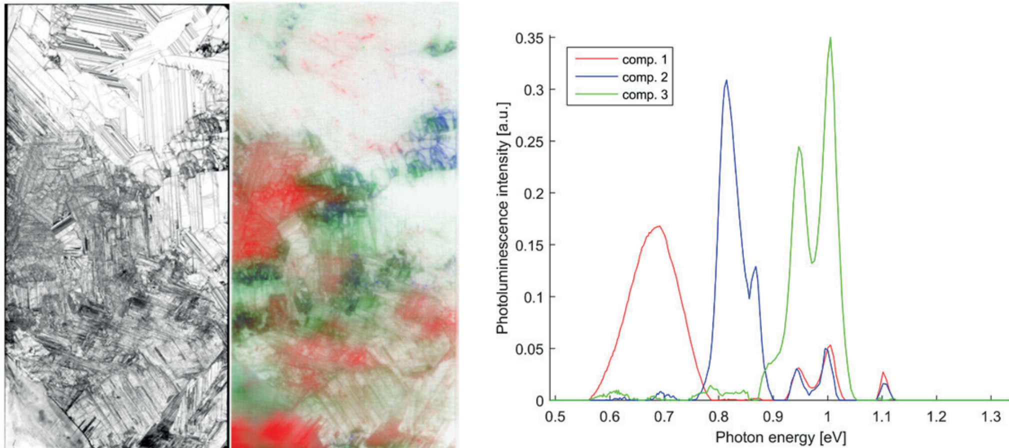

Fig. 5. Dislocation density of sample B beside image and graph of three components from an MCR analysis. It is correlation between high dislocation density and spatial distribution of the components. Comp. 1 (red) correspond to D07 with weak signals of D3 and D4. Comp. 2 (blue); D1 and D2 with weak D3 D4. Comp. 3 (green): D3 D4.

The spatial distribution of D3 and D4 signals seems to correlate and the two signals emits from areas with high dislocation density. The dislocation density patterns of D1/D2 and D3/D4 looks different. Future studies will have to be done to distinguish these dislocation density patterns. It also seems that D1/D2 have a higher negative impact on the band-to-band luminescence than D3/D4, cf. [7]. The D3/D4 signals also seem to be present, but weak, in areas with D1/D2. To separate the different signals and group them spectrally and spatially, an MCR analysis is conducted on the hyperspectral image.

The result from an MCR analysis is depicted in Figure 5. It groups the DRL into three components. Component 1, red in Figure 5, exhibit a spectrum with center peak energy 0.69 eV but also to relatively weak peaks at 0.94 eV (correspond to D3) and 1.00 eV (D4). This indicate that the 0.694 eV and D3/D4 are of FeB / Fe_i origin. The different states give rise to the different signals. Graff [8] states that FeB leads to a shallow level in the band gap of Si at E_V +0.1 eV. This is in accordance with the D4 signal at 1.00 eV emanating from carrier recombination from E_C to E_T. It is widely reported that the D3/D4 signal is a primary mechanism with its associated replica. If this is the case, recombination through this level may give raise to both these signals. Interstitial Fe_i is, on the other hand, reported to introduce a level at E_V +0.39 eV. This is in accordance with at least one of the D07-related signals (Fig. 3) to be associated with Fe_i. This will be investigated further in an upcoming paper.

The state of the binding in Fe-containing complexes in the Si structure has been subject to much debate. Within one of the proposed models, covalent bonding between Fe and the Si atoms nearest to the substitutional B plays a significant role and suggestions are made that there are no direct covalent bond between the Fe and the B [9]. We may speculate that if this is the case, the actual substitutionally placed element may not be crucial in the Fe-containing complex. The same mechanisms may therefore come to play for other elements than B with similar bonding characteristics in the Si lattice. This may explain the occurrence of a D3/D4-like emission pair in Fe-doped n-type Si. This calls for further fundamental studies.

Component 2, blue in Figure 5, has center peaks energy levels corresponding to D1 and D2 with weak D3 and D4. Component 3, green in Figure 5, has center peaks corresponding to D3 and D4. The two MCR-components spectra correspond to previous studies [10,11], where the recombination active defects were grouped in two types; Here, component 2 corresponds to Type B and component 3 to Type A, a denomination introduced by Lausch et al. [11]. Type A defects have been correlated with iron impurities [11].

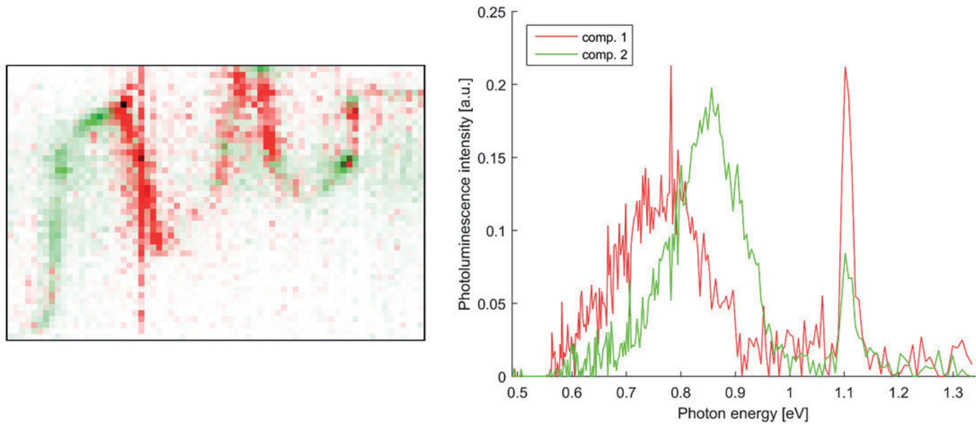

Fig. 6. MCR analysis of area with random GB, obtained from the top part of sample B, as depicted in Figure 4. DRL with center peak energy levels of 0.78 and 0.85 eV and BB PL-signal.

3.3. Red zone

In red zones and other areas with high metallic impurities of multicrystalline silicon ingots, higher Band-to-Band PL-signals have been observed in grain boundaries and dislocation clusters [12]. The internal gettering processes during solidification, will diffuse iron near primary grain boundaries into the boundary regions and effectively locking them there [13]. The depleted region near the grain boundaries will have higher lifetime and thereby higher BB PL-signal than the surroundings. The strongest internal gettering effect has been observed at Random GB [13]. In the p-doped sample w/Fe in Figure 4, we observe a weak BB PL-signal at Random GB, and also DRL of different energy levels. Due to spatial resolution of 100µm, it is not possible to perceive if the BB PL-signal emit from the grain boundary or from adjacent areas. MCR analysis is done on an area obtained from the top part of sample B. The algorithm divide the DRL into two different components, with center peak energies of 0.78eV and 0.85eV respectively. BB is present in both. Figure 6 shows their spatial distribution and radiative spectrum.

4. Conclusion

In this study, we have used spectral photoluminescence imaging to determine spectral- and spatial distribution of radiative active defects in multicrystalline silicon wafers. Combined with EBSD and dislocation mapping, we have found correlations between different DRL signals, and between DRL and dislocation density. There is a spatial correlation between D1 and D2, and between D3 and D4, respectively. Moreover, D1/D2 and D3/D4 appear in different distinct dislocation areas. By applying MCR analysis, the D1/D2 and D3/D4 have been linked to previously studied Type A and Type B defects, respectively.

The DRL signal around 0.7 eV (D07) may be the product of two emissions, one centered at 0.694 eV and the other at 0.716 eV. The D07 is found to exhibit very different characteristics in a boron-doped wafer intentionally contaminated with Fe than in the other samples. There is reason to believe that a radiative recombination pathway with characteristic photons with energy 0.694 eV is present in this sample due to interstitial iron Fe_i, while the D3/D4 emission pair is related to the FeB complex.

References

[1] Olsen E, Flø AS. Spectral and spatially resolved imaging of photoluminescence in multicrystalline silicon wafers. Appl Phys Lett 2011;99:1.
[2] Trupke T, Bardos RA, Schubert MC, Warta W. Photoluminescence imaging of silicon wafers. Appl Phys Lett 2006;89:044107.
[3] Mudryi AV, Korshunov FP, Patuk AI, Shakin IA, Larionova TP, Ulyashin AG et al. Low-temperature photoluminescence characterization of defects formation in hydrogen and helium implanted silicon at post-implantation annealing. Physica B 2001;308-310:181-4.
[4] Piqueras S, Duponchel L, Tauler R, Juan A. Resolution and segmentation of hyperspectral biomedical images by Multivariate Curve Resolution - Alternating Least Squares. Analytica Chimica Acta 2011;705:1-2:182-192
[5] Drozdov NA, Partin AA, Tkachev VD. Recombination radiation on dislocations in silicon. Sov Phys JETP Lett. 1976;23:597-9.
[6] Flø A, Burud I, Kvaal K, Søndenå R, Olsen E. Distribution of radiative crystal imperfections through a silicon ingot. AIP Advances 2013;3:112120.
[7] Lausch D, Hagendorf C. Influence of different types of recombination active defects on the integral electrical properties of multicrystalline silicon solar cells. J Solar Energy 2015;4:1-9.
[8] Graff K. Metal Impurities in Silicon-Device Fabrication. Springer-Verlag Berlin Heidelberg 2000;ISBN 3-540-64213-7.
[9] Istratov AA, Hieselmair H, Weber ER. Iron and its complexes in silicon. Appl Phys A 1999;69;13-44.
[10] Lausch D, Mehl T, Petter K, Flø AS, Burud I, Olsen E. Classification of crystal defects in multicrystalline silicon solar cells and wafer using spectrally and spatially resolved photoluminescence. J Appl Phys 2016;119:054501.
[11] Lausch D, Petter K, Bakowskie R, Bauer J, Breitenstein O, Hagendorf C. Classification and investigation of recombination-active defect structures in multicrystalline silicon solar cells-recombination models. Proceedings of the 27th EUPVSEC 2012:723-8.
[12] Boulfrad Y, Haarahiltunen A, Savin H, Øverlid EJ, Arnberg L. Enhanced performance in the deteriorated area of mc Si wafers by internal gettering. IEEE J Photovolt 2012;2:479-484.
[13] Knörlien M, Autruffe A, Søndenå R, Di Sabatino M. Internal gettering of iron at extended defects. Energy Procedia 2014;55:539-544.

Paper V

Available online at www.sciencedirect.com

ScienceDirect

Energy Procedia 124 (2017) 107–112

Energy Procedia

www.elsevier.com/locate/procedia

7th International Conference on Silicon Photovoltaics, SiliconPV 2017

Oxygen-related defects in n-type Czochralski silicon wafers studied by hyperspectral photoluminescence imaging

Torbjørn Mehl[a,*], Ingunn Burud[a], Elénore Letty[b] and Espen Olsen[a]

[a]*Norwegian University of Life Sciences, NMBU, Universitetstunet 3, 1433 Ås, Norway*
[b]*CEA, LITEN, INES-Department of solar technologies, F-73375 Le Bourget du Lac, France*

Abstract

Oxygen-related Thermal Donors in n-type Czochralski silicon (Cz-Si) wafers have been investigated using hyperspectral photoluminescence imaging and OxyMap. Thermal Donors give rise to two photoluminescence emissions, one narrow peak at 0.767 eV, and one broad band with centre peak at 0.72 eV that is also measurable at room temperature. The spectral imaging was first carried out on the sample cooled to 90 K, then repeated at room temperature (300 K). The possibility to delimitate at room temperature defects-rich zones with hyperspectral photoluminescence imaging is evidenced.

© 2017 The Authors. Published by Elsevier Ltd.
Peer review by the scientific conference committee of SiliconPV 2017 under responsibility of PSE AG.

Keywords: hyperspectral imaging; photoluminescence; thermal donor; oxygen; Czochralski silicon

1. Introduction

Oxygen is a major impurity in Czochralski (Cz) Si. It comes from the dissolution of the quartz crucible during crystallization and is incorporated in large amount in the ingot. Interstitial oxygen (O_i) has not been shown to be recombination active so far, but it gives birth to multiple defects. This is for example the case of oxide precipitates formed at high temperature and responsible for efficiency losses of more than 4 % absolute [1]. This is also the case of Thermal Donors (TD) which are electrically active clusters of Si and O_i formed at temperatures in the range 350–550°C. TD are known to be recombination-active and to introduce multiple energy levels into the gap [2].

* Corresponding author. Tel.: +47-98446844.
E-mail address: torbjorn.mehl@nmbu.no

1876-6102 © 2017 The Authors. Published by Elsevier Ltd.
Peer review by the scientific conference committee of SiliconPV 2017 under responsibility of PSE AG.
10.1016/j.egypro.2017.09.326

The existence of intermediate energy levels in the gap may enable recombination pathways for photo exited charge carriers. This pathways can be radiative or non-radiative. In general freeze out of phonons in indirect bandgap semiconductor like Silicon will cause more and more processes to be of radiative nature, due to energy conservation as the sample temperature is lowered towards cryogenic temperature.

Several lines in the photoluminescence (PL) spectra have been observed and linked to oxygen-related defects such as TD. Especially the P and H lines have been reported by many [3-6] to be connected to TD. The photon energy of the zero-phonon line of P is 0.767 eV and for H 0.926 eV. The P line is observed in samples with oxygen concentration above 3–5x10^{17} cm^{-3} [7] regardless if it is n- or p-type doped silicon [3]. Tajima [8] reports a broad PL emission band with center energy 0.7 eV accompanying the P line. While the 0.7 eV band is observable at room temperature, the P line is visible only below 150 K. The H line has been associated with a TD defect complex involving both oxygen and carbon [6].

Hyperspectral PL imaging has been used in previous studies to characterize multicrystalline silicon wafers and solar cells [9-13], but the technique have never before been used on Cz-Si wafers.

In this study, the aim was to determine the potential of hyperspectral PL imaging to detect heterogeneous distribution of defects/impurities in Cz wafers. Areas full of O_i related defects will be particularly studied not only at low temperatures but also at room temperature.

2. Materials and method

The sample characterized in this study is a wafer from an n-type, phosphorus doped, Czochralski ingot. The 156 mm x 156 mm wafer is from the top part (seed-end) of an industrial ingot, solidified fraction < 5%. This part contains the highest [O_i] and is submitted to a rather slow cooling. It should thus contain high densities O_i-related defects. The as-cut resistivity is stated to vary from 1.5 Ωcm at the wafer center to 5 Ω.cm at the edge related to a high variation of [TD] across the wafer diagonal. The wafer was chemically textured (KOH) in order to remove the saw damaged layer. We are therefore confident that the PL imaging presented in these study are representative of the bulk of the wafer

The [O_i] was determined by OxyMap on a sister wafer. This characterization tool aims at measuring [O_i], [P] and as-grown [TD] across the wafers. It is based on resistivity measurements on as-received wafers, after controlled generation of TD and after suppression of TD. Details about the technique can be found in [14].

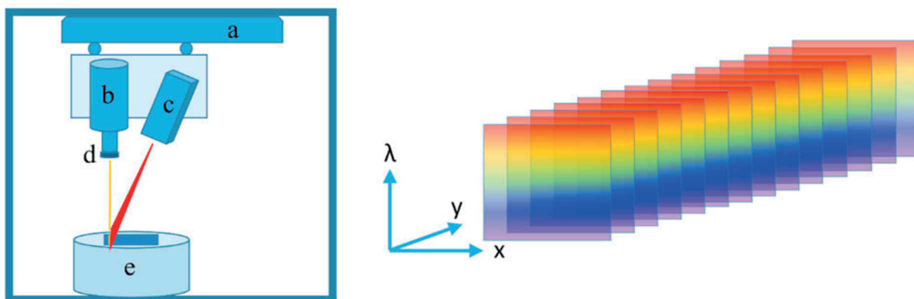

Fig. 1. Hyperspectral imaging setup. a) translation stage, b) hyperspectral camera, c) line laser, d) low pass filter and e) cryogenic cooler. The camera records a 2D image with one spatial and one spectral dimension. The second spatial dimension is obtained by assembling images taken while the camera scans the sample using the translation stage.

In this study a hyperspectral photoluminescence imaging setup, shown in Fig. 1, have been used. The near-infrared (NIR) push-broom hyperspectral camera, with a mercury cadmium telluride detector (MCT), has a spectral resolution of 6nm in the range 930–2500 nm (0.49–1.13 eV). As excitation source, an 808 nm line laser was used with an irradiated power density of 2 W/cm2 (Lasiris Magnum II). A 1000 nm low-pass filter prevented laser beam reflections from entering the optic apparatus. The camera records a 2D image with one spatial, (x), and one spectral

dimension, (λ). By assembling images taken while the camera scans the sample, one gets a second spatial dimension, (y). This provides a PL spectrum in each spatial pixel(x,y) of the sample. In the setup for this study, the spatial resolution is 250 µm. Images are taken of the samples at room temperature, 300 K, and of the samples cooled with liquid nitrogen to 90 K. A similar setup has been used in previous studies [9-13]. The scanning speed for PL mapping was approximately 0.6 cms^{-1} for the spatial resolution used in this study.

A tool to separate PL of different origins, even though they have overlapping spatial distribution and/or PL spectrum, is multivariate curve resolution analysis (MCR) [15]. The mathematical method uses multivariate statistics for deconvolving complex, convoluted signals composed of several discrete, simultaneously occurring signals and can be represented mathematically by Eq. (1):

$$D = CS^T + E$$

MCR decomposes the measured data, matrix D, into a number of representative scores in matrix S^T, with the corresponding loading vectors in matrix C. An alternating least squares (ALS) algorithm is used to minimize the error matrix, E. The different radiative components are manifested with images of the spatial distribution in S^T and their corresponding spectrum in C. In this study, the MCR algorithm in PLS_Toolbox version R8.2.1 (Eigenvector Research, Inc., USA) running on MATLAB R2016b (The MathWorks, Inc., USA) was used.

3. Results and discussion

OxyMap measurements of the sample give the O_i distribution along the wafer diagonal shown in Fig. 2. The O_i

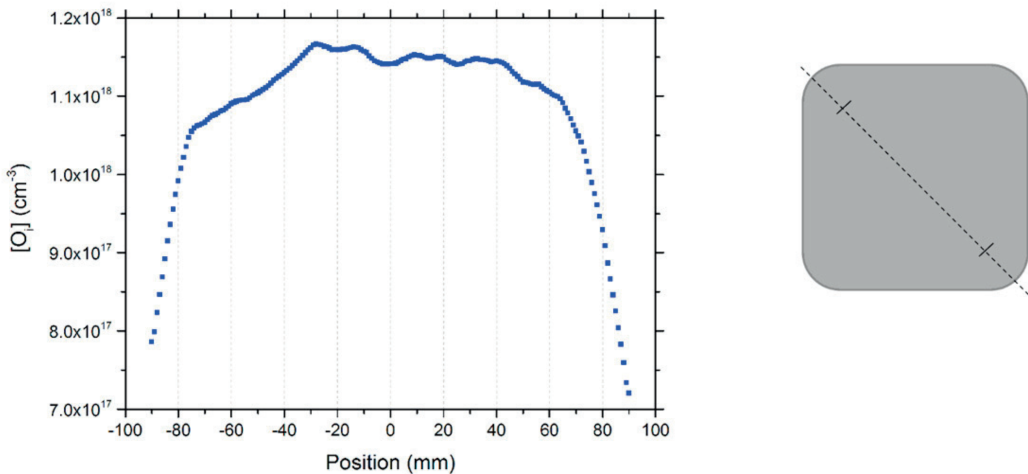

Fig. 2. Concentration of interstitial oxygen distribution along the wafer diagonal.

content was found to be around 1.1×10^{18} cm^{-3}, higher in the centre of the wafer and decreasing towards the wafer edge. The distribution of TD across the wafer diagonal is very similar (not shown here), with higher [TD] at wafer centre, since it is greatly dependent on [O_i].

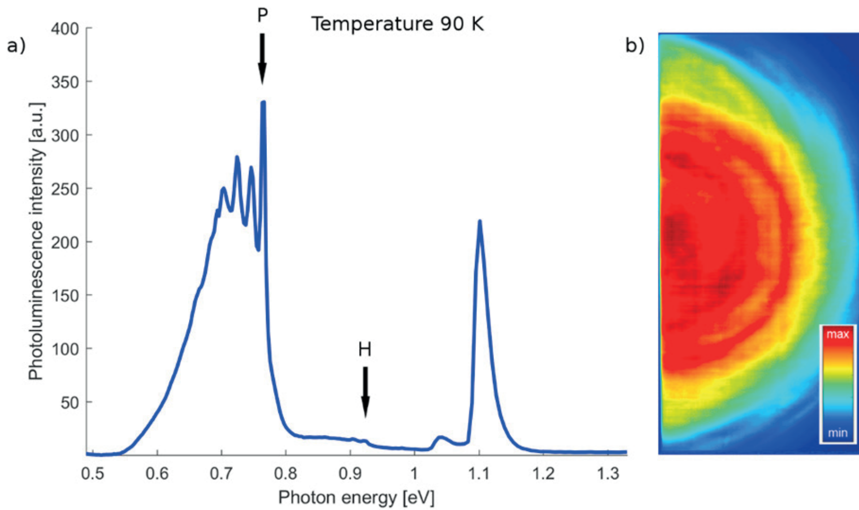

Fig. 3. (a) Photoluminescence spectrum from a textured cz-Si n-type wafer at T = 90 K. P and H lines marked. (b) Image from the integral of defect related photoluminescence, range 0.66–0.77 eV

The hyperspectral PL spectrum, integrated over the entire surface of the Cz-Si n-type wafer, cooled to 90 K, is shown in Fig. 3a). The low intensity in the band-to-band PL, at 1.10 eV, could either be due to rapid recombination of photoexcited charge carriers due to high surface recombination in the unpassivated sample or due to enhanced recombination caused by a high oxygen content. A weak signal from the H line is found at 0.926 eV. If looking at the defect related PL as a single entity, it gives rise to a broad band with peak centred at 0.72 eV. This broad band also has local sharp peaks. The one with highest energy is the P line at 0.767 eV. Other local peaks are at 0.746 eV, 0.724 eV, 0.704 eV and shoulders at 0.789 eV, 0.684 eV and 0.666 eV. The spatial distribution of the defect related PL is given in Fig. 3b). The pattern is ring-like and strongest in the centre. This correlates well with the concentration of O_i (Fig. 2) and TD.

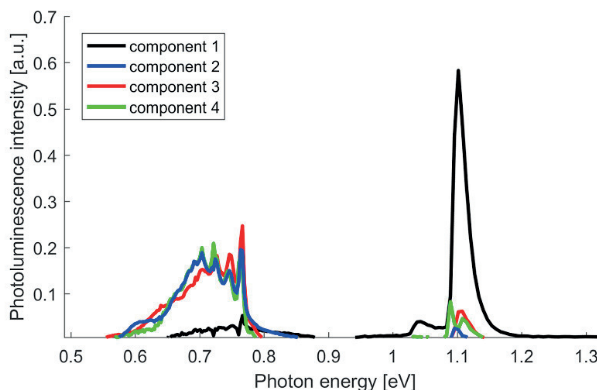

Fig. 4. MCR analysis only manage to separate the band-to-band PL from the TD related PL.

To investigate the spatial distribution of the various local peaks, MCR was used. MCR analysis did not divide the TD related PL into different signals, neither spatial nor spectral. Only the band-to-band signal was separated (Fig. 4). This indicates that all peak energy levels are present simultaneously from the defects in this wafer.

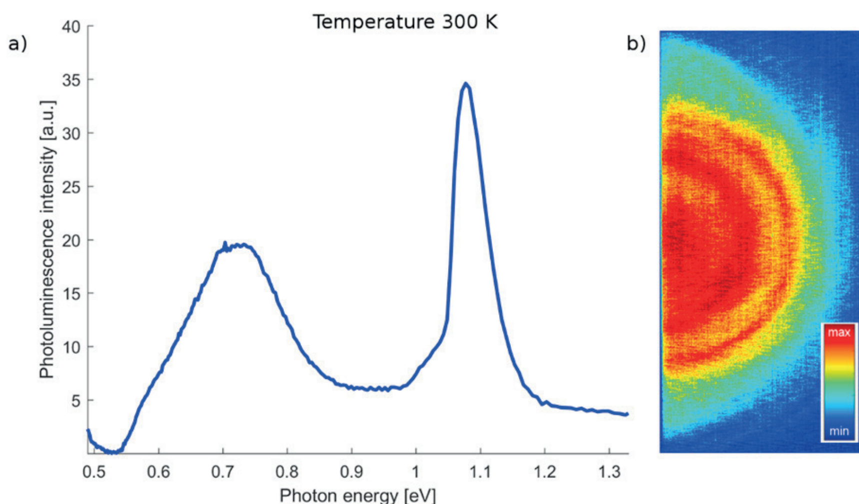

Fig. 5. Hyperspectral PL imaging at room temperature. a) Photoluminescence spectrum from a textured Cz-Si n-type wafer at T = 300K. b) Image from the integral of defect related photoluminescence, range 0.66–0.77eV.

Since the P line is related to TD, it can be assumed that the rest of the broad band with center at 0.72 eV also is related to TD. The different energy levels can be due to phonon replicas and/or TD with different oxygen–silicon complexes.

The results from the measurement at 300 K are shown in Fig. 5. The band-to-band PL has shifted from a sharp peak at 1.10 eV in the cooled (90 K) wafer to a broader peak with center at 1.08 eV for the sample at 300 K. This corresponds to the narrowing of bandgap with higher temperature [16]. There is also a broad PL signal with center peak at 0.72 eV, without any significant local peaks. Neither is the P line seen, as expected since the temperature is higher than 150 K. Nor is the H line detected.

The spatial distribution of the 0.72 eV signal is shown in Fig. 5 b). Even though the PL signal is weaker and has lower signal to noise ratio, the spatial distribution corresponds with the measurement obtained at 90 K, and therefore has the same origin. It is not possible to detect, from this dataset, if the peak center is shifted towards lower energies due to higher temperature.

4. Conclusion

As expected from the literature, the P line at 0.767 eV was observed in the areas full of TD at low temperature. This line was accompanied by the broad band with centre peak at 0.72 eV that can also be detected at room temperature. Hyperspectral PL imaging seems thus a promising tool to detect heterogeneous distribution of defects also in Czochralski Si.

Very few trap-assisted recombinations are radiative at room temperature. The most studied is the D1 (at 0.807 eV) defect line [17], and the broad defect emission band at 0.72 eV has previously been detected at room temperature [8]. The emission strength of this 0.72 eV band is comparable to the band-to-band PL signal. This indicates that these mechanisms can be used for a variety of applications, such as up conversion of photons, light emitting diodes and classifications of wafers.

The origin of the local peaks within the 0.72 eV signal at 90 K should be a topic for further studies.

References

[1] Haunschild, J., et al., Detecting efficiency-limiting defects in Czochralski-grown silicon wafers in solar cell production using photoluminescence imaging. Physica Status Solidi-Rapid Research Letters, 2011. 5(5-6): p. 199-201.
[2] Tomassini, M., et al., Recombination activity associated with thermal donor generation in monocrystalline silicon and effect on the conversion efficiency of heterojunction solar cells. Journal of Applied Physics, 2016. 119(8): p. 084508.
[3] Pizzini, S., et al., The photoluminescence emission in the 0.7-0.9 eV range from oxygen precipitates, thermal donors and dislocations in silicon. Journal of Physics-Condensed Matter, 2000. 12(49): p. 10131-10143.
[4] Minaev, N. and A. Mudryi, Thermally ‐ induced defects in silicon containing oxygen and carbon. physica status solidi (a), 1981. 68(2): p. 561-565.
[5] Uozumi, Y. and T. Katoda, Effects of stress on generation of P-line defects near insulator-silicon interface. Applied surface science, 1997. 117: p. 624-628.
[6] Tajima, M., P. Stallhofer, and D. Huber, Deep Level Luminescence Ralated to Thermal Donors in Silicon. Japanese Journal of Applied Physics, 1983. 22(9A): p. L586.
[7] Wagner, P. and J. Hage, Thermal double donors in silicon. Applied Physics A, 1989. 49(2): p. 123-138.
[8] Tajima, M., Characterization of semiconductors by photoluminescence mapping at room temperature. Journal of Crystal Growth, 1990. 103(1-4): p. 1-7.
[9] Olsen, E. and A.S. Flo, Spectral and spatially resolved imaging of photoluminescence in multicrystalline silicon wafers. Applied Physics Letters, 2011. 99(1): p. 3.
[10] Burud, I., et al., Hyperspectral photoluminescence imaging of defects in solar cells. Journal of Spectral Imaging, 2016. 5.
[11] Lausch, D., et al., Classification of crystal defects in multicrystalline silicon solar cells and wafer using spectrally and spatially resolved photoluminescence. Journal of Applied Physics, 2016. 119(5).
[12] Mehl, T., et al., Defects in multicrystalline Si wafers studied by spectral photoluminescence imaging, combined with EBSD and dislocation mapping. Proceedings of the 6th International Conference on Crystalline Silicon Photovoltaics (Siliconpv 2016), 2016. 92: p. 130-137.
[13] Flo, A., et al., Distribution of radiative crystal imperfections through a silicon ingot. Aip Advances, 2013. 3(11): p. 9.
[14] Veirman, J., et al., Oxygen-defect characterization for improving R&D relevance and Cz-Si solar cell efficiency. Photovoltaics International, 2016. 33.
[15] Tauler, R., Multivariate curve resolution applied to second order data. Chemometrics and Intelligent Laboratory Systems, 1995. 30(1): p. 133-146.
[16] A. Schenk, Finite-temperature full random-phase approximation model of band gap narrowing for silicon device simulation, Journal of Applied Physics, 84 (7), pp. 3684–3695, 1998.
[17] Koshka, Y., et al., Scanning room-temperature photoluminescence in polycrystalline silicon. Applied physics letters, 1999. 74(11): p. 1555-1557.

Paper VI

Defect related radiative recombination in mono-like crystalline silicon wafers

E. Olsen*[,1], S. Bergan[1], T. Mehl[1], I. Burud[1], K. E. Ekstrøm[2], and M. Di Sabatino[2]
1 Norwegian University of Life Sciences (NMBU), Universitetstunet 3, 1430 Ås, Norway
2 Norwegian University of Science and Technology (NTNU), Alfred Getz vei 2B, 7491 Trondheim, Norway
Received 3 March 2017, revised 10 April 2017, accepted 10 April 2017 Published online 27 April 2017
Keywords defects, photoluminescence, radiative recombination, silicon, wafers
* Corresponding author: e-mail espen.olsen@nmbu.no, Phone: +47 67 23 15 66, Fax: +47 67 23 15 01
Phys. Status Solidi A 214, No. 8, 1700124 (2017) / DOI 10.1002/pssa.201700124

Abstract

We report on studies of sub-bandgap defect related photoluminescence (DRL) signals originating from radiative recombination through traps in the bandgap of cooled mono-like silicon wafers. Spectrally resolved photoluminescence (SPL) and multivariate curve resolution (MCR) have been used in combination, to study the behaviour of sub-bandgap photoluminescence (PL) emissions in wafers cut from different heights in a pilot-scale mono-like silicon ingot. No DRL signals were found in the main mono-like body. Strong defect related sub-bandgap emissions correlating with heavily dislocated areas, are found directly above some of the seed junctions. The DRL signal exhibits a correlation with the number of axis with small angle misalignment in the junctions of the seeds. The signal conventionally labelled D1 (0.80 eV) decreases with ingot height. A mechanism relating this signal to oxygen is proposed. The signals D3 (0.94 eV) and D4 (1.00 eV) are found to co-occur, supporting previous studies, and similarly to the D2 (0.87 eV) signal, their strength is found to increase with ingot height. As the content of the transition metal impurities in the ingot is supposed to increase with height, this supports a reported link between the D3 and D4 signals with Fe, as well as a link between D2 and other impurities. An emission previously found in multicrystalline material and labelled D07 (0.70 eV), is found to solely exist as the only DRL signal recorded by us in parasitic crystals, growing into the main mono-like ingot from the crucible walls. This contradicts the common notion that the D1–D4 signals are strongly related to, and always follow dislocations.

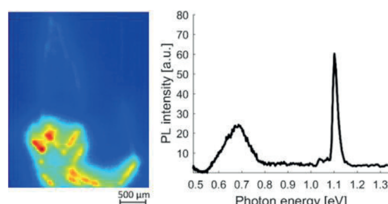

Total photoluminescence spectrum (right) and distribution (left) of the PL signal with centre energy 0.70 eV emanating from the parasitic crystals growing into the bulk mono-like Si crystal from the crucible walls.

1 Introduction

Recent progress in material development for crystalline silicon solar cells has been centred around two main routes: i) high-performance multicrystalline material (HPMC) and ii) mono-like silicon. The former contains a relatively fine grain structure and a high fraction of randomly oriented grain boundaries that make it easier for dislocations to move from the interior of the grains to the boundaries, and there either

interlock in the photovoltaic inactive areas or annihilate, effectively rendering them inactive with regards to recombination mechanisms [1–3]. In the latter case, measures are taken to solidify the ingot as a near-monocrystal by the relatively inexpensive directional solidification method in quartz crucibles, originally developed for making multicrystalline material [4, 5]. Both methods currently rely on seeds with the desired structure being positioned on the bottom of the crucible, with polycrystalline feedstock being positioned above before melting. The melting process has to be closely monitored in order to prevent complete melting of the respective seed structure. For HPMC fine grained seeds are preferred, while for mono-like material, the seeds at the bottom are of the monocrystalline type. Careful control of the crystal orientation of the seeds enables a monocrystalline solidification front to be established, and an essentially monocrystalline structure to solidify towards the top. Dislocations and impurities are considered to be the main contributors to low-lifetime areas, where photogenerated charge carriers recombine causing losses in solar cell performance. Dislocations also cause breaks in the periodic crystal lattice where impurities may accumulate due to energetically favoured mechanisms. Grain boundaries with random orientation have been found to act as sinks with possible internal gettering for impurities such as iron, while Fe is found to only segregate slightly on coincidence site lattice (CSL) boundaries [6]. In mono-like silicon, dislocations readily form due to the lack of control over thermal and mechanical stresses, and due to the near-monocrystalline structure, they are relatively free to move and multiply in the ingot [7]. It has been shown that larger inclusions of SiO_2 form inside CSL grain boundaries in slowly solidified mono-like material leading to increased generation of dislocations around these as compared to a more rapidly grown material [8]. Sub-band gap DRL is caused by radiative recombination via states or traps in the bandgap by the Shockley–Read–Hall mechanism, introduced by loss in the long range periodicity of the crystal [9]. Different impurity elements and types of dislocations are known to give rise to their own characteristic states in the bandgap [10]. By cooling the wafer, phonons are removed from the structure and, due to energy conservation, more and more of recombination mechanisms involving traps become radiative – emitting photons with characteristic energies, as the temperature is lowered. In this work, we utilise a spectrally resolved photoluminescence (SPL) method of cooled mono-like wafers, to study the distribution of these mechanisms in the bottom, middle and top of a pilot-scale mono-like silicon ingot. This method has previously been employed with success for multicrystalline material [11–14]. The purpose is to study the lateral and spectral distribution of these mechanisms in order to gain fundamental insight into the distribution of impurities – possibly in combination with dislocations.

Defect related luminescence in silicon has been studied since the 1960s [15]. In 1976, a landmark article was published, in which, 4 clearly identifiable sub-bandgap signals were found to be emitted from intentionally dislocated Czochralski (Cz) monocrystalline wafers [9]. These were labelled D1–D4 (D1: 0.80 eV, D2: 0.87 eV, D3: 0.94 eV, D4: 1.00 eV) by the authors, where D indicates that they are related to dislocations, as these signals were only found in dislocated areas. More recently, several studies have been published on the topic [16–19]. The main reasons for the increased interest has mainly been related to the connection between crystal imperfections and increased recombination of minority charge carriers – both from the electronics industry perspective and from loss in silicon solar cell performance. The D1 emission is present at room temperature and has been extensively studied as it is utilised in IR-diodes [17, 20]. The D-line emissions have been linked to a number of mechanisms. In general, the D3/D4 signals are reported to occur as a pair – one, possibly, as the phonon replica of the other. Most studies suggest D3/D4 to be associated with dislocations and/or combined with impurities decorating these [16, 21, 22]. The D1 and D2 emissions are reported by some to occur together [21], while several studies find these as separate entities [13, 23]. Screw dislocations with small twist angle have been associated with the D-lines, while

edge dislocations have been suggested to lead to non-radiative recombination [24]. Since the discovery and description of the original D1–D4 lines, several others have been identified. A strong, localised emission with similar peak energy as D3 (VID3) has been studied by Flø et al. [12]. The same paper describes two possible emissions at 0.68 and 0.74 eV. To our knowledge, no firm conclusions have yet been drawn over the nature and in particular, cause of these DRL emissions. If this could be established, it could provide a valuable tool for understanding how recombination through traps in silicon is related to structure, and how defects and impurities cause areas of low lifetime of charge carriers. For the photovoltaic (PV) industry, knowing the actual distribution of individual kinds of dislocations and impurities may enable individual treatment of wafers to diminish the detrimental effects upon final solar cell performance.

2 Experimental

A p-type (10^{16} cm^{-3}, B-doped), G1 (12 kg), mono-like, silicon ingot was produced in a Crystalox DS 250 pilot-scale furnace, by using 6 Cz monocrystalline seeds as reported by Ekstrøm et al. [7]. The seeds were oriented so that the crystallographic orientation of the seeds had the <110> direction parallel to the solidification direction. The seeds were deliberately positioned with respect to each other to form six inter-seed junctions with [110]/[110] boundary planes and three with [100]/[100] boundary planes. Two of the former junctions had intentionally made gaps of 0.4 and 1.6 mm. For the other junctions, the seeds were positioned in close contact. A schematic layout of the seed arrangement is shown in Fig. 1. The junctions have been numbered 1.1–1.6 ([110]/[110] boundary planes) and 2.1–2.3 ([100]/[100] boundary planes).

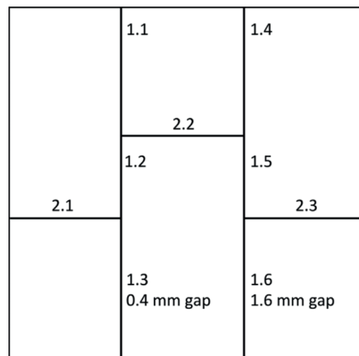

Figure 1 The layout of the initial <110> Cz monocrystalline seeds. Junctions 1.1–1.6: [110]/[110] boundary planes. Junction 2.1–2.3: [100]/[100] boundary planes. Junction 1.3 was made with 0.4mm gap. Junction 1.6 exhibited a 1.6mm gap.

A thorough study of the ingot structure and development of dislocations from bottom to top, based on microscopical methods and conventional non-spectrally resolved PL, has been published by Ekstrøm et al. [7] Wafers of 156×156mm^2 were cut from the ingot by conventional methods. In this work, we have analysed 3 of these wafers labelled (position from the bottom of the block) A-108 (42.4 mm), A-78 (54.0 mm) and A-45 (66.3 mm). The as-cut wafers were positioned on an aluminium surface cooled by liquid

nitrogen to 90 K, as previously reported for multicrystalline wafers [11–13]. The wafers were scanned using a hyperspectral camera (Specim HySpex SWIR) with a spectral range 900–2500 nm (1.34–0.49 eV) with a resolution of 6 nm. A line laser with a wavelength of 808 nm (1.53 eV) was used as excitation source. This wavelength has an average penetration depth of 12.5mm in the silicon wafer. The illumination flux was $8 \cdot 10^{18}$ photons cm^{-2}. The lateral resolution can be varied in the range 75–500 mm by focusing the lens used with the camera. The hyperspectral data are recorded as the so-called hypercube, with a 2D image for each wavelength. A schematic view of the setup is shown in Fig. 2. In order to identify possible DRL emissions, the data recorded were analysed by multivariate curve resolution (MCR). This is a statistical-mathematical method for deconvolving complex signals composed of several individual emissions. The method has been used with success together with hyperspectral imaging on silicon wafers and solar cells in a number of previous studies [11–14]. The strength of the method lies in the ability to easily extract possible components of a very complex and highly dynamic signal, over a given range of spaxels (pixels with a spectral third dimension) in the hypercube. A strong

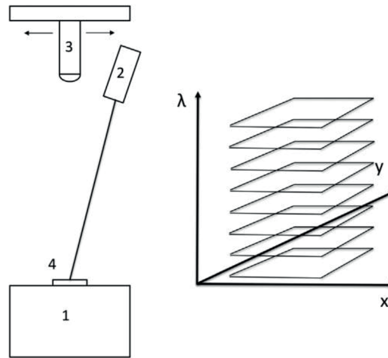

Figure 2 The hyperspectral setup (left) and a visualisation of the hypercube with one spectral- and two lateral dimensions (right). 1: Cryogenic sample holder, 2: Line laser, 3: Hyperspectral camera, 4: Sample.

MCR-signal in the score plot from an area indicates how strong the signal is relative to others in the spaxels where it is actually present. A strong signal in a few spaxels will show up as a strong signal in MCR, however, if the actual physical spectrum from a larger area is dominated by a strong emission, these individual signals will, to a large scale, be hidden in the integrated (averaged) spectrum making them difficult to identify by conventional methods. MCR detects such hidden signals and provides a way to identify smaller areas where they are strong. This applies very well to the convoluted PL spectra from solar cells or wafers, where the DRL signals may emanate from small areas containing individual defects, while being dominated by a large band-to-band (BB) signal from large areas with small amounts of defects. For a more thorough description of MCR we refer to Flø et al. [12]. As the method is based on a pure mathematical approach, it is preferable to check the validity of the results by first imaging the score plot from MCR, and then validating by checking for the identified high-intensity areas or pixels, i.e. what signals are actually present in the physical spectrum.

3 Results and discussion

3.1 Above the seed junctions

In the bottom wafer (A-108), MCR identifies three distinct components of DRL as shown in Fig. 3. Two of them correspond to D1 (0.81 eV) and D2 (0.88 eV), while the third has not been identified due to a rather low signal strength both for BB PL and DRL in this wafer. The spectra of the individual areas indicated in Fig. 3 are depicted in Figs. 4 and 5. This third signal may be a separate signal or a combination of D2 and D1. D3 (0.94 eV) and D4 (1.00 eV) are not identified by MCR as separate signals in this wafer. Physical spectra from the areas above the junctions are depicted in Fig. 6. In general, DRL from the junctions increases with ingot height, from the bottom to the top. The same signals occur in all junctions, except in 1.5 where there is no recorded DRL. Junction 2.3 clearly exhibits the strongest signal. The junctions with intentionally made gaps (1.3 and 1.6) exhibit similar DRL emission, as some junctions with no gaps, except for junction 2.3. This junction, however, exhibits a significantly larger DRL emission than the others.

In wafer A-78, cut from the middle of the ingot, the D3 (0.94 eV) and D4 (1.00 eV) signals are clearly identified by MCR integrated over the total wafer (Fig. 3), together with the three signals previously described in wafer A-108. An additional signal between D2 and D3 is also found. Judging from the physical spectra in Fig. 4, there are 4 clearly identifiable emissions (D1–D4). The emission between D2 and D3, as identified by MCR, cannot be distinguished clearly by eye from the recorded spectrum. However, as MCR constitutes a highly powerful algorithm, not being able to identify a component by eye in a complex and convolved spectrum does not constitute a verification of its absence. This will be further examined in Section 3.3 below. Junction 1.5 exhibits no DRL, while junctions 1.2 and 2.2 only exhibit a small amount. Junction 2.3, however, shows strong DRL for all the emissions D1–D4. Junctions 1.3 and 1.6 do not show a significant difference with regards to DRL or BB PL.

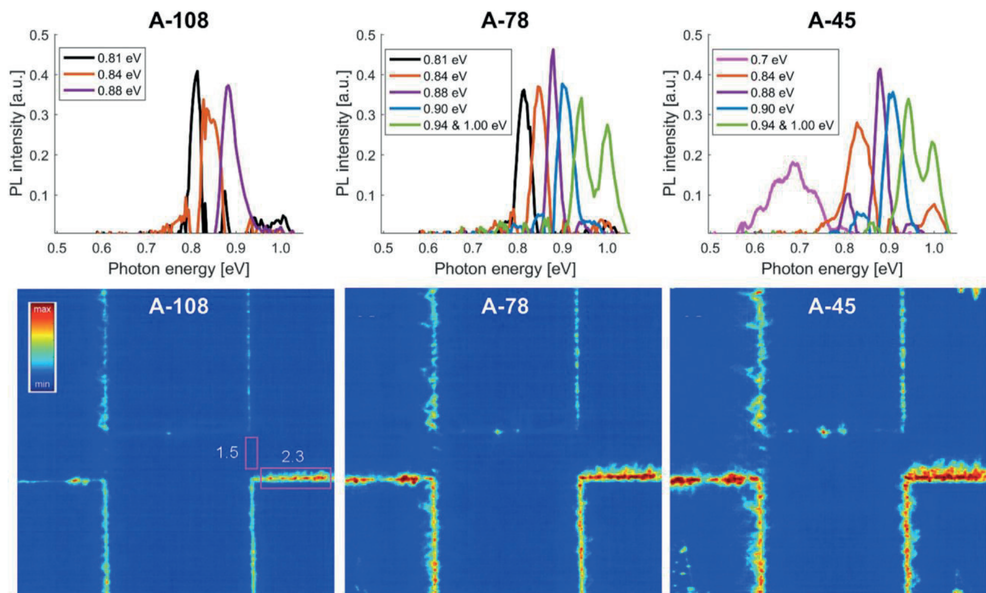

Figure 3 Image of the total DRL (BB PL, 1.1 eV omitted) signal at 90K for the respective wafers (bottom) and the corresponding results from the MCR analysis (top). The red boxes in A-108 indicate the area for the MCR analysis.

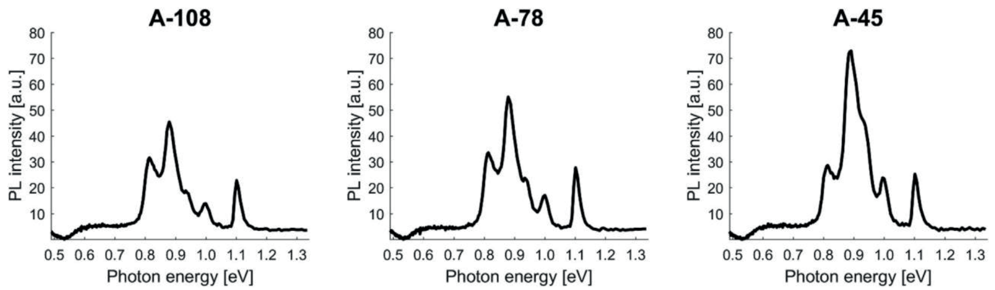

Figure 4 Total spectra (0.5–1.3 eV) from the area above junction 2.3 as indicated in Fig. 3 in the three studied wafers

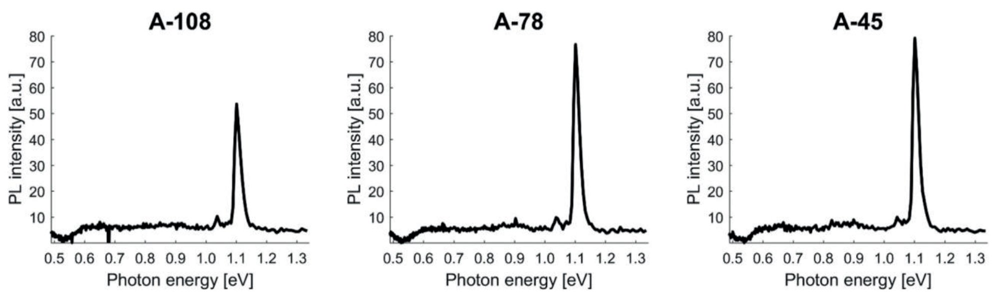

Figure 5 Total spectra (0.5–1.3 eV) from the area above junction 1.5 in the three studied wafers. No clear indications of any D-line emissions are found.

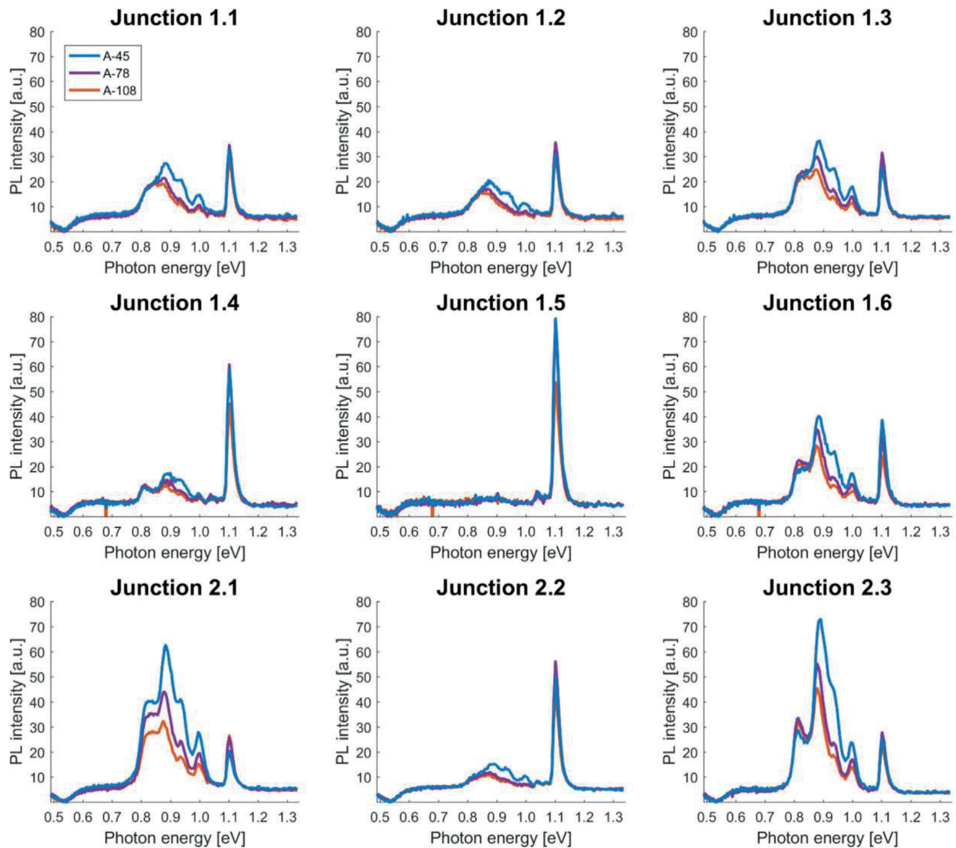

Figure 6 DRL from areas above the individual seed junctions in the wafers investigated.

In wafer A-45, the D1–D4 signals again occur in the MCR analysis for the whole wafer – except for the signal between D1 and D2. However, a notable new and broad signal is identified with peak energy around 0.7 eV [14]. A more thorough investigation reveals that the signal identified by MCR, with energy intermediate between D2 and D3, is a separate entity. An emission with this energy has previously been suggested in multicrystalline material, and will be given a further discussion below. Physical spectra from the junction areas again show D1–D4 with similar relative intensities in the individual junctions as for the other wafers. No significant DRL is recorded in junction 1.5, only small amounts in 2.2 and 1.2, while junction 2.3 exhibits a very strong signal. DRL shows similar strength in junctions 1.3 (0.4mm gap) and 1.6 (1.6mm gap).

In the work by Ekstrøm et al., the dislocation density over each junction through the ingot is identified to be a function of the number of principal axes with low-angle misorientation between the individual junctions for the seed crystals [7]. Junction 2.3 exhibits a relatively large misorientation in all three axes

(x, y, z), while junction 1.5 is almost perfectly aligned. The DRL signal, as well as the BB PL signal from the area above the seed junctions, show the same pattern as the dislocation densities. The two junctions with intentionally made gaps (1.3 and 1.6), both exhibit similar DRL activities–in the intermediate range. These observations support the conclusions made by Ekstrøm et al., that dislocation formation is more a function of misorientation than of gap width.

3.2 Parasitic crystals

The ingot exhibited a certain degree of breakdown of the mono-like structure, due to nucleation of parasitic crystals at the crucible wall during solidification. This led to a multicrystalline structure in the periphery of the ingot, close to the crucible walls, that continued to grow inwards, into the main mono-like bulk as solidification proceeded. When the centre 156×156mm^2 block was cut, most of the multicrystalline parts were cut away, however, some of it remained in the topmost wafers, particularly in the corners [7]. The MCR analysis of the integrated spectrum over the wafer A-45 identified a previously reported signal D07 in the top wafer, as seen in Fig. 3 (right) [14]. Further examination revealed this signal to be confined to the small, multicrystalline crystallites. This is evident in Fig. 7. This emission was not detected elsewhere in the ingot. Fig. 7c and d shows close-ups of two of the parasitic crystals together with the spectrum from one of the high-intensity areas (Fig. 7e).

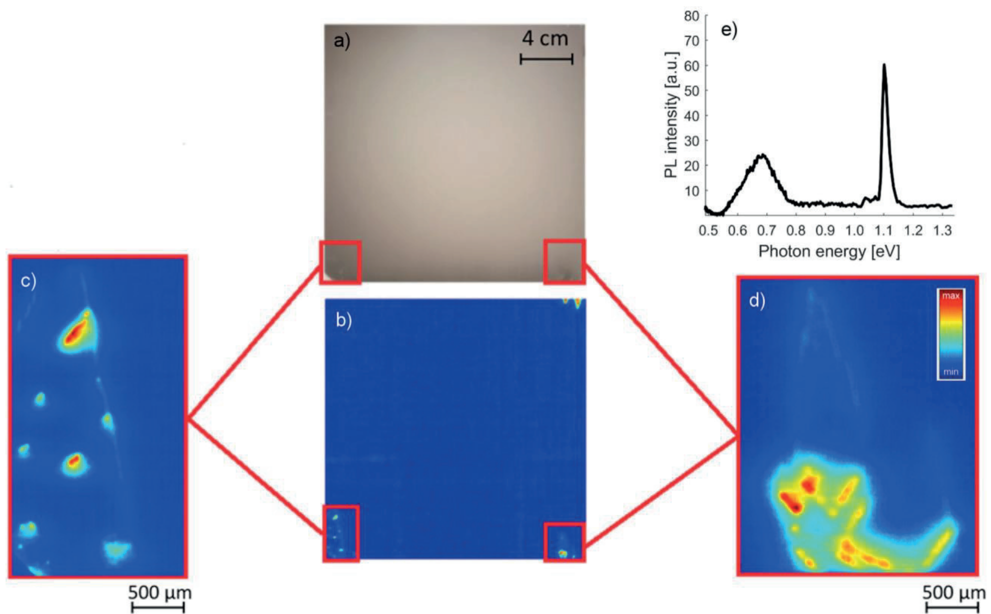

Figure 7 a) RGB image of the top wafer A-45. b) Image of the MCR score plot for the D07 (0.694 eV) emission for the whole wafer. c) and d) Close up of the MCR score plot for the D07 signal for two of the parasitic multicrystalline crystallites, pixel resolution 75mm. e) Recorded spectrum from the area indicated in d.

An emission with peak energy around 0.69 eV has previously been reported for multicrystalline wafers as emanating from distinct, small, and well localized areas [14]. It is evident from Fig. 7 that this is also the case for the parasitic crystals in this mono-like ingot. However, there is a clear signal following the

boundary between the mc-Si and the mono-like Si as seen in Fig. 7c and d. The latter is most probably a primary grain boundary with a width of several micrometres. Such boundaries may function as sinks for impurities such as Fe and O, forming clusters within the structure. This is thermodynamically favourable, as the energy associated with harbouring impurities is lower in these regions than in the Si crystal structure with high periodicity. No other DRL emissions are found in these parasitic crystals. This behaviour is unexpected, as these crystallites exhibit high etch pit densities, and thereby, a large number of dislocations as compared to the mono-like bulk ingot [7]. Dislocated multicrystalline material only exhibiting the D07 DRL has not been reported before, and contradicts the common notion that the D1–D4 signals follow dislocations and/or dislocations decorated with impurities. Most previous studies have been focused on the D1–D4 emission lines (0.80–1.00 eV) and a few studies have been reported for energies below 0.75 eV. The D1 line has been linked to oxygen precipitates [17, 25]. This may also be the case for the D07 (0.70 eV) signal. Being close to the top of the ingot it is expected that, in particular the multicrystalline parts, will contain significant amounts of impurities due to segregation effects. This calls for further studies of these structures. The D07 signal has previously been attributed to Fe_i [14]. The observations in this study, where the D07 signal is of localized character, rather suggest this signal to be linked to inclusions. However, a resolution of 0.75mm cannot distinguish if the signal is following small subgrains formed in the mc-Si crystallites, as reported by Mehl et al. [26]. These studies of FeB–Fe_i in HPM wafers with high-definition PL show a very similar distribution of Fe as found in this study. According to Graff, Fe has an acceptor trap level at $E_T = E_V + 0.4$ eV, consistent with a recombination mechanism involving free electrons from the conduction band, to recombine via this level with an emitted photon energy $E_{ph}= E_C - E_T = 1.09 – 0.4$ eV = 0.69 eV consistent with our findings [10]. This calls for further studies of these structures by methods with high magnification such as TEM.

3.3 The 0.9 eV emission

A DRL emission with peak energy of 0.90 eV has been identified in the convolved spectrum by MCR in wafers A-78 and A-45 (Fig. 3). Since the MCR score plot shows no DRL in the main bulk monolike ingot, this signal must come from the areas above the seeds or the parasitic crystals. Since the parasitic crystals only exhibit the D07 emission, the signal must be related to the dislocated areas above the seed junctions. Further examinations of the recorded spectrum in individual pixels from the hyperspectral images of the junction areas revealed that this indeed is a separate DRL emission. A plot for the total recorded emission with a centre energy of 0.90 eV over the whole A-45 wafer with individual spectra for certain identified pixels is shown in Fig. 8.

As seen from Fig. 8, the 0.9 eV signal is found in DRL active areas in all junctions, except in the DRL inactive junction 1.5. An emission with a peak around 0.9 eV has been observered by Lausch et al. for a certain crystallographic defect [14]. It has further been seen in microcrystalline thin film Si and been attributed to Si–H bonds. The observation of this distinct emission in the junction areas of as-cut mono-like wafers without any treatment means that – at least in this case, it cannot be attributed to Si–H bonds.

4 Summary and conclusions

The current work reports on examination of defect-related sub-bandgap photoluminescence from three wafers, cut from various heights in a mono-like ingot, with dislocated areas above the seed junctions. No DRL is found in the main, mono-like structure. The DRL from the junction areas are found to exhibit

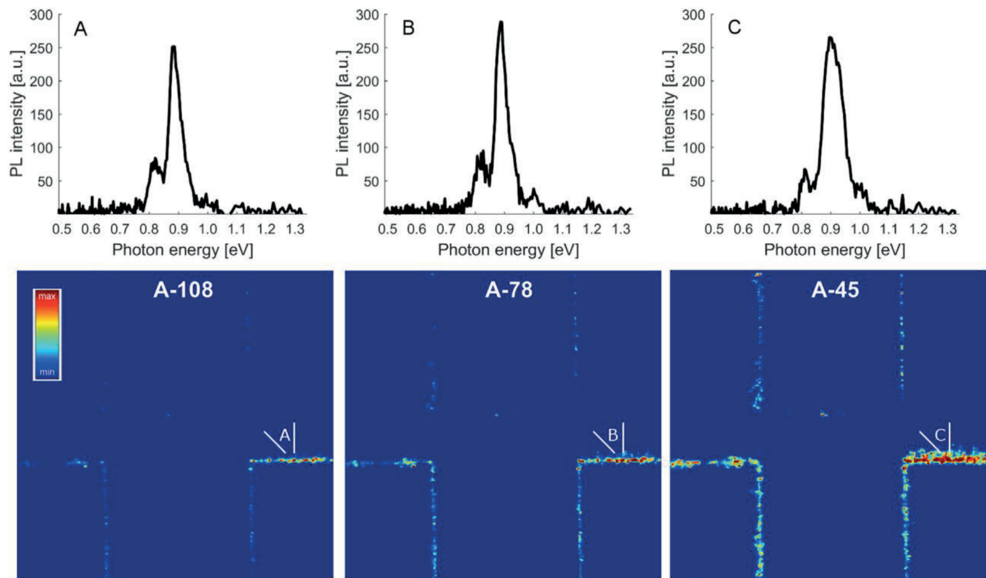

Figure 8 Recorded spectra (top) and maps (bottom) of the 0.90 eV signal in wafer A-108 (left), A-78 (middle) and A-45 (right). The spectra shows the signal in one position over junction 2.3 common to all three wafers exhibiting strong emission.

emissions consistent with previous studies of intentionally dislocated Cz wafers. The D1 emission is found to be the strongest in the bottom wafer and the weakest in the top, supporting previous suggestions that it is associated with oxygen. The D2 emission is strongest in the uppermost wafer, supporting the theories that it is associated with transition metal impurities. The D3 and D4 emissions occur as a pair and are not found in the bottom wafer, but are found in the middle- and are even stronger in the top wafer. This pair has been reported to be linked to iron or iron precipitates on dislocations. Our findings support this explanation. Further studies with complementary methods are needed to firmly establish the cause and nature of these emissions. Small areas of multicrystalline nature are found to have grown into the main, mono-like structure around the corners in the top part of the ingot. These are heavily dislocated but only exhibit one strong, broad emission with centre frequency around 0.69 eV. As dislocated areas normally exhibit all four D-band emissions – in particular high in ingots, this is a highly unexpected result which raises questions regarding the physical mechanisms and interactions between dislocations and impurities, leading to the commonly found D1–D4 emissions in silicon wafers. Studies involving splitting the FeB pair by illumination suggest the D07 emission to be caused by Fe_i [26]. We suggest this emission is caused by recombination between the conduction band edge E_C and the known trap generated by Fe at $E_T = E_V + 0.4$ eV [27]. An emission with peak energy of 0.90 eV has been found in the dislocated, DRL active junctions. A trap level consistent with this has been reported to be caused by Si–H bonds [28]. As our samples have not been subject to hydrogenation, this cannot be the case for this material. It is natural to put this into the same category as the other emissions related to impurities, as they will accumulate towards the top of the wafer due to segregation.

References

[1] C. W. Lan, W. C. Lan, T. F. Lee, A. Yu, Y. M. Yang, W. C. Hsu, B. Hsu, and A. Yang, J. Cryst. Growth 360, 68 (2012).

[2] Y. M. Yang, A. Yu, B. Hsu, W. C. Hsu, A. Yang, and C. W. Lan, Prog. Photovolt. 23, 340 (2015).

[3] S. Castellanos, K. E. Ekstrom, A. Autruffe,M.A. Jensen, A. E. Morishige, J. Hofstetter, P. Yen, B. Lai, G. Stokkan, C. del Canizo, and T. Buonassisi, IEEE J. Photovolt. 6, 632 (2016).

[4] M. Trempa, C. Reimann, J. Friedrich, D. Muller, and Oriwol, J. Cryst. Growth 351, 131 (2012).

[5] X. Gu, X. G. Yu, K. X.Guo,L.Chen, D.Wang, and D. R.Yang, Sol. Energy Mater. Sol. Cells 101, 95 (2012).

[6] M. Kn€orlein, A. Autruffe, R. Søndena, and M. Di Sabatino, Energy Procedia 55, 6 (2014).

[7] K. E. Ekstrøm, G. Stokkan, R. Sondena, H. Dalaker, T. Lehmann, L. Arnberg, and M. Di Sabatino, Phys. Status Solidi A 212, 2278 (2015).

[8] A. Autruffe, M. Kivambe, L. Arnberg, and M. Di Sabatino, Phys. Status Solidi A 213, 122 (2016).

[9] N. A. Drozdov, A. A. Patrin, and V. D. Tkachev, JETP Lett. 23, 597 (1976).

[10] K. Graff, Metal Impurities in Silicon-Device Fabrication (Springer, Berlin, 2000).

[11] E. Olsen and A. S. Flo, Appl. Phys. Lett. 99, 11903 (2011).

[12] A. Flø, I. Burud, K. Kvaal, R. Sondena, and E. Olsen, AIP Adv. 3, 112120 (2013).

[13] I. Burud, A. S. Flo, and E. Olsen, AIP Adv. 2, 042135 (2012).

[14] D. Lausch, T.Mehl, K. Petter, A. S. Flo, I.Burud, and E. Olsen, J. Appl. Phys. 119, 054501 (2016).

[15] P. J. Dean, J. R. Haynes, and W. F. Flood, Phys. Rev. 161, 711 (1967).

[16] R. Sauer, J. Weber, J. Stolz, E. R. Weber, K. H. Kusters, and H. Alexander, Appl. Phys. A: Mater. 36, 1 (1985).

[17] S. Pizzini, M. Acciarri, E. Leoni, and A. Le Donne, Phys. Status Solidi B 222, 141 (2000).

[18] I. Tarasov, S. Ostapenko, C. Haessler, and E. U. Reisner, Mater. Sci. Eng. B 71, 51 (2000).

[19] M. Tajima, Y. Iwata, F. Okayama, H. Toyota, H. Onodera, and T. Sekiguchi, J. Appl. Phys. 111, 113523 (2012).

[20] V. V. Kveder, E. A. Steinman, S. A. Shevchenko, and H. G. Grimmeiss, Phys. Rev. B 51, 10520 (1995).

[21] T. Sekiguchi and K. Sumino, J. Appl. Phys. 79, 3253 (1996).

[22] T. Arguirov, Electro-optical properties of dislocations in silicon and their possible applications for light emitters, PhD Thesis, (Brandenburger Technische Universit€at Cottbus, Cottbus, 2007).

[23] S. Ostapenko, I. Tarasov, J. P. Kalejs, C. Haessler, and E. U. Reisner, Semicond. Sci. Tech. 15, 840 (2000).

[24] T. Mchedlidze, T. Arguirov, O. Kononchuk, M. Trushin, and M. Kittler, Phys. Status Solidi C 8, 4 (2011).

[25] S. Pizzini, M. Guzzi, E. Grilli, and G. Borionetti, J. Phys. Condens. Matter. 12, 10131 (2000).

[26] T.Mehl,M. Di Sabatino,K. Adamczyk, I.Burud, and E. Olsen, Energy Procedia 92, 130 (2016).

[27] A. A. Istratov, H. Hieslmair, and E. R. Weber, Appl. Phys. A 69, 13 (1999).

[28] D. Redifield and R. Bube, Photoinduced defects in semiconductor silicon, (Cambridge University Press, Cambridge, UK, 1996).

Paper VII

Solar Energy Materials and Solar Cells 180 (2018) 130–137

Contents lists available at ScienceDirect

Solar Energy Materials and Solar Cells

journal homepage: www.elsevier.com/locate/solmat

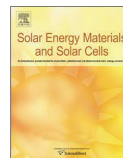

Injection intensity-dependent recombination at various grain boundary types in multicrystalline silicon solar cells

F. Frühauf[a], P.P. Altermatt[b], T. Luka[c], T. Mehl[d], H. Deniz[a], O. Breitenstein[a,*]

[a] Max Planck Institute of Microstructure Physics, Halle, Germany
[b] Global Photovoltaic Simulation Group, Case Postale 1056, 1211 Genève 1, Switzerland
[c] Fraunhofer Center for Silicon Photovoltaics (CSP), Halle, Germany
[d] Norwegian University of Life Sciences, Ås, Norway

ARTICLE INFO

Keywords:
Photoluminescence imaging
Light beam-induced current
Device simulation
Injection-dependent recombination

ABSTRACT

If the ratio of two open circuit photoluminescence (V_{oc}-PL) images taken at two different light intensities is displayed, some grain boundaries (GBs) may show up as bright lines. This indicates that these special GBs show distinct injection intensity-dependent recombination properties. It will be shown here that this results in an apparent ideality factor of the light emission smaller than unity. The effect is reproduced with numerical device simulations using a usual distribution of defects in the band gap along grain boundaries. Quantitative imaging of this apparent luminescence ideality factor by PL imaging is complicated by the lateral horizontal balancing currents flowing at open circuit. The local voltage response of an inhomogeneous solar cell at different injection levels under open circuit is modelled by Griddler simulations, based on PL investigations of this cell. The evaluation of V_{oc}-PL images at different illumination intensities allows us to conclude that the apparent luminescence ideality factor at the special GBs is about 0.89, whereas in the other regions it is between 0.94 and 0.95. Reverse bias electroluminescence showed no pre-breakdown sites, and hyperspectral PL imaging showed only in one of the investigated GBs particular defect luminescence. TEM investigations of two GBs, one showing distinct injection intensity-dependent recombination and the other one showing none, revealed that the investigated special GB is a large-angle GB whereas the GB not showing this effect is a small-angle GB.

1. Introduction

Electroluminescence (EL) and photoluminescence (PL) imaging are standard tools to study local electronic properties of solar cells. This holds in particular for cells made from multicrystalline (mc) silicon material, which still represent the major part of all solar cells produced today. Therefore a comprehensive study of the electronic properties of the extended crystal defects in mc-Si material and cells is necessary, since these defects are governing the energy conversion losses in these cells. Grain boundaries (GBs) and dislocation networks represent the significant contribution to these extended defects. It is well-known that different types of GBs in mc-Si show different recombination properties. For example, twins on (111) planes usually show little or no recombination activity, whereas low-angle GBs may show a high recombination activity [1]. These low-angle GBs are basically rows of dislocations. It was shown recently that, even within one and the same low-angle GB, regions of different recombination activity may exist, which differ in their type of dislocations representing the GB [2].

In this contribution we show by evaluating PL images of mc-Si solar cells that different GBs may show different degrees of injection intensity-dependent recombination activity. It will be shown by a simplified analytic analysis that this property can be described by an apparent ideality factor of the luminescence n_{lum} smaller than unity, which corresponds to a bulk recombination current ideality factor n_1 larger than unity. The effect is reproduced with numerical device simulations using a usual distribution of defects in the band gap along grain boundaries. In principle, n_{lum} can be imaged by evaluating V_{oc}-PL images taken at different illumination intensities. The difference between the applied bias and the local diode voltages due to horizontal balancing currents may be regarded at least approximately by applying a recently introduced correction method evaluating V_{oc}-PL images at two illumination intensities [3]. In this work this correction method is extended to the evaluation of images taken at 4 different intensities. Based on this knowledge and on 2-dimensional finite element simulations of the cell using an independently measured J_{01} distribution, n_{lum} of the special GBs are measured. By transmission electron microscopy (TEM) the crystallographic structure of one of these GBs showing and one GB not showing injection-dependent recombination was

* Corresponding author.
E-mail address: breiten@mpi-halle.mpg.de (O. Breitenstein).

https://doi.org/10.1016/j.solmat.2018.02.029
Received 6 November 2017; Received in revised form 16 February 2018; Accepted 17 February 2018
0927-0248/ © 2018 Elsevier B.V. All rights reserved.

determined. It was checked by reverse bias electroluminescence (ReBEL) [4] and hyperspectral PL imaging [5] whether these special GBs show particular defect luminescence.

2. Photoluminescence results

Two cells from different producers were investigated here, both being industrial standard technology Al-BSF (full-area back surface field) type multicrystalline (mc) cells with 3 busbars, 156 × 156 mm^2 in size. It should be noted that the special GBs reported here have been found also on several other cells of this type, hence they seem to be quite common at least in this type of solar cells. PL measurements have been performed under open circuit and short circuit conditions by using a custom built PL system employing LED illumination at 850 nm (870 nm short-pass filtered) and 950–1000 nm bandpass filtering in front of the thermoelectric-cooled ANDOR iKon-M PV-Inspector camera used with a LINOS inspec.x M NIR 1.4/50 mm objective. All open circuit (V_{oc})-PL images shown and evaluated here are net PL images, hence from all of them a short circuit (J_{sc})-PL image taken at the same illumination intensity and acquisition time was subtracted, see [6]. This procedure makes the PL images equivalent to EL images for the same local diode voltage [7] and corrects for the baseline and residuals of the excitation illumination. For (V_{oc})-PL images the luminescence correction is very minor, but the baseline and illumination light correction remains important. Usually deconvolution of the luminescence images is applied for correcting photon scatter in the detector [8,9]. We have shown recently [10] that, for our band-pass filtered luminescence images, deconvolution leads to minor improvements of the spatial resolution but may degrade the signal-to-noise ratio. Therefore we have not applied spatial deconvolution for most of our results. Only the final result of the image of the luminescence ideality factor will be presented either without or including spatial deconvolution of the luminescence images.

Fig. 1(a) shows a net V_{oc}-PL image of the first investigated cell taken at 0.5 sun equivalent intensity (measured by the nominal I_{sc}) together with an enlarged insert below. The same images measured at 0.1 sun intensity looked visually very similar. However, when the ratio of the 0.5 to the 0.1 suns images is displayed in Fig. 1(b), some bright lines appear in the enlarged insert, see white arrows. These lines are in the locations of certain isolated lying recombination-active grain boundaries, which look in a) very similar to other grain boundaries. In the ratio image (Fig. 1(b)) other separately lying grain boundaries become invisible, see e.g. dashed white arrows. These GBs obviously show an injection-independent recombination. Some cracks in the lower left of the enlarged region (black arrows) and all regions of a high local density of GBs, which may be considered as extended regions with increased recombination, appear dark in the ratio image b), see circle. This is an effect of the lateral series resistance as will be modelled in the next Section. Note that under V_{oc} condition, in defect regions of high bulk recombination current density J_{01}, the dark current dominates, whereas in "good" regions the photocurrent dominates. This leads to lateral balancing currents and thus to lateral diode voltage differences. In defect regions the local diode voltage is always smaller than in good cell regions, and these differences increase with increasing illumination intensity (linear response principle, see [11]). Therefore in these defect regions the local voltage is reduced more strongly at 0.5 suns than at 0.1 suns, leading to the dark contrast in these regions in the ratio image Fig. 1(b).

3. The apparent ideality factor of light emission

3.1. General considerations

It is well-known that Shockley-Read-Hall (SRH) recombination levels having unequal capture cross sections leads to a lifetime τ, which depends on the excess carrier concentration n. This dependency can be approximated in a restricted injection range by (see e.g. [12]):

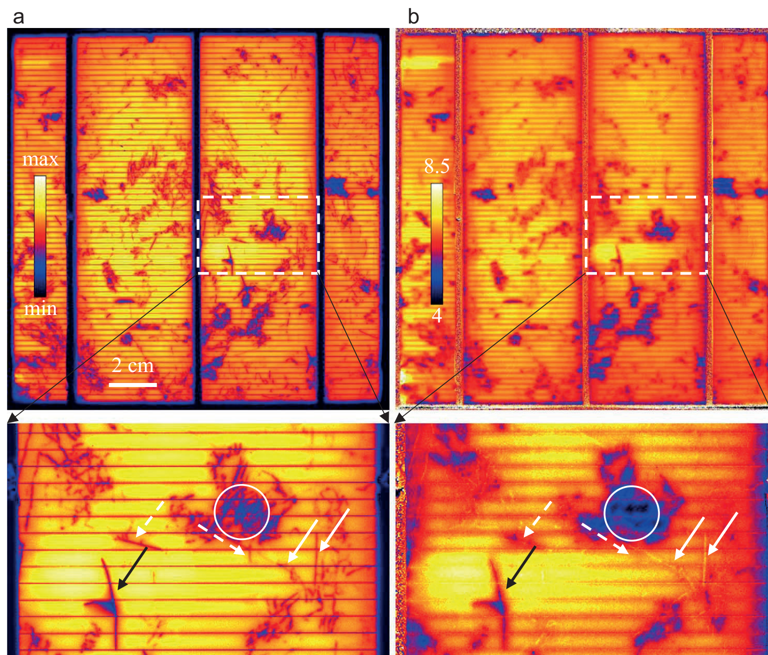

Fig. 1. a) V_{oc}-PL image of the first investigated cell at 0.5 sun [colors in a.u.], b) ratio of V_{oc}-PL images at 0.5 and at 0.1 suns intensity.

$$\tau(n) \sim n^{\alpha} \tag{1}$$

For carrier-independent lifetime $\alpha = 0$ holds, hence the lifetime is independent of the carrier density, and in the high-injection limit of a dominating SRH defect $\alpha = 1$ holds. In reality in most cases α is between 0 and 1. Then the carrier-dependence of τ is usually described by the overlapping action of two SRH defects [13]. For multicrystalline cells it has been found that this behavior is due to injection-dependent lowering of potential barriers around recombination-active GBs [14]. In "good" regions where the diffusion length L_d is larger than the cell thickness d ($L_d > d$), the saturation current density J_{01} is proportional to $1/\tau$. On the other hand, in "poor" regions with short diffusion length ($L_d < d$) and depth-homogeneous τ, J_{01} is proportional to $1/\sqrt{\tau}$ [15]. For injection-independent τ and L_d, we would have in the whole bulk ($V_{d,i}$ = local diode voltage, i = position index, V_T = thermal voltage) [7]:

$$n \sim \exp\left(\frac{V_{d,i}}{V_T}\right) \tag{2}$$

In recombination-active grain boundaries $d > L_d$ holds. In this case, again assuming depth-homogeneous τ, we obtain with (1) and (2) a dark current density of (C, C' = temporary local constants, $J'_{01,i}$ = voltage-independent local saturation current density):

$$J(V_{d,i}) = \frac{C}{\sqrt{\tau(n)}}\exp\left(\frac{V_{d,i}}{V_T}\right) = \frac{C'}{\sqrt{\left(\exp(\frac{V_d}{V_T})\right)^{\alpha}}}\exp\left(\frac{V_{d,i}}{V_T}\right) = C'\exp\left(\frac{(1-0.5\alpha)V_{d,i}}{V_T}\right) = J'_{01,i}\exp\left(\frac{V_{d,i}}{n_1 V_T}\right) \tag{3}$$

Hence, the ideality factor n_1 of the dark current due to grain boundary recombination in the bulk is expected to depend on α in SRH theory as:

$$n_1 = \frac{1}{1-0.5\alpha}. \tag{4}$$

The strong approximation behind Eq. (3) is that, for varying illumination intensity, the lifetime changes but is assumed to remain homogeneous within the bulk. In reality for $L_d < d$ a pronounced depth profile of n establishes, leading for an injection-dependent lifetime to a depth profile of τ, which influences $J(V_d)$. Moreover, a GB perpendicular to the pn-junction cannot be treated correctly by a 1-dimensional model. This will lead to a slightly different dependence of n_1 from α than in (4), but the general tendency that n_1 increases with increasing α remains. Such an increased ideality factor has been found for mc-Si cells e.g. by Macdonald et al. [13].

On the other hand, the net luminescence intensity can be described by (C_i = calibration constant at position i) [6,7]:

$$\Phi_i = C_i\exp\left(\frac{V_{d,i}}{V_T}\right) \tag{5}$$

According to Fuyuki [16] C_i is proportional to L_d, which, for $L_d < d$ (where this proportionality is only valid, see [10]), is proportional to $\sqrt{\tau}$. This leads with (1) and (2) to (C_i' = voltage-independent calibration constant):

$$\Phi_i = C\sqrt{\tau(n)}\exp\left(\frac{V_{d,i}}{V_T}\right) = C'\sqrt{\left(\exp\left(\frac{V_{d,i}}{V_T}\right)\right)^{\alpha}}\exp\left(\frac{V_{d,i}}{V_T}\right) = C_i'\exp\left(\frac{(1+0.5\alpha)V_{d,i}}{V_T}\right) = C_i'\exp\left(\frac{V_{d,i}}{n_{lum}V_T}\right) \tag{6}$$

Hence, in recombination-active grain boundary positions, where $L_d < d$ can be expected, a recombination-dependent lifetime will lead to an apparent luminescence ideality factor of:

$$n_{lum} = \frac{1}{1+0.5\alpha} \tag{7}$$

For $\alpha > 0$ this is smaller than unity, hence in these regions we expect, due to the saturation of SRH levels, that the luminescence intensity increases with increasing V_d more strongly than proportionally to $\exp(V_d/V_T)$. This is exactly what we observe at the special grain boundaries in Fig. 1(b). Again, for an injection-dependent lifetime, L_d is not constant but depth-dependent. Moreover, grain boundaries crossing the pn-junction cannot be treated by a 1-dimensional model, since there is significant horizontal excess carrier current to the GB. This means that (7) does not hold exactly, but the general tendency that n_{lum} decreases with increasing injection-dependence of τ will remain.

Please note that this apparent luminescence ideality factor smaller than unity does not mean that the basic luminescence equation $\Phi = B_{rad}\, n\, p$ does not hold anymore (B_{rad} = coefficient of radiative recombination, p = hole concentration [7]). This equation still holds at any depth in the cell and for any V_d, but the depth profile of the excess carriers may flatten with increasing V_d, which leads for increasing V_d to an increased photon yield per injected electron.

3.2. Device simulation results

For explaining the phenomenon of bright GBs in PL images in more detail, we performed two-dimensional numerical device simulations using the software Sentaurus [17]. We simulate a 1 mm wide domain with one vertical grain boundary. The defects in the grain boundary are distributed within the band gap according to a defect-pool model, which was modified from amorphous to defected silicon in [14]. Because there are acceptor-like and donor-like defects, the occupancy of these defects depend on the injection conditions and, with this, so does the stored charge and the band bending. Because the bright GBs shown in Fig. 1(b) are only moderately recombination active, we reduce the defect density by a factor of 10 compared to [14] (see Fig. 5 for p-type therein). We simulated at various illumination intensities, beginning at 0.05 suns, and extracted the PL intensity (number of photons generated by radiative recombination) at open-circuit and at short-circuit conditions, yielding $N_{ph,oc}$ and $N_{ph,sc}$. The difference between these two ($N_{ph,net}$) is proportional to the net PL signal at V_{oc}, which was also evaluated in Sect. 2. The local diode voltages V_d are the local differences of the quasi Fermi levels E_F^n -E_F^p at the depth of the pn junction in the considered position. For evaluating the apparent luminescence ideality factor we use the formula:

$$n_{lum} = \frac{V_d^{(1)} - V_d^{(2)}}{V_T ln\left(\frac{N_{ph,net}^{(1)}}{N_{ph,net}^{(2)}}\right)}, \tag{8}$$

where the index 1 and 2 denote simulations at two different but similar illumination intensities differing from each other by a factor of 2 or less.

Fig. 2 shows the resulting ideality factor of the simulated PL intensity in dependence of V_{oc}. The V_{oc} range between 548 and 631 mV corresponds to an illumination intensity between 0.05 and 2 suns.

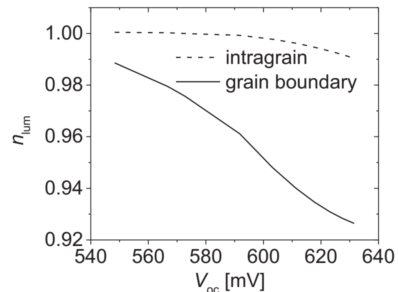

Fig. 2. Simulated apparent luminescence ideality factor as a function of V_{oc} at the grain boundary and in the intragrain region.

Results for two different parts of the simulation domain are shown: one around the GB, and the other in the remaining intragrain region between two GBs lying 1 mm apart from each other (note the mirroring boundary conditions in these simulations). The lower n_{lum} at the GB is clearly reproduced. The effect of low n_{lum} can be created irrespective of bulk lifetime, dopant density etc. and these simulation parameters are therefore not listed in detail. The slight decrease of n_{lum} also for the intragrain region at high V_{oc} is due to lateral excess carrier diffusion to the grain boundary.

4. Evaluation method of the PL results

In the following a quantitative imaging of n_{lum} will be attempted. If the local diode voltage $V_{\text{d},i}$ in any position i would be known, n_{lum} could be measured simply by measuring Φ_i at two different voltages $V_{\text{d},i}{}^{(1)}$ and $V_{\text{d},i}{}^{(2)}$ according to (8). Unfortunately, even at open circuit (V_{oc}) condition with an illumination intensity as low as 0.1 suns, in mc-Si cells the local diode voltages $V_{\text{d},i}$ may differ from V_{oc} by a voltage difference $\Delta V_{\text{d},i}$ as large as 4.7 mV [10]. For higher intensities $\Delta V_{\text{d},i}$ becomes correspondingly larger, which becomes increasingly significant. In [3] a method was proposed, based on the linear response principle [11], for calculating $\Delta V_{\text{d},i}$ by comparing V_{oc}-PL images $\Phi_i{}^{(1)}$ and $\Phi_i{}^{(2)}$ taken at different illumination intensities, leading to open circuit voltages $V_{\text{oc}}{}^{(1)}$ and $V_{\text{oc}}{}^{(2)}$. It has been found in [3] by evaluating numerical 2-dimensional Spice simulations of a model cell containing extended regions of increased J_{01} that the voltage response depends linearly on the illumination intensity only for very low intensities but tends to saturate already for intensities > 0.1 suns. This saturation was described in [3] by defining a non-linearity parameter X according to:

$$\Delta V_{d,i}^{(2)} = (1+X)\,\Delta V_{d,i}^{(1)} \tag{9}$$

For the considered case $I_{\text{sc}}{}^{(2)} = 2*I_{\text{sc}}{}^{(1)}$, $X = 1$ means linear response, which holds for the case evaluated in [3] only for very small intensities; as a rule there $X < 1$ holds. The value of X depends on several parameters, such as the illumination intensity, the value of J_{01} in the defect region, the emitter sheet resistance, and also on the defect geometry and strength. Thus, the value of X holding for a certain defect region is generally unknown. In particular, not all defect regions can be assumed to show the same value of X.

Altogether we have 4 unknown variables for each position i, which are $\Delta V_{\text{d},i}{}^{(1)}$, X_i, C_i', and $n_{\text{lum},i}$. Theoretically, by measuring net V_{oc}-PL images at four different illumination intensities (e.g. at 0.1, 0.2, 0.5, and 1 sun), we should be able to obtain all these parameters for each position. Until now the parameter X was defined only for $I_{\text{sc}}{}^{(2)} = 2*I_{\text{sc}}{}^{(1)}$. For the other intensities we may define other non-linearity parameters Y and Z for $I_{\text{sc}}{}^{(3)} = 5\,I_{\text{sc}}{}^{(1)}$ and $I_{\text{sc}}{}^{(4)} = 10\,I_{\text{sc}}{}^{(1)}$, which are:

$$\Delta V_{d,i}^{(3)} = (1+Y)\,\Delta V_{d,i}^{(1)} \quad \Delta V_{d,i}^{(4)} = (1+Z)\,\Delta V_{d,i}^{(1)} \tag{10}$$

Fortunately X, Y, and Z are not independent of each other. By evaluating all simulation points of Fig. 6 in [3] we have found that they all very accurately (maximum error 5%) follow the relation (*suns* = illumination intensity in suns):

$$\Delta V_{d,i}(suns) = \Delta V_{d,i}^{max}\left(1-\frac{a}{suns+a}\right) \tag{11}$$

The validity of (11) was proven also by the 2-dimensional finite element cell simulations for various illumination intensities shown below. If the two parameters a and $\Delta V_{\text{d},i}{}^{\max}$ in (11) are fitted to $\Delta V_i{}^{(1)}$ and $\Delta V_i{}^{(2)}$, depending on each other for a certain value of X by (9), $\Delta V_{\text{d},i}{}^{(3)}$ and $\Delta V_{\text{d},i}{}^{(4)}$ for 0.5 and 1 sun may be calculated by (11), leading to the values of Y and Z after (10). Combining (9) and (11) for 0.1 and 0.2 suns leads to the following expressions for the parameters a and $\Delta V_{\text{d},i}{}^{\max}$ as a function of X:

$$a(X) = \frac{0.2 \quad X}{1-X} \quad \Delta V_{d,i}^{max} = \Delta V_{d,i}^{(1)}\frac{1+X}{1-X} \tag{12}$$

This leads with (11) for 0.5 and 1 sun to:

$$\Delta V_{d,i}^{(3)} = \Delta V_{d,i}^{(1)}\frac{1+X}{1-0.6X} \quad \Delta V_{d,i}^{(4)} = \Delta V_{d,i}^{(1)}\frac{1+X}{1-0.8X} \tag{13}$$

This leads with (10) to:

$$Y = \frac{1.6 \quad X}{1-0.6 \quad X} \quad Z = \frac{1.8 \quad X}{1-0.8 \quad X} \tag{14}$$

Hence, if a certain value of X is assumed, this defines Y and Z by (14). For example, for $X = 1$ (linear response) $Y = 4$ and $Z = 9$ emerges, as expected by (10).

Now we may write the expected luminescence intensities for the four net V_{oc}-PL images performed at 0.1, 0.2, 0.5, and 1 sun after (5), (8), and (9):

$$\Phi_{oc}^{(1)} = C_i' \quad \exp\left(\frac{V_{oc}^{(1)} + \Delta V^{(1)}}{n_{lum}V_T}\right) \quad \Phi_{oc}^{(2)} = C_i' \quad \exp\left(\frac{V_{oc}^{(2)} + X \quad \Delta V^{(1)}}{n_{lum}V_T}\right)$$
$$\Phi_{oc}^{(3)} = C_i' \quad \exp\left(\frac{V_{oc}^{(3)} + Y \quad \Delta V^{(1)}}{n_{lum}V_T}\right) \quad \Phi_{oc}^{(4)} = C_i' \quad \exp\left(\frac{V_{oc}^{(4)} + Z \quad \Delta V^{(1)}}{n_{lum}V_T}\right) \tag{15}$$

Since Y and Z are dependent variables after (14), the independent variables in (16) are C_i', $\Delta V^{(1)}$, X, and n_{lum}. We have simulated luminescence intensities after (16) by assuming certain values for these variables and have re-extracted these variables by self-consistently solving Eq. (16) using the equation solver of Matlab [18]. This worked indeed, but only on simulated data without any noise. As soon as we added only 1% statistical noise to the simulated intensities, the evaluation lead to very noisy results. Also the application of this method to experimental luminescence data did not lead to meaningful results. Note that the assumption of the validity of (11) and the assumption made in (6) that n_{lum} is independent of the diode voltage are only approximations. Therefore we consider the self-consistent solution of (16) for evaluating experimentally obtained luminescence data as not practicable. Instead, we try to obtain these variables step-by step by using the following strategy: The first step is to calculate the expected distribution of X by performing a 2-dimensional finite element device simulation of our given solar cell. In a previous paper [19] we fitted a Griddler cell model [20] to an existing inhomogeneous solar cell by evaluating DLIT and luminescence images of this cell. The DLIT results used in [19] had a spatial resolution in the order of 1 mm. Since we are interested here in a higher spatial resolution, we use in the Griddler model applied here a high-resolution J_{01} image obtained from luminescence imaging after [10]. In contrast to [19] we assume here homogeneous values of the grid and contact resistances, which lead to very similar local diode voltage results as that found in [19]. This Griddler model was then used for predicting local diode voltage images at V_{oc} for 0.1, 0.2, 0.5, and 1 sun illumination intensity. This simulation reveals $\Delta V_{\text{d},i}$ data for these intensities. Fig. 3(a) shows these data for 0.1 sun intensity for the selected region of Fig. 1, the data for higher intensities look qualitatively similar. From the $\Delta V_{\text{d},i}$ data for 0.1 and 0.2 suns the distribution of X shown in Fig. 3(b) is obtained after (9). We see in this distribution that in most of the area X is well-defined and close to the value of 0.86, which was obtained and used homogeneously in [3]. In these regions also the simulated data for $\Delta V_{\text{d},i}$ for 0.5 and 1 sun intensity follow Eq. (11) to an accuracy better than 2%. In the strong defect regions X appears to be lower, but these regions will not be evaluated later on. In the regions where $\Delta V_{\text{d},i}$ comes close to zero (red in Fig. 3(a)), the obtained data for X in Fig. 3(b) show large positive and negative values with sharp transitions. This is an artifact coming from the fact that, in contrast to our model expectation, the regions (lines) of $\Delta V_{\text{d},i} = 0$ between regions of positive and negative $\Delta V_{\text{d},i}$ (regions of low and high J_{01}) do not remain at exactly the same positions for varying illumination intensity in reality. This is because of the non-linear dependence of $\Delta V_{\text{d},i}$ on illumination intensity. Moreover, if the cell is at its global V_{oc}, due to the lateral balancing currents not all regions within the cell are at their individual V_{oc}. Therefore in these regions of low $\Delta V_{\text{d},i}$ the prediction (9) does not hold, leading to

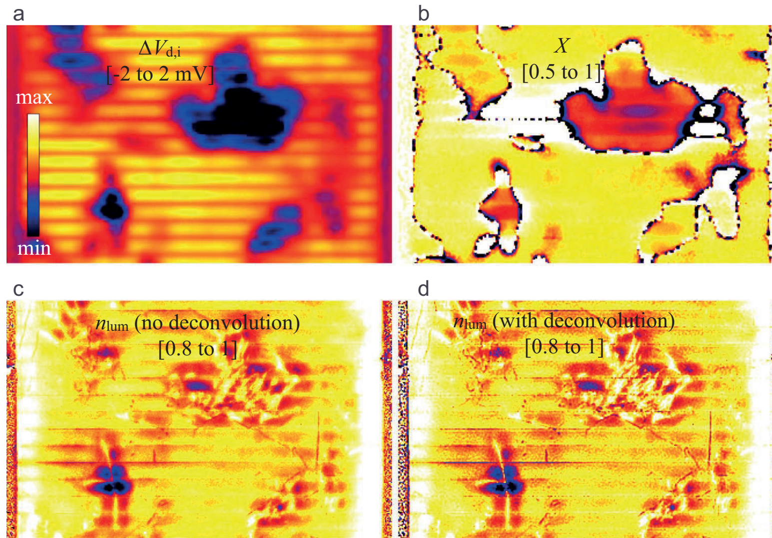

Fig. 3. a) Local voltage difference $\Delta V_{d,i}$ at 0.1 sun in the enlarged region of Fig. 1 obtained from a Griddler analysis; b) distribution of X in this region; c) distribution of n_{lum} in this region without image deconvolution; d) distribution of n_{lum} in this region after applying image deconvolution to the luminescence images.

meaningless values of X there. On the other hand, these "wrong" X data do not influence the result too much, since, if $\Delta V_{d,i}^{(1)}$ is very small, also the voltage differences for higher intensity remain small and an error in X is insignificant. Therefore, in the following evaluations we have set all values above 1 to 1 and all values below 0.5 to 0.5.

In the next step n_{lum} and C_i are determined simultaneously by a fit of the luminescence data between 0.1 and 1 sun intensity. With the known values of $\Delta V_{d,i}^{(1)}$ and X each nominator of the exponential terms in (16), which is the local diode voltage V_d, can be calculated with Y and Z obtained after (14). Applying a linear fit to the logarithmic luminescence signal Φ_{oc} of all four net V_{oc}-PL images over their corresponding local diode voltage V_d leads to a linear function with the slope $1/(n_{lum} V_T)$ and the offset $\ln(C_i')$, see also (8). Fig. 3(c) and (d) show the determined n_{lum} without and including image deconvolution after [9] applied to the luminescence images, respectively. As it was discussed already in [10], this correction only leads to a sharpening of dark lines, which, however, is necessary here for improving the accuracy of the results for a single grain boundary. We see that in most of the area outside of the defect regions n_{lum} is lying homogeneously between 0.94 and 0.95. At the special grain boundaries, which appeared bright in the ratio image in Fig. 1(b), the value of n_{lum} in Fig. 3(d), which is based on the deconvoluted luminescence images considered to be more correct, reduces down to a value of 0.89. In the defect regions n_{lum} is strongly fluctuating. We assume that this is also an artifact coming from the fact that our approximation (11) for describing the non-linearity of the voltage difference to V_{oc} does not hold anymore in regions of strongly fluctuating J_{01}. Hence, we believe that in these defect regions the PL evaluation method described in this Section is not applicable. The same holds for the regions close to the busbars, which appear to show $n_{lum} > 1$. Here we are at the border between illuminated and shadowed regions, where Eq. (11) also does not hold anymore.

5. ReBEL, SEM, TEM, and hyperspectral PL imaging results

For obtaining more information on the physical nature of the special GBs showing intensity-dependent recombination and of other GBs not showing this effect, reverse-bias electroluminescence (ReBEL [4]), scanning electron microscopy (SEM), transmission electron microscopy (TEM) and hyperspectral PL imaging [5] has been applied, the latter to another cell region in a parallel wafer showing similar grain boundaries. It was shown in [4] and also in [21] that defect-induced (type-2) breakdown occurs predominantly at strongly recombination-active GBs. This breakdown is caused by iron silicide needles [22], and the recombination activity of these GBs is most probably due to iron contamination. Fig. 4(a) shows a superposition image of the V_{oc}-PL image of the detail in Fig. 1(a) in grey with the ReBEL image of this region at − 14 V in red. This image shows that the special GB showing injection-dependent recombination (arrow *b*) shows no or only a few breakdown sites, as does a GB showing no injection-dependent recombination (arrow *a*). As found already in [21], also here most breakdown sites are found in the GB clusters.

The SEM image of GB *a* at the top of Fig. 4(b) shows that this GB is only weakly attacked by the texturing etch, whereas GB b in Fig. 3(c) is strongly attacked. The TEM image of GB *a* in the bottom of Fig. 3(b) was taken in [110] viewing direction on a Philips CM 20 T electron microscope. The GB is lying somewhat inclined to the surface normal. The selected area diffraction pattern in the inset shows that this is a small angle GB with a tilt of approximately 1.7°. GB *b* in Fig. 4(c), on the other hand, is a large angle GB. The high-resolution TEM (HRTEM) image in Fig. 4(c) was taken at a FEI TITAN 80–300 microscope. Also here the GB is inclined to the surface. Here only the upper grain could be oriented to [110] but not the lower one. Separate diffraction patterns obtained on both grains yielded a relative grain misorientation angle of about 29.7°.

Hyperspectral photoluminescence imaging provides a near infrared spectrum for each pixel in the recorded image, and has been performed to get information of the spatial distribution of different types of radiative defects [5,23,24]. Local low-temperature luminescence emission spectra of different grain boundaries have already been published by Tajima et al. [25]. Hyperspectral PL images were obtained by using a NIR hyperspectral pushbroom camera (SWIR, Specim, Finland). The HgCdTe detector has a spectral sensitivity in the 929–2531 nm (0.49–1.33 eV) range with a resolution of 6 nm (256 bands). The spatial resolution in this study was 27 and 116 µm. As excitation source, an 808 nm line laser was used with an irradiated power density of approximately 2 W/cm² (Lasiris Magnum II). To prevent laser beam

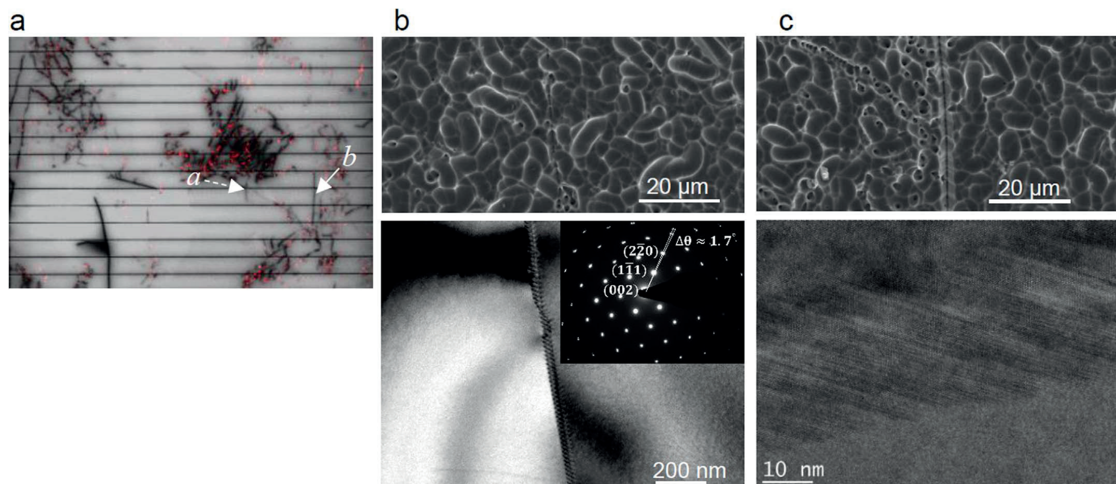

Fig. 4. a) Superposition of V_{oc}-PL (grey) and ReBEL image (red) of the detail region shown in Fig. 1; b) SEM (top) and TEM micrograph (bottom) of position *a*, inset: selected area electron diffraction pattern; c) SEM (top) and HRTEM micrograph (bottom) of position *b*. (For interpretation of the references to color in this figure legend, the reader is referred to the web version of this article.).

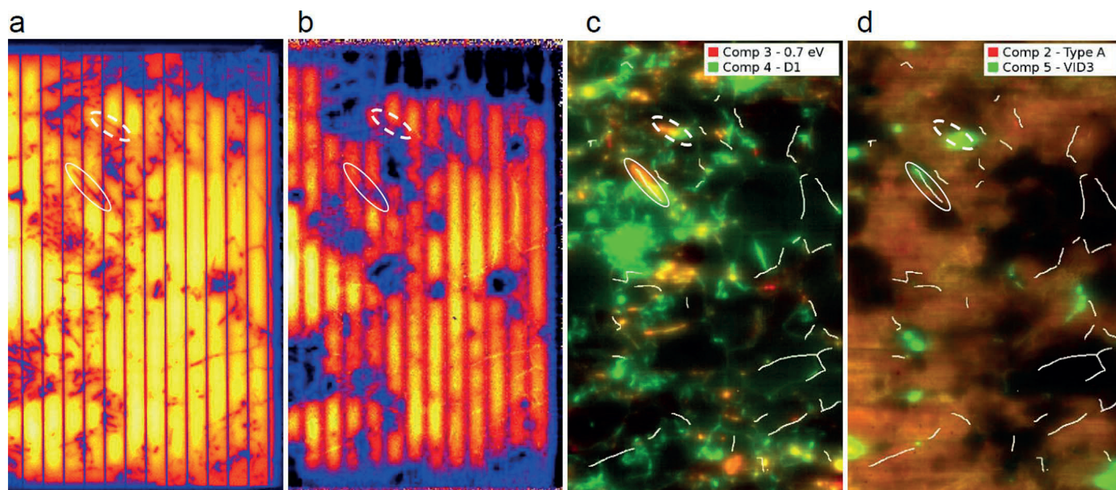

Fig. 5. a) V_{oc}-PL image (1 sun) of a region in the second investigated cell; b) ratio of V_{oc}-PL images at 1 and at 0.1 suns intensity; c) hyperspectral PL image of component 3 and 4, obtained from MCR analysis (red: component 3 with center peak energy 0.7 eV, green: component 4 at 0.82 eV (D1)); d) hyperspectral PL image (red: component 2 – two peaks, 0.94 and 1.00 eV (Type A), green: component 5 at 0.93 eV (VID3)). In areas where two components are present, the colors blend. (For interpretation of the references to color in this figure legend, the reader is referred to the web version of this article.).

reflections from entering the camera's optics, a 1000 nm low-pass filter was used. The sample was cooled to 90 K on a polished aluminum surface on top of a cryogenic cooler filled with liquid nitrogen.

To separate the different radiative defects, a multivariate curve resolution analysis (MCR) was carried out [26]. MCR is a mathematical method in multivariate statistics for deconvoluting complex, convoluted signals composed of several discrete, simultaneously occurring signals and can be represented mathematically by Eq. (16):

$$D = CS^T + E \tag{16}$$

In MCR, the measured data, matrix D, are decomposed into a number of representative scores in matrix S^T, with corresponding loading vectors in C. An error matrix, E, represents the difference between the recorded and the simulated signal. An alternating least squares (ALS) algorithm is used to minimize E. The different radiative defects are manifested as different components, with images of the spatial distribution of each defect in S^T and their corresponding spectrum in C. The MCR algorithm in PLS_Toolbox version R8.2.1 (Eigenvector Research, Inc., USA) running on MATLAB R2016b (The MathWorks, Inc., USA) was used in this study.

The hyperspectral investigations were made on a passivated wafer, which is a neighboring wafer of the second investigated cell produced by the same technology as the first one. Fig. 5(a) shows a V_{oc}-PL image of a typical region in this second cell and (b) shows the ratio image using V_{oc}-PL images at 1 and 0.1 suns, respectively. Again, in the ratio image some special grain boundaries show up as bright lines, one of

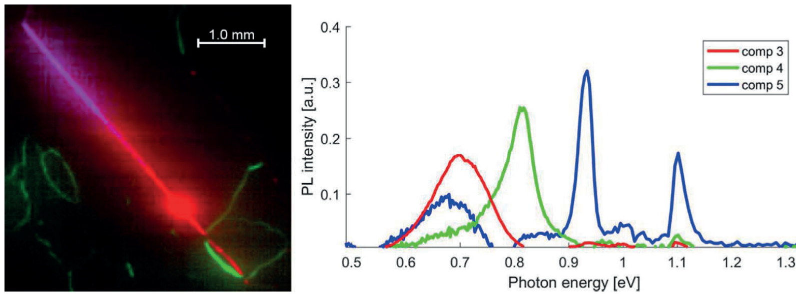

Fig. 6. Spatial distribution and respective spectra of components obtained from MCR analysis of PL from the GB marked by a solid white ellipse in Fig. 5. Each component has its own color, but in areas where two or more are present, the colors blend. (For interpretation of the references to color in this figure legend, the reader is referred to the web version of this article.).

them is indicated as a white ellipse. Another grain boundary, which does not appear bright in Fig. 5(b), is marked as a dashed ellipse. In Fig. 5(c) and (d) the positions of the special GBs showing injection-dependent recombination are marked as white lines.

The hyperspectral analysis of the neighboring wafer of this region revealed 5 spectral components between 0.49 and 1.3 eV photon energy. Fig. 5(c) and (d) show the distribution of 4 of these components in this region. Component 1 is the band-to-band PL, not shown here, but the spatial distribution is anti-correlated with component 2's, i.e., band-to-band PL in the dark areas of Fig. 5(d). Component 2 is identified as Type A defect, cf. [27], areas where the component's PL spectrum has peaks at 0.94 eV (D3) and at 1.00 eV (D4). The white lines show no correlation with neither band-to-band PL nor Type A defects, since the white lines are distributed approximately evenly between them. Component 3, 4 and 5 can be tentatively identified as interstitial iron, Fe_i, cf. [28], a Type B defect (D1), cf. [27] and VID3 of unknown origin, cf. [29], respectively. None of the special GBs, except of the one marked by the ellipse denoted with a solid white line, shows any significant defect luminescence. The marked GB shows luminescence of components 3, 4 and 5. A close-up image of the spatial distribution and respective spectra of these components, is shown in Fig. 6. The analysis shows that there are three spectral components (comp 3, 4, and 5) present in the GB. However, in spite of the relatively homogeneous appearing recombination strength of the GB visible in Fig. 5(a), the distribution of the different luminescence components is very inhomogeneous.

6. Discussion and conclusions

In this contribution evidence has been presented that, in certain special grain boundaries, the recombination is significantly injection intensity-dependent. This can easily be proven by displaying the ratio of V_{oc}-PL images taken at different illumination intensities. In these images these special GBs show up as bright lines, whereas other GBs and GB clusters do not or show up as dark areas. This injection dependence leads, if the recombination activity is high enough, to an apparent ideality factor of the luminescence smaller than unity. We attempted to measure this ideality factor by evaluating V_{oc}-PL images taken at various illumination intensities and regarding the influence of horizontal balancing currents by applying and further developing a recently proposed non-linear response description of this effect. However, this description is only approximate and does not hold in the whole cell area. Nevertheless luminescence ideality factors of 0.95 in undisturbed regions and 0.89 in the special GBs have been found. These values are in the same order as that revealed by a Sentaurus simulation of a domain in a cell containing a GB. An accurate theory relating this luminescence ideality factor of GBs to corresponding recombination ideality factors larger than 1 is still missing.

Other physical investigations of these special GBs have not revealed any particularities. TEM analysis has shown that at least one of them is a large angle GB, whereas a nearby lying GB not showing this injection dependence is a small angle GB. The special GBs do not contain particular defect-induced breakdown sites, and, with only one exception, they do not show significant defect luminescence. Hyperspectral PL investigation of the one GB showing defect luminescence has revealed an inhomogeneous distribution of three different luminescence components. This leads us to the conclusion that these GBs are relatively clean ones, hence they obviously show a moderate density of deep level defects. Such deep level defects in high numbers should lead to defect luminescence, and they would tend to pin the Fermi level for the depletion regions around the defects. If the density of such deep levels is low, however, the trapped charge and a possible potential barrier around the GBs reduce with increasing injection intensity (electron concentration) and the recombination activity gradually reduces. We believe that this is the mechanism responsible for the observed injection-dependent recombination of these special GBs. This interpretation is supported by the Sentaurus simulations, which have revealed that the apparent luminescence ideality factor smaller than unity only appears if the density of states at the GB is moderate. It would be very interesting to compare our results with nano-XRF studies as performed e.g. by Bernardini et al. [30].

These results are a contribution to a deeper understanding of the electronic behavior of GBs in mc solar silicon material. As usual, the results raise more questions than they answer. Thus, the connection between an observed luminescence ideality factor smaller than 1 to a recombination ideality factor larger than 1 for a GB going into the depth of the material still has to be established. Also the method for measuring (imaging) the luminescence ideality factor under the influence of horizontal balancing currents still has to be improved. Generally, understanding the connection between spectral defect luminescence and the electronic properties of GBs and other defects is still at its beginning.

Acknowledgements

The authors would like to thank for the financial support by the German Federal Ministry for Economic Affairs and Energy and by industry partners within the research cluster "SolarLIFE" (contract no. 0325763 D). T. Mehl's work has been a part of the FME-SuSolTech research centre financed by The Research Council of Norway. The content is in the responsibility of the authors.

References

[1] J. Chen, B. Chen, T. Sekiguchi, M. Fukuzawa, M. Yamada, Correlation between residual strain and electrically active grain boundaries in multicrystalline silicon, Appl. Phys. Lett. 93 (2008) 112105.
[2] J. Bauer, A. Hähnel, P. Werner, N. Zakharov, H. Blumtritt, A. Zuschlag, O. Breitenstein, Recombination at Lomer dislocations in multicrystalline silicon for solar cells, IEEE J. Photovolt. 6 (2016) 100–110.
[3] O. Breitenstein, J. Bauer, D. Hinken, K. Bothe, Towards an improved Laplacian-based photoluminescence image evaluation method, Sol. Energy Mater. Sol. Cells 142 (2015) 92–101.
[4] D. Lausch, K. Petter, H. v. Wenckstern, M. Grundmann, Correlation of pre-break-down sites and bulk defects in multicrystalline silicon solar cells, Phys. Status Solidi RRL 3 (2009) 70–72.

[5] I. Burud, A.S. Flø, E. Olsen, On the origin of inter band gap radiative emission in crystalline silicon, AIP Adv. 2 (2012) 042135.
[6] T. Trupke, E. Pink, R.A. Bardos, M.D. Abbott, Spatially resolved series resistance of silicon solar cells obtained from luminescence imaging, Appl. Phys. Lett. 90 (2007) 093506.
[7] K. Bothe, D. Hinken, Quantitative luminescence characterization of crystalline silicon solar cells, in: G.P. Willeke, E.R. Weber (Eds.), Advances in Photovoltaics, 2 Academic Press (Burlington), Elsevier, 2013.
[8] D. Walter, A. Fell, E. Franklin, D. MacDonald, B. Mitchell, T. Trupke, The impact of silicon CCD photon spread on quantitative analyses of luminescence images, IEEE J. Photovolt. 4 (2014) 368–373.
[9] O. Breitenstein, F. Frühauf, A. Teal, An improved method to measure the point spread function of cameras used for electro- and photoluminescence imaging of silicon solar cells, IEEE J. Photovolt. 6 (2016) 522–527.
[10] O. Breitenstein, F. Frühauf, D. Hinken, K. Bothe, Effective diffusion length and bulk saturation current density imaging in solar cells by spectrally filtered luminescence imaging, IEEE J. Photovolt. 6 (2016) 1243–1254.
[11] J.-M. Wagner, A. Schütt, J. Carstensen, R. Adelung, Linear-response description of the series resistance of large-area silicon cells: resolving the difference between dark and illuminated behavior, Energy Procedia 92 (2016) 255–264.
[12] O. Breitenstein, F. Frühauf, J. Bauer, F. Schindler, B. Michl, Local solar cell efficiency analysis performed by injection-dependent PL imaging (ELBA) and voltage-dependent lock-in thermography (Local I-V), Energy Procedia 92 (2016) 10–15.
[13] D. Macdonald, A. Cuevas, Reduced fill factors in multicrystalline silicon solar cells due to injection-level dependent bulk recombination lifetimes, Prog. Photovolt.: Res. Appl. 8 (2000) 363–375.
[14] P.P. Altermatt, G. Heiser, Predicted electronic properties of polycrystalline silicon from three-dimensional device modeling combined with defect-pool model, J. Appl. Phys. 92 (2) (2001) 2561–2574.
[15] O. Breitenstein, The physics of industrial crystalline silicon solar cells, in: G.P. Willeke, E.R. Weber (Eds.), Advances in Photovoltaics, 2 Academic Press (Burlington), Elsevier, 2013.
[16] T. Fuyuki, H. Kondo, T. Yamazaki, Y. Kaji, A. Ogane, Y. Takahashi, Analytic findings in the electroluminescence characterization of crystalline silicon solar cells, J. Appl. Phys. 101 (023711) (2007).
[17] Synopsys Inc., Mountain View, CA, USA.
[18] see 〈http://de.mathworks.com/products/matlab/index.html?requestedDomain=uk.mathworks.com〉, Jan 2017.
[19] F. Frühauf, J. Wong, J. Bauer, O. Breitenstein, Finite element simulation of inhomogeneous solar cells based on lock-in thermography and luminescence imaging, Sol. Energy Mater. Sol. Cells 162 (2017) 103–113.
[20] J. Wong, Griddler: Intelligent computer aided design of complex solar cells, in: Proceedings of the 40th IEEE PVSC, Tampa, 2013, pp. 933–938.
[21] O. Breitenstein, J. Bauer, K. Bothe, W. Kwapil, D. Lausch, U. Rau, J. Schmidt, M. Schneemann, M.C. Schubert, J.-M. Wagner, W. Warta, Understanding junction breakdown in multicrystalline solar cells, J. Appl. Phys. 109 (2011) 071101.
[22] A. Hähnel, J. Bauer, H. Blumtritt, O. Breitenstein, D. Lausch, W. Kwapil, Electron microscope verification of breakdown-inducing α-$FeSi_2$ needles in multicrystalline silicon solar cells, J. Appl. Phys. 113 (2013) 044505.
[23] E. Olsen, A.S. Flø, Spectrally and spatially resolved imaging of photoluminescence in multicrystalline silicon wafers, Appl. Phys. Lett. 99 (2011) 011903.
[24] I. Burud, T. Mehl, A. Flo, D. Lausch, E. Olsen, Hyperspectral photoluminescence imaging of defects in solar cells, J. Spectr. Imaging 5 (2016) a8.
[25] M. Tajima, Y. Iwata, F. Okayama, H. Toyota, H. Onodera, T. Sekiguchi, J. Appl. Phys. 111 (2012) 113523.
[26] R. Tauler, Multivariate curve resolution applied to second order data, Chemom. Intell. Lab. Syst. 30 (1995) 133–146.
[27] D. Lausch, T. Mehl, K. Petter, A.S. Flø, I. Burud, E. Olsen, Classification of crystal defects in multicrystalline silicon solar cells and wafer using spectrally and spatially resolved photoluminescence, J. Appl. Phys. 119 (2016) 054501.
[28] T. Mehl, M. Di Sabatino, K. Adamczyk, I. Burud, E. Olsen, Defects in multicrystalline Si wafers studied by spectral photoluminescence imaging, combined with EBSD and dislocation mapping, Energy Procedia 92 (2016) 130–137.
[29] A. Flø, I. Burud, K. Kvaal, R. Søndenå, E. Olsen, Distribution of radiative crystal imperfections through a silicon ingot, AIP Adv. 3 (2013) 112120.
[30] S. Bernardini, Nano-XRF analysis of metal impurities distribution at PL active grain boundaries during mc-silicon solar cell processing, IEEE J. Photovolt. 7 (2017) 244–249.

ISBN: 978-82-575-1528-7
ISSN: 1894-6402

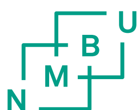

Norwegian University
of Life Sciences

Postboks 5003
NO-1432 Ås, Norway
+47 67 23 00 00
www.nmbu.no

100436 / ANDVORDGRAFISK.NO